



**TECHNISCHE
UNIVERSITÄT
WIEN**
Vienna University of Technology

Dissertation
**Numerical simulation of non-steady states of
the TRIGA Mark II reactor Vienna**

Ausgeführt zum Zwecke der Erlangung des akademischen Grades einer
Doktorin der technischen Wissenschaften

unter der Leitung von

Ao. Prof. Dr. Helmuth Böck
E142, Atominstitut
Technische Universität Wien

von

Mag. rer. nat. Julia Riede
Matrikelnummer 0147007
Butjadinger Strasse 57, D-26969 Butjadingen

Butjadingen, am 17.06.2013

Deutsche Kurzfassung der Dissertation

Seit Herbst 2006 wurden am Atominstitut Monte-Carlo Simulationen mit MCNP zur Berechnung der Neutronencharakteristik statischer Reaktorzustände durchgeführt. Der Schwerpunkt dieser Arbeiten lag auf der Entwicklung eines Modells der Reaktorgeometrie und des Inventars des TRIGA Reaktors Wien in MCNP, die Verifikation der numerischen Resultate anhand experimenteller Daten aus den ersten Kritikalitätsexperimenten, die Modellierung anhand der aktuellen Kernbeladung sowie Berechnungen zur Möglichkeit einer partiellen HEU/LEU Beladung, um Möglichkeiten des Umgangs mit Restriktionen betreffend Kernbrennstofflieferungen der aktuellen politischen Situation zu eruieren. Die aus dieser Arbeit resultierende Dissertation von R. Khan [25] beschäftigt sich ausschliesslich mit stationären Reaktorzuständen.

Die vorliegende Dissertation befaßt sich mit der Erweiterung dieses Ansatzes um die Simulation nichtstationärer Zustände des TRIGA Reaktors Wien.

Das Hauptaugenmerk liegt hierbei auf der Beschreibung und numerischen Simulation von zeitabhängigen Werten der Reaktorleistung, Neutronenflussdichte, Brennstofftemperatur und Reaktorgiften (I-135 sowie Xe-135 im speziellen) und deren experimentelle Validierung.

Ausgehend von einer detaillierten Beschreibung des TRIGA Reaktors Wien (Kapitel 3) sowie der Kinetik von Kernreaktoren (Kapitel 4) und der Darstellung des der Arbeit zugrunde liegenden numerischen Modells zur Simulation nichtstationärer Zustände (Kapitel 5) sowie der Vorstellung eines Algorithmus zur automatischen Auswertung der experimenteller Gammaspectren (Kapitel 6) wurden die genannten Simulationen durchgeführt (Kapitel 7) und mit eigenen experimentellen Daten verglichen (Kapitel 8).

Die Grundlage des Modells basiert auf einem Algorithmus von Emendörfer und Höcker in deren Lehrbuch zur Reaktorphysik [16]. Ausgehend von der kinetischen Reaktorgleichung wird dort ein rekursiver Algorithmus zur Berechnung der Abweichung der Reaktorleistung von beliebigen stationären Zuständen um Beiträge durch Änderungen der Reaktivität verursacht durch Veränderungen in der externen und internen Reaktivität (Rückkopplungsmechanismen durch Temperatur-, und Leistungsänderungen sowie Veränderungen in der Konzentration von Reaktorgiften) vorgestellt. Das Modell wurde spezifisch auf den TRIGA Reaktor in Wien angepasst und implementiert und konnte erfolgreich zur Vorhersage von Leistungsänderungen angewandt werden. Die Resultate wurden durch im Februar 2011 am Atominstitut durch die Kandidatin durchgeführte Experimente validiert.

Durch ebenfalls im Februar 2011 durchgeführte Experimente zur Messung des zeitabhängigen Inventars von Xe-135 nach Reaktorabschaltung lieferten mehr als 1200 Gammaspectren, die mit dem in Kapitel 6 präsentierten Algorithmus, (basierend auf Arbeiten von Mariscotti et al [19]) erfolgreich automatisiert ausgewertet und mit theoretischen Vorhersagen verglichen werden konnten.

Abstract

Since fall 2006 Monte Carlo calculations are being developed at the Atominstitut of the Technical University Vienna modeling the local TRIGA MARK II reactor to calculate various parameters of the reactor at continuous operation. Main focus of the calculations has been the flux density change when replacing specific fuel elements. Simulations were done both with fresh fuel elements configuration as well as burned fuel configuration. The result of this work is the PhD thesis of R. Khan [25], which focuses on calculations of steady-state operations.

This thesis expands this work onto numerical calculation of non steady-states of the TRIGA reactor Vienna. Main focus has been the explication and numerical calculation of time-dependent reactor power, neutron flux density, fuel temperature and reactor poisons (especially Xe-135) and validation of this calculations against experimental results.

Starting with an extensive description of the TRIGA reactor Vienna (chapter 3), nuclear reactor kinetics (chapter 4) and the description of the algorithm of numerical calculation of non steady-state reactor kinetics (chapter 5) a detailed description of an algorithm for automatic analysis of multiple multiline gamma ray spectra is presented (chapter 6), numerical simulations are conducted (chapter 7) and validated against experimental data (chapter 8).

The basis for the numerical model of the TRIGA reactor kinetics is the algorithm presented by Emendörfer and Höcker in their textbook on nuclear reactor physics [16]. Starting with the kinetic reactor equation they develop an recursive algorithm for calculations of deviations from steady-state reactor power which includes both external and internal reactivities. The algorithm has been adapted for the TRIGA reactor Vienna and could successfully be used for prediction of time dependent reactor power changes. The results of this calculations have been validated against experimental results gained from experiments conducted in early 2011 in Vienna.

Also in early 2011, in-core gamma ray spectrometry has been used to quantify the Xe-135 inventory after reactor shutdown. The resulting spectra have been evaluated automatically via the algorithm presented in chapter six and being compared to analytical calculations.

In memoriam Lilo Dressler (1936-2009)

Contents

1	Abstract	1
2	Introduction	3
3	The TRIGA MARK II reactor at Technical University of Vienna	5
4	A primer in reactor physics	9
4.1	Criticality	9
4.2	Reactivity and reactor period	10
4.3	Fuel temperature	11
4.4	Burnup	11
4.5	Gamma dose rates	11
4.6	Reactor kinetics	11
4.7	Delayed neutrons	12
4.8	Temperature coefficients of reactivity	13
4.9	Reactor poisoning	13
4.10	Neutron kinetics without feedback	16
4.11	Time dependent reactivity	17
4.12	Temperature feedback	17
4.13	Feedback caused by Xenon poisoning	17
5	Numerical modelling of reactor kinetics	19
5.1	The algorithm by Emmendoerfer and Hoecker	19
5.2	Application to an example problem	20

5.2.1	Including temperature feedback	20
5.3	Description of the algorithm including feedback mechanisms	21
5.3.1	Algorithm flow chart	22
5.4	Algorithm equations and step-by-step instructions	22
5.5	TRIGA specific parameters	24
6	An algorithm for the automatic analysis of batches of multi-line gamma ray spectra	27
6.1	The peak search algorithm	27
6.2	Enhancing signal quality for analysis: smoothing	32
6.2.1	Detailed description of the algorithm	36
7	Numerical simulations	37
7.1	The MCNP models	37
7.1.1	Generic model data	37
7.1.2	Core layout	40
7.2	Automatic generation of MCNP input files	43
7.2.1	Cell cards	43
7.2.2	Surface cards	45
7.2.3	Material and tally cards	45
7.3	Temperature influence on k_{eff}	45
7.4	Uncertainty analysis and runtime	46
7.5	Reactivity feedback	47
7.5.1	Reactivity	47
7.5.2	Temperature	48
7.6	Systematic parameter investigation	48
7.6.1	Variation of thermal feedback coefficients Θ_F and Θ_C	53
7.6.2	Correction factors	53
7.7	Various Perturbations	53
7.7.1	Fuel temperature: 30 ° C, positive reactivities	53
7.7.2	Fuel temperature: 30 ° C, negative reactivities	55

7.7.3	Fuel temperature: 40 ° C, positive reactivities	57
7.7.4	Fuel temperature: 40 ° C, negative reactivities	59
7.7.5	Fuel temperature: 50 ° C, positive reactivities	61
7.7.6	Fuel temperature: 50 ° C, negative reactivities	63
7.7.7	Fuel temperature: 60 ° C, positive reactivities	65
7.7.8	Fuel temperature: 60 ° C, negative reactivities	67
7.7.9	Fuel temperature: 70 ° C, positive reactivities	69
7.7.10	Fuel temperature: 70 ° C, negative reactivities	71
7.7.11	Fuel temperature: 80 ° C, positive reactivities	73
7.7.12	Fuel temperature: 80 ° C, negative reactivities	75
7.7.13	Fuel temperature: 90 ° C, positive reactivities	77
7.7.14	Fuel temperature: 90 ° C, negative reactivities	79
7.7.15	Fuel temperature: 100 ° C, positive reactivities	81
7.7.16	Fuel temperature: 100 ° C, negative reactivities	83
7.7.17	Fuel temperature: 110 ° C, positive reactivities	85
7.7.18	Fuel temperature: 110 ° C, negative reactivities	87
7.7.19	Fuel temperature: 120 ° C, positive reactivities	89
7.7.20	Fuel temperature: 120 ° C, negative reactivities	91
7.7.21	Fuel temperature: 130 ° C, positive reactivities	93
7.7.22	Fuel temperature: 130 ° C, negative reactivities	95
7.7.23	Fuel temperature: 140 ° C, positive reactivities	97
7.7.24	Fuel temperature: 140 ° C, negative reactivities	99
7.7.25	Fuel temperature: 150 ° C, positive reactivities	101
7.7.26	Fuel temperature: 150 ° C, negative reactivities	103
7.8	Fuel temperature	105
7.9	Xenon buildup	107
8	Experimental verification	109
8.1	Water temperature	109
8.2	Fuel temperature	109

8.3	Power versus shim rod position	109
8.4	Shim rod reactivity calibration	110
8.5	Reactor core temperature	113
8.5.1	Experimental setup	113
8.5.2	Experimental results	113
8.5.3	Comparison of experimental and MCNP results	115
8.6	Reactor power development with time for various reactivity inserts	118
8.6.1	Experimental setup	118
8.6.2	Results	122
8.6.3	Discussion	122
8.7	Incore gamma dose rate measurements	126
8.7.1	Experimental setup	126
8.7.2	Results	130
8.7.3	Discussion	131
8.8	Gamma spectrometry	131
8.8.1	Experimental setup	131
8.8.2	Analysis: data from Jan. 28th - Jan. 30th, 2011	134
8.8.3	Analysis: data from Feb. 1st, 2011	139
8.8.4	Discussion	144
8.9	Xenon and Iodine measurements	146
8.9.1	Analytical Iodine and Xenon history in the relevant time period	146
8.9.2	Evaluation of the experimental data for Xenon and Iodine	146
8.10	Xenon poisoning effects on reactivity	149
9	Conclusion	151
9.1	Numerical reactor kinetics	151
9.2	Xenon measurements and spectrometry in general	152
10	Acknowledgements	153
	References	163

Chapter 1

Abstract

Since fall 2006 Monte Carlo calculations are being developed at the Atominstitut of the Technical University of Vienna modelling the TRIGA MARK II reactor in Vienna to calculate various parameters of the reactor at continuous operation. Main focus of the calculations has been the flux density change when replacing specific fuel elements. Simulations were done both with fresh fuel elements configuration as well as burned fuel configuration.

Expanding those current calculations to include time dependent reactor behaviour is a logical consequence to have access to a full range of reactor behaviour simulations.

The main focus of the simulations is the numerical calculation of time dependent values for neutron flux densities, gamma dose rates, fuel temperature and reactor poisoning and the in-core measurement of gamma ray spectra for gathering detailed information about Xenon and Iodine buildup and decay during steady-state operation, startup, shutdown and for long-term poisoning effects.

All simulations are compared to actual experimental data for integral neutron flux densities at various reactor states (startup, shutdown, steady-state operations and changes due to reactivity changes), time-dependent Xenon and Iodine concentrations and reactivity feedback mechanisms (temperature and poisoning feedback effects).

To be able to analyse the massive amount of gamma ray spectra obtained experimentally an algorithm for automatic spectrum analysis including peak search, peak analysis and statistical evaluation of the experimental data has been developed. The algorithm is also applicable for general multi-line spectrum analysis. It is numerically stable, well-suited for multiplets and able to extract data relevant to analyze nuclides with short half-life times as well as nuclides with medium and relatively long half-life times.

Chapter 2

Introduction

PHYSICS IS, HOPEFULLY, SIMPLE. PHYSICISTS ARE NOT. *Edward Teller*

Since fall 2006 Monte Carlo calculations are being developed at the Atominstitute modeling the TRIGA MARK II reactor in Vienna to calculate various parameters of the reactor at continuous operation. Main focus of the calculations has been the flux density change when replacing specific fuel elements. Simulations were done both with fresh fuel elements configuration as well as burned fuel configuration [2].

Expanding those current calculations to include time dependent reactor behaviour is a logical consequence to have access to a full range of reactor behavior simulations.

The main focus of the simulations is the calculation of time dependent values for neutron flux densities, gamma dose rates, fuel temperature and reactor poisoning and the in-core measurement of gamma ray spectra to verify values for ^{135}Xe inventory calculated numerically.

Applications include the simulation of activation analysis (e.g. optimization of activation position and sample preparation) and neutron radiography with high neutron flux densities (calculation of neutron flux density at beam lines, exposure time and expected results of short-time exposure with phantoms).

There are several publications on the general topic of modelling specific aspects of TRIGA reactors with MCNP. Most of them deal with criticality and/or reactivity ([3], [4], [6], [9], [10], [11]), some with fuel related issues ([5]) or neutron flux densities ([7], [8]). As far as I can tell no simulation results of time dependent TRIGA reactor operation have yet been published. The topics of interest listed above have not yet been simulated (respectively measured in the case of in-core spectrometry) at the TRIGA Mark II in Vienna.

Chapter 3

The TRIGA MARK II reactor at Technical University of Vienna

ICH WEISS, DAS KLINGT ALLES SEHR KOMPLIZIERT ... *Fred Sinowatz, 1983*¹

The TRIGA Mark-II reactor in Vienna was built by General Atomic in the years 1959 through 1962 and went critical for the first time on March 7, 1962. Since this time the operation of the reactor has averaged at 200 days per year without any longer outages.

The TRIGA reactor is a pool-type reactor solely used for training, research and isotope production with a maximum continuous power output of 250 kW (thermal). The heat produced is released to the Danube river via two coolant circuits including a heat exchanger.

The reactor core currently consists of 83 fuel elements arranged in an annular lattice. Two fuel elements (currently positioned at C06 and E13) have got three thermocouples implemented in the fuel meat at the center and one inch above and below allowing measurements of the fuel temperature during reactor operation. At nominal power, the center fuel temperature is about 200 °C [18]. Due to the low operating power fuel burnup occurs slowly and most of the initial loaded core elements are still there.

An overview of the TRIGA Mark II reactor as cross-section drawings is shown in Figures 3.1 and 3.2.

The reactor uses a mixed core consisting of three different types of fuel elements (FE): 20% enriched Aluminium (Al) clad fuel, 20 % enriched Stainless Steel (SS) clad fuel and 70% enriched SS clad FLIP (*Fuel Lifetime Improvement Program*) fuel. The fuel consists of 8 wt % Uranium, 1 wt % Hydrogen and 91 wt % Zirconium with the Zirconium Hydride (ZrH) being the main moderator. The ratio of Hydrogen to Zirconium depends on the fuel type. [25]

As the ZrH has the special property of moderating much less effectively at higher temperatures the reactor can also be operated in pulse mode with a rapid power excursion up to 250 MW for

¹in his government policy statement 1983

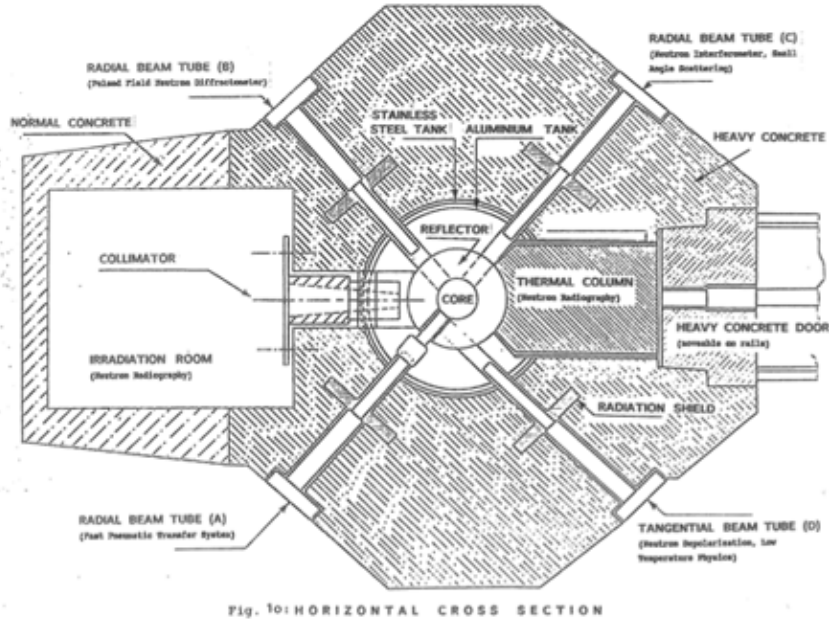


Figure 3.1: Top view of the TRIGA Mark II research reactor [18]

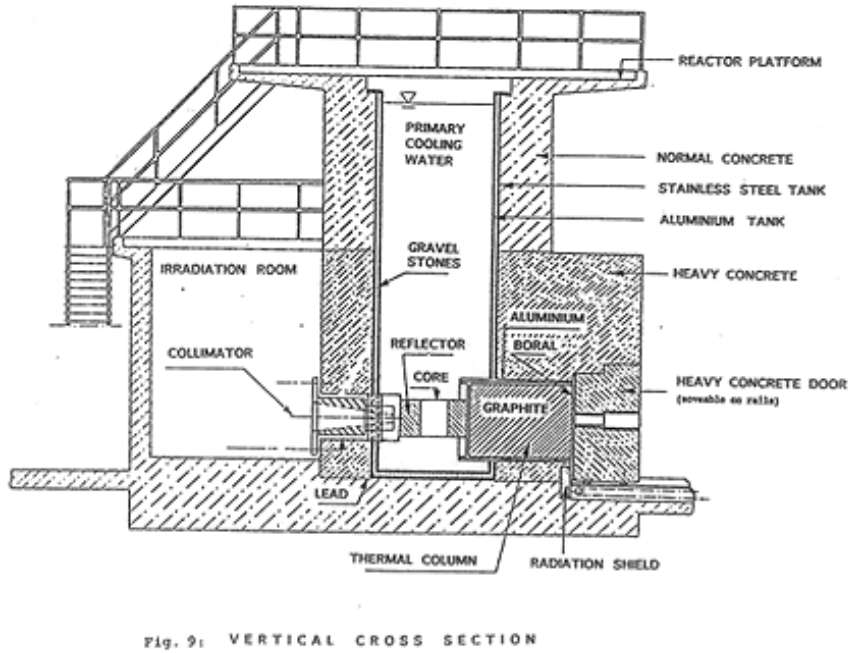


Figure 3.2: Side view of the TRIGA Mark II research reactor [18]

about 40 ms. The maximum pulse rate is 12 per hour [18] as the fuel temperature during the pulse rises to about 360 °C and causing strong thermal stress to the fuel.

The Al clad (or type 102) fuel is approximately 20% enriched with 8 wt.% ^{235}U and has got two burnable poison disks (Samarium) per FE. All type 102 FEs are indexed with the number 2 at the beginning.

The SS clad (or type 104) fuel consists of a homogenous mixture of 8.5 wt.% enriched ^{235}U and 91.5 wt.% ZrH. The enrichment of the Uranium is about 20%. This type of fuel has got a central Zirconium rod with one lower Molybdenum disks as burnable poison. All type 104 FEs are indexed with any number not being a 2 or a 7 at the beginning.

The FLIP (or type 110) fuel is a homogenous mixture of 8.5 wt.% ^{235}U , 1.6 wt. % erbium and ZrH as the remaining part.[25] The Erbium is a strong contributor to the prompt negative temperature coefficient and also acts as poison to compensate excess reactivity supplied by the high enrichment (70%) of the Uranium [25]. All FLIP Fes are indexed with the number 7 at the first position.

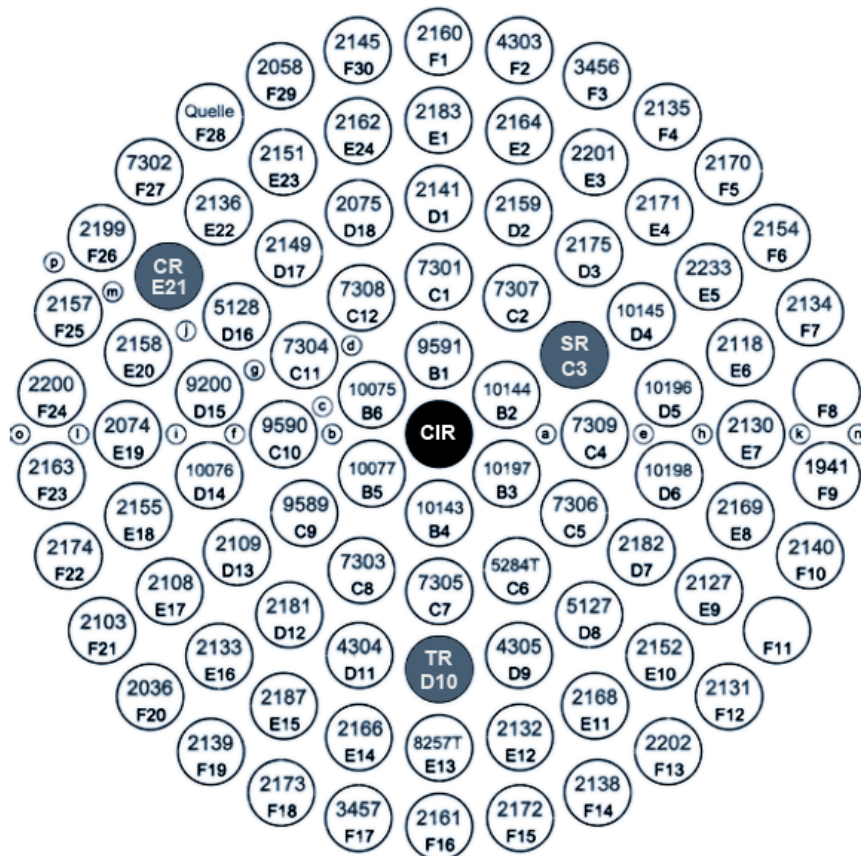


Figure 3.3: Current core configuration with shim rod (SR), transient rod (TR), control rod (CR) and the central irradiation facility (CIR).

The reactor is controlled by three control rods containing boron carbide as absorber material.

With these three rods fully inserted into the core, the neutrons continuously emitted by the start-up source (an Sb-Be photoneutron source) are absorbed almost completely forcing the reactor to a subcritical state. As soon as the control rods are withdrawn from the core (one is moved pneumatically, the other two by using an electrical motor system), the number of fissions in the core increase causing an increase of the power level.

It takes about a minute to start-up the reactor from a subcritical state to a power level of 250 kW (nominal power). It can be shutdown either manually or by using the automatic safety system. It takes about 1/10 of a second for the control rods to fall into the core.

Chapter 4

A primer in reactor physics

QUALITY ASSURANCE? WHAT FOR? WE'RE JUST BUILDING NUCLEAR POWER PLANTS. *Christoph Grawe, 2011*¹

In this chapter, the physics of nuclear reactors is reviewed and the mathematical and physical models used in the later chapters are developed.

4.1 Criticality

One of the most important factors in nuclear reactors is the *multiplication factor* k which is defined by

$$k_{\infty} = \eta \epsilon p f \quad (4.1)$$

with

- $\eta = \nu \frac{\Sigma_f}{\Sigma_a}$ average number of neutrons generated per one absorbed neutron in fuel
- ν average fission neutrons per fission
- Σ_f, Σ_a macroscopic fission and absorption cross sections of the fuel
- ϵ fast fission factor (quotient of number of fission neutrons and the number of neutrons generated by thermal fission)

The product ηf is the number of neutrons produced (on average) from the fission of fissile nuclides for each neutron absorbed in the assembly; $\eta \epsilon f$ is the total number of fission neutrons produced for each neutron absorbed in the assembly and $k_{eff} = \eta \epsilon p f$ is the total number of fission neutrons produced, on average, for each neutron introduced into the assembly by a previous fission event [12].

With P_{NL} as nonleakage probability the *effective multiplication constant* k_{eff} can be defined by

¹At Areva NP Erlangen, spring 2011, during a quick-temperated discussion on internal quality assurances processes

$$k_{eff} = \eta \epsilon p f P_{NL} = k_{\infty} P_{NL} \quad (4.2)$$

If (on average) exactly one neutron survives to cause another fission a condition referred to as *criticality* ($k = 1$) is given and the neutron population will remain constant. If less than one neutron survives the fission event the assembly is called *subcritical* ($k < 1$) and the neutron population will decrease; if more than one neutron survives the assembly the state is called *supercritical* ($k > 1$) and the neutron population will increase.

The effective multiplication constant k_{eff} depends on the composition, size and on the arrangement of the materials within the assembly.

4.2 Reactivity and reactor period

Reactivity is the measure of the departure of a reactor from critical. The effective multiplication factor, k_{eff} , determines whether the neutron density within a reactor will remain constant or change. Since the power level is directly proportional to the neutron density, whenever $k_{eff} = 1.0$, the reactor is critical and operates at a constant power level. If $k_{eff} < 1.0$, the reactor is subcritical and the power level is decreasing. If $k_{eff} > 1.0$, the reactor is supercritical and the power level is rising. (Notice that the power level, neutron density, etc., are constantly changing whenever k_{eff} is not equal to 1.0.) The difference between a given value of k_{eff} and 1.0 is known as the excess multiplication factor δk ,

$$k_{eff} - 1.0 = \delta k = k_{excess} \quad (4.3)$$

and δk may be either positive or negative, depending upon whether k_{eff} is greater or less than 1.

A useful quantity known as reactivity is given by the symbol ρ which is called *reactivity*. The reactivity ρ is directly connected to the multiplication factor k and is defined by

$$\rho = \frac{k - 1}{k} \quad (4.4)$$

Instead of the mean lifetime l usually the generation lifetime Λ ,

$$\Lambda = \frac{l}{k} \quad (4.5)$$

is used.

The reactor period ω is defined as the time needed to increase the neutron flux by a factor e and can be characterized by using the Inhour Equation (see equation 4.27).

4.3 Fuel temperature

Due to the short range of fission products and the beta particles within the core, most of the heat released during fission processes is deposited at the initial fission position. Using this assumption the power density P_V (in $[\text{Wm}^{-3}]$) can be described by [16]

$$P_V = q_f \Sigma_f \Phi \quad (4.6)$$

where q_f is the energy released in one fission event (usually around 200 MeV for Uranium), Σ_f is the total fission cross section and Φ is the neutron flux. This leads to the conclusion that the heat deposited locally can be easily calculated if one knows the neutron flux density at this specific location and the local fission cross section.

4.4 Burnup

In nuclear reactor terminology, burnup is a measure of how much energy is extracted from a primary nuclear fuel source. It is measured both as the fraction of fuel atoms that underwent fission as %FIMA (fissions per initial metal atom) and as the actual energy released per mass of initial fuel (in gigawatt-days or similar units).

Knowing the exact inventory is essential for precise reactor simulations and has to be specified for the material composition part in the relevant input files of the simulation programs.

4.5 Gamma dose rates

About 7 MeV per fission are released as prompt gamma ray photons and the fission fragments itself also can be radioactive. A rough estimate for the gamma dose rate released during the fission processes at power level of a few Watts are about 0.5 kSv/h, for 250kW this tends towards kSv/h. The dose rate generated by fission fragments depends on the burnup state of the reactor (see previous paragraph).

4.6 Reactor kinetics

The dynamics of a nuclear reactor is determined by external reactivity, reactivity feedback (internal reactivity due to temperature and poisoning effects) and the characteristics of delayed emission of neutrons from the decay of fission products.

External reactivity is induced by inserting a perturbation, for example moving of a control rod. The internal reactivity is given by reactor poisoning (e.g. Xenon poisoning) and temperature changes of coolant and fuel: increasing fuel temperature leads to increasing neutron capture caused by Doppler broadening of the resonance integral.

4.7 Delayed neutrons

Although there is quite a large number of fission products which decay via neutron emission, the observed composition emission characteristics can be well represented by defining six effective groups of delayed neutron precursor fission products[12].

Each of this groups can be defined by using a decay constant λ_i and a relative yield fraction β_i/β .

Tables for delayed neutron parameters can be found for example in [12], chapter 5. The interesting group parameters for the TRIGA reactor at ATI is the group ^{235}U with the data listed in Table 4.1.

Table 4.1: Delayed neutron parameters for the group ^{235}U [12]

Group	Fast Neutrons		Thermal Neutrons	
	Decay Constant λ_i (s^{-1})	β_i/β	Decay Constant λ_i (s^{-1})	β_i/β
1	0.0127	0.038	0.0124	0.033
2	0.0317	0.213	0.0305	0.219
3	0.115	0.188	0.111	0.196
4	0.311	0.407	0.301	0.395
5	1.4	0.128	1.14	0.115
6	3.87	0.026	3.01	0.042

The kinetic equations are

$$\frac{dn(t)}{dt} = \frac{\rho(t) - \beta}{\Lambda} n(t) + \sum_{i=1}^6 \lambda_i C_i(t) \quad (4.7)$$

and

$$\frac{dC_i}{dt} = \frac{\beta_i}{\Lambda} n(t) - \lambda_i C_i(t) \quad (i \in [1, 6]) \quad (4.8)$$

By using an one delayed neutron group approximation, we can simplify the problem further to

$$\frac{dn}{dt} = \frac{\rho - \beta}{\Lambda} n + \lambda C \quad (4.9)$$

$$\frac{dC}{dt} = \frac{\beta}{\Lambda} n - \lambda C \quad (4.10)$$

which leads to [12]

$$n(t) = n_o \left[\frac{\rho}{\rho - \beta} \exp\left(\frac{\rho - \beta}{\Lambda} t\right) - \frac{\rho}{\rho - \beta} \exp\left(-\frac{\lambda \rho}{\rho - \beta} t\right) \right] \quad (4.11)$$

$$c(t) = n_o \left[\frac{\rho \beta}{(\rho - \beta)^2} \exp\left(\frac{\rho - \beta}{\Lambda} t\right) + \frac{\rho}{\Lambda \lambda} \exp\left(-\frac{\lambda \rho}{\rho - \beta} t\right) \right] \quad (4.12)$$

Typical values for light water reactors are $\beta = 0.0075$, $\lambda = 0.08 \text{ s}^{-1}$ and $\Lambda = 6 \cdot 10^{-5}$ [12][15]. The initial value of $c(0)$ is about 1560 times higher than the initial value of $n(0)$ which leads to the conclusion that the large latent neutron source controls the dynamics of the neutron population under normal conditions. This does not hold for rapid transitions as we will see below. Equations 4.11 and 4.12 do not include any reactivity feedback mechanisms.

4.8 Temperature coefficients of reactivity

The reactivity of the system is affected severely by changes in temperature. The temperature increases associated with the increase in power reduces reactivity and prevents the power from increasing indefinitely. Normal reactor power regulation includes this effect.

The basic parameter which allows TRIGA reactors to operate safely during either steady-state or transient conditions is the prompt negative temperature coefficient given by the TRIGA fuel and core design which allows inherently safe operating in both steady-state and transient modes. A major factor in the prompt negative temperature coefficient for the TRIGA cores is the core spectrum hardening that occurs as the fuel temperature increases. A detailed explanation can be found in [18].

The temperature coefficient of reactivity is the change in reactivity per unit temperature increase. It may be positive or negative. It is usually given in $\delta k / \text{ per Kelvin}$ or in $\text{c}(\text{cent})$.

If boiling occurs in a coolant channel, steam gradually displaces coolant. The name of this effect is voiding. Partial or total void in a channel affects resonance capture, parasitic absorption, fast fission, leakage and therefore effects on reactivity, which can be positive (with respect to reactivity change) or negative. The TRIGA Mark II reactor has got a negative void coefficient, which means reactivity decreases with increasing voiding.

4.9 Reactor poisoning

The generation of fission products results in an additional absorption usually called *reactor poisoning*. The most important nuclide is ^{135}Xe with a thermal absorption cross section of 2.9E6 barns [13] and is produced either directly in thermal fission or via decay of ^{135}Te via ^{135}I (see figure 4.2). The product yields for ^{135}Te and ^{135}Xe are 6.1% and 0.2%, respectively. The number of ^{135}I nuclei $I(t)$ is given by

$$\frac{dI(t)}{dt} = (\gamma_{sb} + \gamma_{Te} + \gamma_I) \Sigma_f \Phi - \sigma_I \Phi I(t) - \lambda_I I(t) \quad (4.13)$$

The first term of equation 4.13 stands for production of Iodine as a fission product, the second term accounts for neutron capture, the third models radioactive decay. The relevant fission yields, half life times and absorption cross sections can be found in table 4.2.

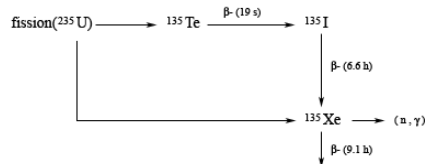


Figure 4.1: Fission product decay chain of ^{235}U to ^{135}Xe

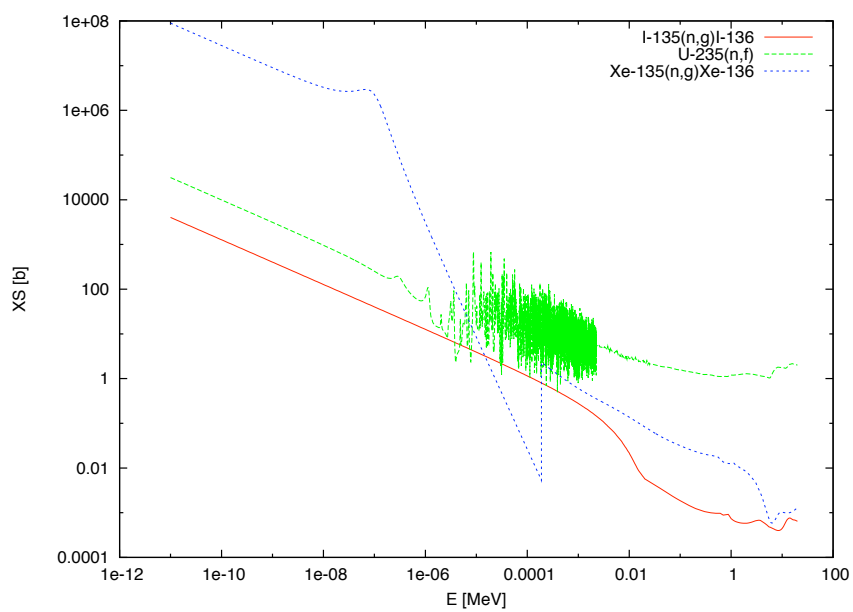


Figure 4.2: Cross sections for fission of ^{235}U and neutron capture for ^{135}Xe and ^{135}I

Equilibrium in Iodine concentration is reached at a certain time t_{eq} when the condition

$$\lambda_I I(t) = (\gamma_{Sb} + \gamma_{Te} + \gamma_I) \Sigma_f \Phi \quad (4.14)$$

is fulfilled. The steady-state concentration I_{ss} is given by

$$I_{eq} = \frac{(\gamma_{Sb} + \gamma_{Te} + \gamma_I) \Sigma_f \Phi}{\lambda_I} \quad (4.15)$$

Solving equation 4.13 leads to

$$I(t) = I_{ss} \left(1 - e^{-\lambda_I t}\right) \quad (4.16)$$

Direct algebraic calculation of the parameter t_{eq} is difficult as this involves solving an equation including the logarithm of zero. Iterative calculation of t_{eq} leads to the formula

$$t_{eq} \approx \frac{\log\left(1 - \frac{I(t)}{I(t_{eq})}\right)}{\lambda_I} \quad (4.17)$$

which converges to t_{eq} as $I(t) \rightarrow I(t_{eq})$. After 60 hours the difference between $I(t)$ and $I(t_{eq})$ is less than 0.1% which can be assumed to be a steady state. Literature speaks of 50-60 hours to reach a steady state [16].

Beta decay of ^{135}I is the main source for the buildup of ^{135}Xe . The number of ^{135}Xe nuclei $Xe(t)$ is given by

$$\frac{dXe(t)}{dt} = \gamma_{Xe} \Sigma_f \Phi - \sigma_{a,Xe} \Phi Xe(t) + \lambda_I I(t) - \lambda_{Xe} Xe(t) \quad (4.18)$$

The first term is due to initial production by fission, the second for parasitic absorption via neutron capture, the third production due to decay of Iodine and the third models loss via decay. An equilibrium between production and decay is reached after a certain time resulting in a equilibrium Xenon concentration Xe_{eq} ,

$$Xe_{eq} = \frac{\gamma \Sigma_f \Phi}{\lambda_{Xe} + \sigma_{a,Xe} \Phi} \quad (4.19)$$

The system of ordinary differential equations given by 4.18 and 4.13 can be solved by variation of constants resulting in a solution for $Xe(t)$ [16]:

$$\begin{aligned} Xe(t) = & Xe(t_{eq}) \left(1 + \frac{\gamma_I \lambda_I - \gamma_{Xe} (\lambda_{Xe} + \sigma_{a,Xe} \Phi_0)}{\gamma (\lambda_I - \lambda_{Xe} - \sigma_{a,Xe} \Phi_0)} e^{-\lambda_I t}\right) \\ - & Xe(t_{eq}) \frac{\gamma \lambda_I - \gamma_{Xe} (\lambda_{Xe} + \sigma_{a,Xe} \Phi_0)}{\gamma (\lambda_I - \lambda_{Xe} - \sigma_{a,Xe} \Phi_0)} e^{-(\lambda_{Xe} + \sigma_{a,Xe} \Phi_0)t} + Xe(0) e^{-(\lambda_X + \sigma_X \Phi)} \end{aligned} \quad (4.20)$$

For simulations during this thesis, a numerical solution of equation 4.18 has been used rather than the analytical solution from [16] shown in 4.20 as the numerical treatment was more effective regarding computing time and did not show significant deviations from the analytical results in a comparison for the used time step (1s).

Table 4.2: Relevant parameters for Iodine and Xenon production and decay [16]

Nuclide	γ (fission yield)	Half Life Time [h]	σ (absorption cross section) [cm ²]
¹³⁵ ₅₁ Sb	0.0015	4.7E-4	
¹³⁵ ₅₂ Te	0.0313	5.0E-3	
¹³⁵ ₅₃ I	0.0303	6.6	9.0E-23
¹³⁵ ₅₄ Xe	0.0024	9.1	2.9E-18

4.10 Neutron kinetics without feedback

The basis for all calculations is the kinetic equation

$$\frac{d}{dt}n(t) = \frac{\rho - \beta_{eff}}{\Lambda}n(t) + \sum_{i=1}^6 \frac{\beta_{i,eff}}{\Lambda}n(0)e^{-\lambda_i t} + \int_{t'=0}^t \frac{\beta_{eff}}{\Lambda}n(t')f(t-t')dt' \quad (4.21)$$

If $\beta_{eff,i}/\lambda$ is not time-dependent and one is interested in deviation from a stationary value

$$x(t) = \frac{n(t) - n(0)}{n(0)}, \quad n(t) = n(0) [1 + x(t)] \quad (4.22)$$

only, it holds that

$$\frac{\Lambda}{\beta_{eff}} \frac{d}{dt}x(t) = \frac{\rho(t)}{\beta_{eff}} [1 + x(t)] - x(t) + \int_{t'=0}^t x(t')f(t-t')dt' \quad (4.23)$$

together with

$$\int_{t'=0}^t f(t-t')dt' = \sum_{i=1}^6 \frac{\beta_{i,eff}}{\beta_{eff}} (1 - e^{-\lambda_i t}) \quad (4.24)$$

For a prompt jump in reactivity at $t = 0$ the equations (4.7) and (4.8) form a system of seven ordinary differential equations which can be solved analytically by a Laplace transform [16] resulting in

$$n(t) = \sum_{i=1}^6 A_i e^{\omega_i t} \quad (4.25)$$

$$c_i(t) = \sum_{j=1}^6 B_{ji} e^{\omega_j t} \quad (4.26)$$

The ω_j are the poles of the Laplace transformed equations (4.7) and (4.8) and

$$\omega_j \left(\Lambda + \sum_{j=1}^6 \frac{\beta_{eff,i}}{\omega_j + \lambda_i} \right) = \rho \quad (4.27)$$

The amplitudes A_j and B_{ij} are given by

$$A_j = n(0) \frac{\Lambda + \sum_{i=1}^6 \frac{\beta_{eff,i}}{\omega_j + \lambda_i}}{\Lambda + \sum_{i=1}^6 \frac{\lambda_i \beta_{eff,i}}{(\omega_j + \lambda_i)^2}} \quad (4.28)$$

$$B_{ij} = \frac{\beta_{eff,i}}{\Lambda(\omega_j + \lambda_i)} A_j \quad (4.29)$$

Equation (4.27) is commonly known as *Inhour equation*.

4.11 Time dependent reactivity

For continuous changes in reactivity there is no analytical solution of equation (4.21). A numerical solution can be obtained by using equation 4.21 and introducing an external neutron source q , so equation 4.23 becomes

$$\Lambda \frac{d}{dt} x(t) = \rho(t) [1 + x(t)] - \beta_{eff} x(t) + \beta_{eff} \int_{t'=0}^t x(t') f(t-t') dt' \quad (4.30)$$

4.12 Temperature feedback

For including internal feedback caused by temperature dependent effects the reactivity $\rho(t)$ has to be replaced by the sum of the external reactivity $\rho_e(t)$ and the internal reactivity $\rho_i(t)$ including this temperature feedback which is given by

$$\rho_{i,T}(t) = \alpha_{TF} [T_F(t) - T_F(0)] + \alpha_{TC} [T_C(t) - T_C(0)] \quad (4.31)$$

4.13 Feedback caused by Xenon poisoning

For or after longer reactor operation periods, the internal reactivity has to be corrected with the effects caused by Xenon poisoning. This leads to

$$\rho_i = \rho_{i,T} + \rho_{i,Xe}(t) \quad (4.32)$$

with

$$\rho_{i,Xe} = \sigma_{a,Xe} X e(t) \Phi(t) \quad (4.33)$$

Chapter 5

Numerical modelling of reactor kinetics

PREMATURE OPTIMIZATION IS THE ROOT OF ALL EVIL. *Donald E. Knuth, 1974*¹

5.1 The algorithm by Emmendoerfer and Hoecker

According to [16], a numerical solution of equation 4.30 can be obtained by we substituting

$$\frac{dx}{dt} \Big|_{t=t_n} = \frac{x(t_n) - x(t_{n-1})}{\Delta t} \quad (5.1)$$

dividing the integral into a sum of n integrals over equidistant time intervals Δt and assume piecewise linearity of $x(t')$ which results in a recursive formula for $x(t_n)$ [16]

$$x(t_n) = \frac{\rho(t_n) + \frac{\Lambda}{\Delta t} x(t_{n-1}) + \sum_{i=1}^6 F_{i,n-1} - \rho(0)}{F - \rho(t_n)} \quad (5.2)$$

with

$$F = \frac{\Lambda}{\Delta t} + \sum_{i=1}^6 \frac{\beta_{i,eff}}{\lambda_i \Delta t} (1 - e^{-\lambda_i \Delta t}) \quad (5.3)$$

and (for $n > 1$)

$$F_{i,n-1} = \frac{\beta_{i,eff}}{\lambda_i \Delta t} (1 + e^{-2\lambda_i \Delta t} - 2e^{-\lambda_i \Delta t}) x(t_{n-1}) + e^{-\lambda_i \Delta t} F_{i,n-2} \quad (5.4)$$

and

$$F_{i,0} = \frac{\beta_{i,eff}}{\lambda_i \Delta t} [1 - e^{-\lambda_i \Delta t} (1 + \lambda_i \Delta t)] \quad (5.5)$$

The method described in the equations above is applicable for continuous reactivity changes. For prompt-jump approximations at $t = 0$ the very first iteration has to be calculated by [16]

$$x(t_0) = \frac{\rho}{\Lambda} \Delta t_0 \quad (5.6)$$

¹in *Structured Programming with Goto Statements*, Computing Surveys 6:4 (December 1974), pp. 261-301

and be sure to hold $\Delta t_0 \ll \Lambda/\beta_{eff}$.

Equations 5.2 to 5.5 are the basis for all time dependent numerical calculations excluding feedback.

5.2 Application to an example problem

For testing purposes, the analytical solution of the special problem case with one group of delayed neutrons and a prompt-jump approximation has been compared to the numerical solutions by implementing the equations above in the Perl programming language. The analytical solution can be found in [16] (chapter I.2). The results of this comparison are shown in fig. 5.1.

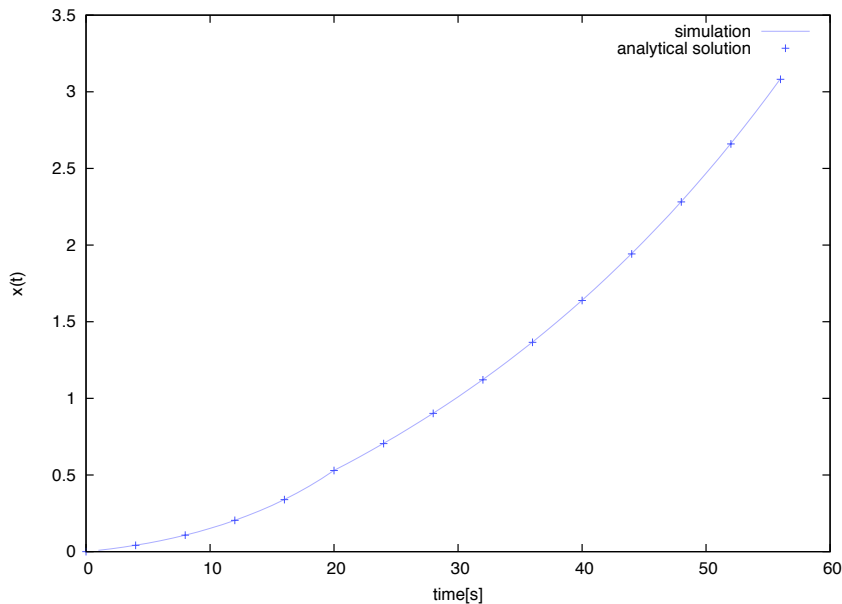


Figure 5.1: Comparison of analytical and numerical solution of the EH algorithm with $a = 5 \cdot 10^{-5} s^{-1}$, $\tau = 20s$, $\lambda = 0.15s^{-1}$, $\beta_{eff} = 0.0065$, $\Lambda = 0$. The bend at $t = 20s$ is clearly visible.

5.2.1 Including temperature feedback

Assume the reactor has been operated at a steady state with a power P_0 for $t < 0$. At $t = 0$ an external reactivity $\rho_e \neq 0$ is introduced by a perturbation (for example, movement of a control rod).

The interesting quantities for our model are the power deviation from a steady-state $x(t)$ (as defined above) together with the changes in temperature $z(t)$ of fuel (index F), coolant (index

C) and coolant inlet (index CI)

$$z_F(t) = \frac{T_F(t) - T_F(0)}{T_F(0) - T_C(0)} \quad (5.7)$$

$$z_C(t) = \frac{T_C(t) - T_C(0)}{T_F(0) - T_C(0)} \quad (5.8)$$

Changes in temperature are calculated by using a point-model approach for fuel and coolant temperatures. Heat accumulation in fuel cladding is neglected and the whole heat is assumed to stay within the fuel rods. Therefore we obtain [16]

$$\Theta_F \frac{d}{dt} z_F(t) = x(t) - z_F(t) + z_C(t) \quad (5.9)$$

$$\Theta_C \frac{d}{dt} z_C(t) = \zeta z_F(t) - z_C(t) + \zeta z_{CI}(t) \quad (5.10)$$

together with

$$\zeta = \frac{T_C(0) - T_{CI}(0)}{T_F(0) - T_{CI}(0)} \quad (5.11)$$

Fuel, coolant and inlet temperatures are characteristic for each reactor type. Assuming the coolant inlet temperature to be constant it shows that $z_{CI} = 0$.

By replacing the time derivatives in equations 5.9 and 5.10 with finite differences and rearranging we obtain

$$z_F(t_n) = \frac{\Delta t [x(t_n) + z_C(t_n)] + \theta_F z_B(t_{n-1})}{\Theta_F + \Delta t} \quad (5.12)$$

and

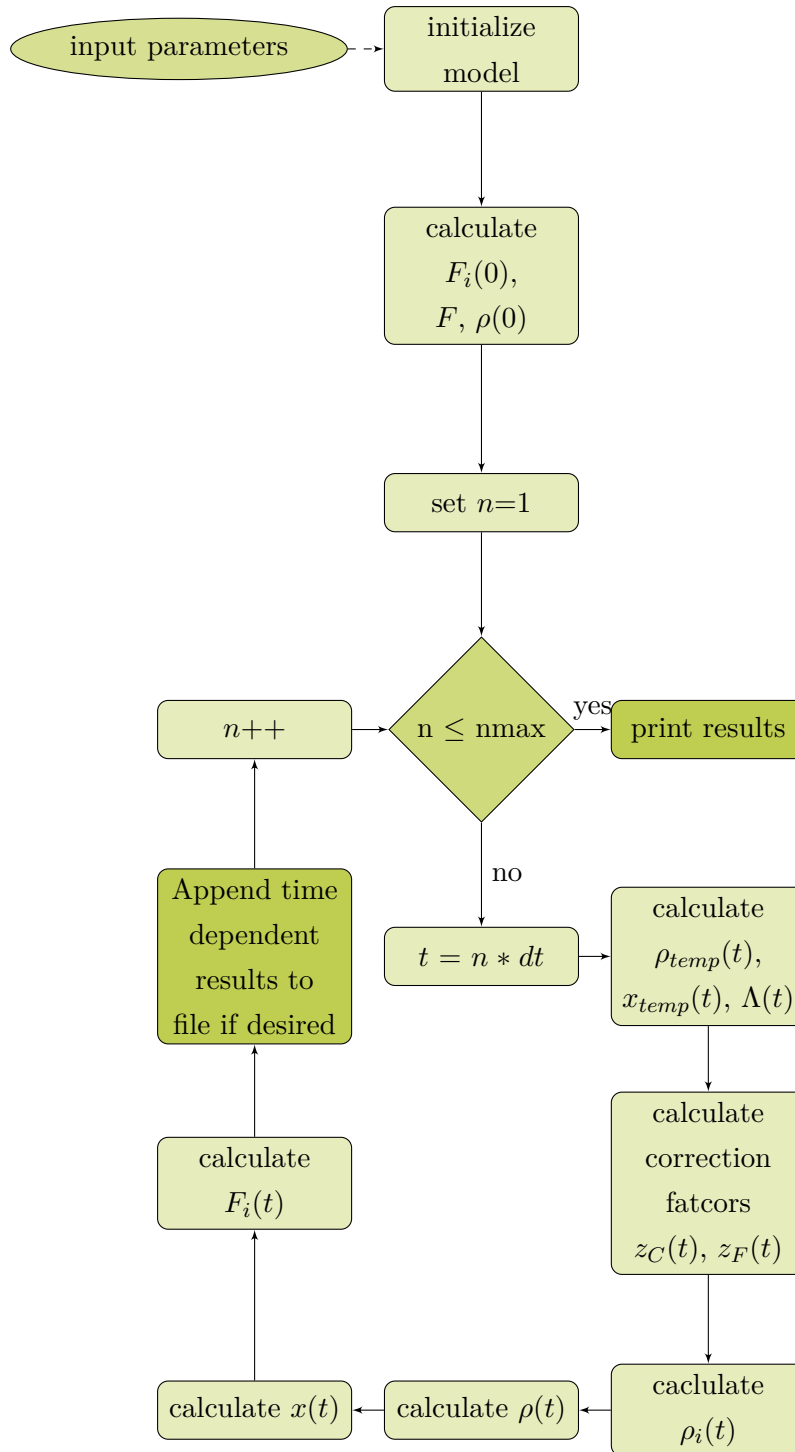
$$z_C(t_n) = \frac{\zeta \Delta t z_F(t_n) + z_C(t_{n-1}) \theta}{\Delta t + \Theta_C} \quad (5.13)$$

The system of equations 4.30, 4.31, 5.9 and 5.10 has to be solved numerically to obtain solutions for the kinetic model including feedback. This is done by integrating equation 4.30 replacing $\rho(t)$ by $\rho_e(t) + \rho_i(t)$ as shown below. As $\rho_i(t)$ is temperature dependent and the temperature changes have to be calculated beforehand, $\rho_i(t_n)$ is replaced by $\rho_i(t_{n-1})$ in a first step and then recalculated with the temperature changes included.

5.3 Description of the algorithm including feedback mechanisms

Expanding the algorithm presented above to include all relevant feedback mechanisms needs taking poisoning effects into account and choosing right parameters suitable to the TRIGA reactor at TU Vienna. This leads to the reactor kinetics model algorithm flowchart shown below. The corresponding equations in their appropriate form suitable for numerical calculations are presented below the flow chart.

5.3.1 Algorithm flow chart



5.4 Algorithm equations and step-by-step instructions

The deviation from steady-state $x(t)$ is calculated as follows:

1. Define all input parameters according to table 5.1.

2. Set $x_0 = 0$ (at the beginning, there is no deviation from steady state.)
3. Calculate the current time t_n by multiplying the iteration number n by dt according to eq. 5.14a.
4. Calculate F and F_0 according to equations 5.14b and 5.14c.
5. Calculate the current, non corrected value for the reactivity $\rho_{temp}(t_n)$ according to eq. 5.14d - 5.14f.
6. Calculate $x_{temp,n}$ according to eq. 5.14g.
7. Calculate fuel and coolant temperature changes z_{F,t_n} and z_{C,t_n} according to eq. 5.14h and 5.14i.
8. Refine the calculation for ρ_i according to eq. 5.14j.
9. Refine the calculation for ρ_n according to eq. 5.14k.
10. Refine the calculation for x_n according to equation 5.14l, using the refined value for ρ_n .
11. Calculate F_n according to eq. 5.14m.

$$t_n = dt \quad n \quad (5.14a)$$

$$F = \frac{\Lambda}{dt} + \frac{\beta}{\lambda dt} (1 - e^{-\lambda dt}) \quad (5.14b)$$

$$F_0 = \frac{\beta}{\lambda dt} (1 - e^{-\lambda dt} (1 + \lambda dt)) x_0 = 0 \quad (5.14c)$$

$$O(x) = \begin{cases} 1 & x \geq 0 \\ 0 & x < 0 \end{cases} \quad (5.14d)$$

$$\rho_e(t) = \rho_e(0) + atO(\tau - t) + a\tau (1 - O(\tau - t)) \quad (5.14e)$$

$$\rho_{temp,n} = \underbrace{\rho_e(\rho_e(0), a, t_n, \tau)}_{\text{external reactivity}} + \underbrace{\rho_{i,n-1}}_{\text{internal reactivity}} \quad (5.14f)$$

$$x_{temp,n} = \frac{\rho_{temp,n} + \frac{\Lambda}{dt} x_{n-1} + F_{n-1} - \rho_0}{F - \rho_{temp,n}} \quad (5.14g)$$

$$z_{F,n} = \frac{\Delta r (x_{temp,n} + z_{C,n-1}) + \theta_B z_{F,n-1}}{\Theta_B + \Delta t} \quad (5.14h)$$

$$z_{C,n} = \frac{\zeta \Delta t z_{F,n} + z_{C,n-1} \Theta_C}{dt + \Theta_C} \quad (5.14i)$$

$$\rho_{i,n} = (T_{F,0} - T_{C,0}) (\alpha_{tF} z_{F,n} + \alpha_{tC} z_{C,n}) \quad (5.14j)$$

$$\rho_n = rho(\rho_0, a, t_n, \tau) + \rho_{i,n} \quad (5.14k)$$

$$x_n = \frac{\rho_n + \frac{\Lambda}{dt} x_{n-1} + F_{n-1} - \rho_0}{F - \rho_n} \quad (5.14l)$$

$$F_n = \frac{\beta}{\lambda dt} \left(1 + e^{-2\lambda dt} - 2e^{-\lambda dt} \right) x_n + e^{-\lambda dt} F_{n-1} \quad (5.14m)$$

5.5 TRIGA specific parameters

Input parameters are taken from literature ([18], [16] and [22]). A compilation of all input parameters can be found in table 5.1. Temporary parameters are parameters used during the calculation and are described in table 5.2. Output parameters are the parameters of interested and can be found in table 5.3.

Table 5.1: Input parameter list

Index	Name	Meaning
1	γ_{Xe}	fission product yield for ^{135}Xe
2	γ_{Sb}	fission product yield for ^{135}Sb
3	γ_{Te}	fission product yield for ^{135}Te
4	γ_I	fission product yield for ^{135}I
5	γ	total fission product yield for reactor poisons
6	λ_{Xe}	half life time for ^{135}Xe
7	λ_I	half life time for ^{135}I
8	ρ	initial reactivity (absolute)
9	β_{eff}	fraction of delayed neutrons (one group approximation)
10	T_C	Initial coolant temperature
11	T_{CI}	Initial coolant inlet temperature
12	T_F	Initial fuel temperature
13	λ	lifetime of delayed neutron parent nuclides (one group approximation)
14	τ	Duration for reactivity change [s]
15	α_C	Temperature feedback coefficient of coolant
16	α_F	Temperature feedback coefficient of fuel
17	Θ_C	Coolant heat removal capacity
18	Θ_F	Fuel heat removal capacity

Table 5.2: List of temporary parameters

Parameter Name	Meaning
$x_{temp}(t)$	power deviation from initial state w/o correction of internal reactivity
$\rho_{temp}(t)$	reactivity at time t w/o correction of internal reactivity
$z_C(t)$	Temperature correction for coolant temperature
$z_F(t)$	Temperature correction for fuel temperature

Table 5.3: Output parameter list

Parameter Name	Meaning
$x(t)$	power deviation from initial state [times]
$\rho(t)$	reactivity at time t (absolute)
$Xe(t)$	Number of ^{135}Xe nuclei at time t
$I(t)$	Number of ^{135}I nuclei at time t
t_s	Time to reach new steady state [s]
x	Power deviation at new steady state [times]

Chapter 6

An algorithm for the automatic analysis of batches of multi-line gamma ray spectra

AN ALGORITHM MUST BE SEEN TO BE BELIEVED. *Donald E. Knuth*

The experimental data generated during this thesis involved more than 2000 gamma ray spectra. This number is much too large to be evaluated by hand effectively. To be able to automate this task, the peak finding algorithm of Mariscotti [19] (which is widely used in commercial nuclide identification programs) has been adapted and expanded.

6.1 The peak search algorithm

The work in this chapter is based on the peak finding algorithm of Mariscotti [19]. This peak finding algorithm is based on the assumption that peaks can be described by Gaussian functions and the background may be approximated by a linear function within short intervals. In such an interval the number of counts as a function of the channel number x is

$$N(x) = G(x) + B + Cx \quad (6.1)$$

where $G(x)$ represents a Gaussian function if a peak is present (and zero otherwise), B and C are constants describing the background. If one assumes that $N(x)$ is a continuous function, the second derivative $N''(x)$ becomes independent of the background and vanishes for any interval in which there is no peak [19]. Therefore peaks are located wherever $N''(x) \neq 0$.

After generating the second difference $D''(x)$ by using the second-difference approximation

$$D(x) := N''(x) = N_s(x-1) + N_s(i+1) - 2N_s(i) \quad (6.2)$$

peak candidates are identified by the condition

$$|D(x)| > c \quad U(x) \quad (6.3)$$

where $U(x)$ is the uncertainty in the original measurement and c is a user defined parameter which reflects search sensitivity.

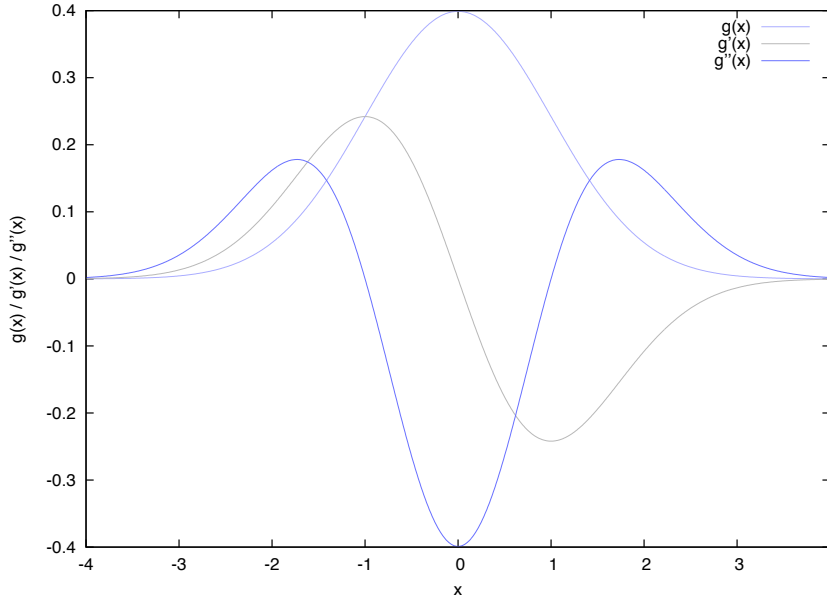


Figure 6.1: The Gaussian function and its first and second derivatives. The second derivative is expected to be found in the derivated spectrum data if a peak is present.

The uncertainty in a single measurement channel containing N counts is easily determined by using the fact that the statistics of radioactive decay are described by the Poisson distribution

$$P(x; \mu) = \frac{\mu^x}{x!} e^{-\mu} = \frac{\mu^x}{\Gamma(x+1)} e^{-\mu} \quad (6.4)$$

with its standard deviation

$$\sigma = \sqrt{N} \quad (6.5)$$

and relative uncertainty

$$\frac{\Delta N}{N} = \frac{\sqrt{N}}{N} = \frac{1}{\sqrt{N}} \quad (6.6)$$

The uncertainty in the original measurement $U(x)$ is therefor equal to \sqrt{N} with N being the counts in the specific channel. The factor c in equation 6.3 can be described as a threshold value: if the second derivative of the signal exceeds this value c plus the initial uncertainty in this parameter, a peak is located.

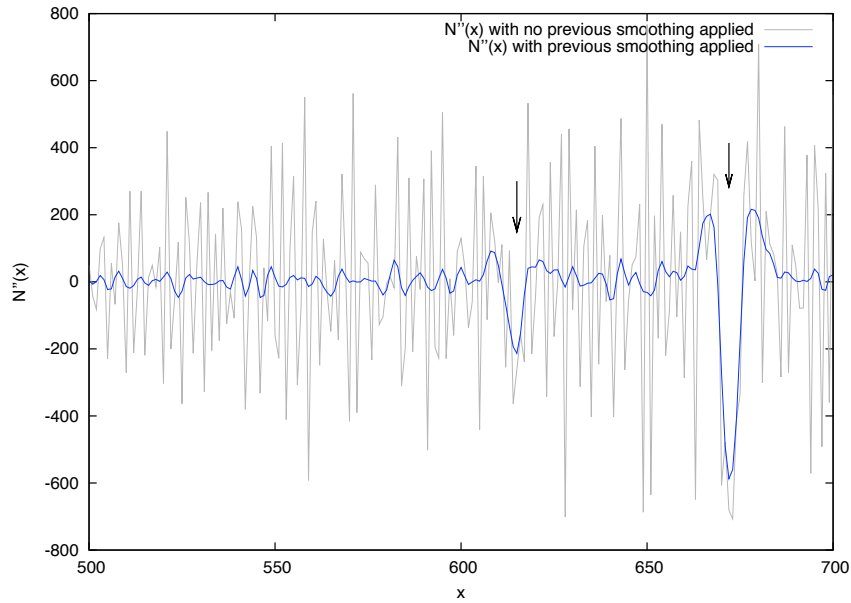


Figure 6.2: Close-up: two peak candidates at $x \approx 615$ and $x \approx 672$, sixth order binomial smoothing filter

The threshold c in equation 6.3 can be investigated by looking at the fluctuations of $D(x)$ in respect to the x -axis. For an ideal spectrum without noise the second derivative $D(x)$ is expected to be of value zero except for areas in which a peak is present. In a spectrum burdened with noise there are fluctuations around the x -axis even with no peaks present. To define a threshold to divide between fluctuations and real peak areas one has to look at the histogram of the values of $D(x)$. There will be a very large amount of values within the fluctuation area and much less values outside this areas. As $G''(x, \mu, \sigma)$ is not symmetrical about the y -axis but dominant in negative values one expects the histogram being biased towards lower values within peak areas. The fluctuation itself is expected to be of Gaussian distribution.

The threshold finding algorithm works best with multipeak spectra: the more peaks the better. An example of such a histogram for a multipeak spectrum can be found in fig. 6.3.

Taking this into account the threshold c can be defined by fitting a Gaussian distribution $G_f(x, \mu, \sigma)$ into the center of the histogram and assume the threshold c to be at 3σ of $G_f(x, \mu, \sigma)$. To fit spectrum data itself using a Gaussian distribution needs two additional parameters a and b as peaks are, like shown above, superimposed with background and measurement uncertainties.

If one wants to fit a peak within a spectrum the function a Gaussian function $G(x, \mu, \sigma)$ is

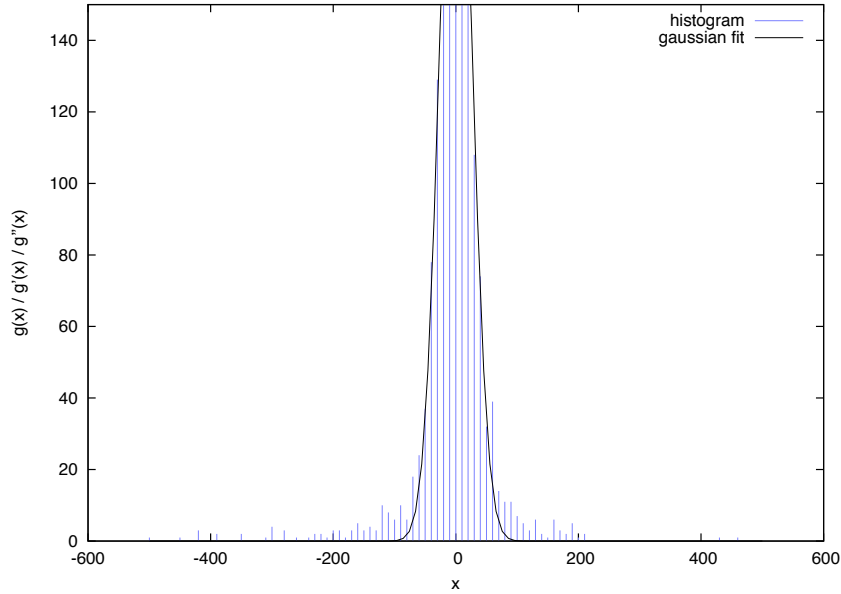


Figure 6.3: Histogram of the distribution of $D(x)$ around zero.

assumed for the fit,

$$G_f(x, \mu, \sigma) = a \frac{1}{\sigma \sqrt{2\pi}} e^{-\frac{(x-\mu)^2}{2\sigma^2}} + b \quad (6.7)$$

and the second derivative of $G()$,

$$G_f''(x) = \frac{ae^{-\frac{(x-\mu)^2}{2\sigma^2}}(x-\mu)^2}{\sqrt{2\pi}\sigma^5} - \frac{ae^{-\frac{(x-\mu)^2}{2\sigma^2}}}{\sqrt{2\pi}\sigma^3} \quad (6.8)$$

is used for analysis as described above.

The minimum of the second derivative is equal to μ , the inflection points of the Gaussian function are located at $x = \pm\sigma$. The maximum of the Gaussian function is located at $x = \mu$ and has the value

$$G(x = \mu) = \frac{1}{\sigma \sqrt{2\pi}} \quad (6.9)$$

The minimum of the second derivative of the Gaussian function is given by

$$G(x = \mu) = -\frac{1}{\sigma^3 \sqrt{2\pi}} \quad (6.10)$$

The next step after identifying peaks itself is identifying their positions which are determined by the local minima of $D(x)$ and their area which is determined by the parameters σ and μ . In practical analysis, the negative part of equation 6.8 is much easier to define and to integrate. As

only the negative part of the second derivative is used for analysis, the ratio of this area to the total peak area have to be defined.

The zero poles of $G''(x, \mu, \sigma)$ are given by

$$G''(x, \mu, \sigma) = 0 \Leftrightarrow x = \begin{cases} \frac{1}{2}(2\mu - \sqrt{2}\sigma) \\ \frac{1}{2}(2\mu + \sqrt{2}\sigma) \end{cases} \quad (6.11)$$

therefore the integral

$$\begin{aligned} & \int_{\frac{1}{2}(2\mu - \sqrt{2}\sigma)}^{\frac{1}{2}(2\mu + \sqrt{2}\sigma)} G''(x, \mu, \sigma) dx \\ = & \int_{\frac{1}{2}(2\mu - \sqrt{2}\sigma)}^{\frac{1}{2}(2\mu + \sqrt{2}\sigma)} \frac{2\sqrt{\frac{2}{\pi}}(x - \mu)^2 e^{-\frac{(x-\mu)^2}{\sigma^2}}}{\sigma^5} - \frac{\sqrt{\frac{2}{\pi}} e^{-\frac{(x-\mu)^2}{\sigma^2}}}{\sigma^3} \\ & = -\frac{1}{\sqrt[4]{e}\sqrt{\pi}\sigma^2} \end{aligned} \quad (6.12)$$

defines the negative part of the negative part of the second derivative, the two positive parts are given by

$$\begin{aligned} & \int_{-\infty}^{\frac{1}{2}(2\mu - \sqrt{2}\sigma)} G''(x, \mu, \sigma) dx \\ = & \int_{\frac{1}{2}(2\mu + \sqrt{2}\sigma)}^{\infty} G''(x, \mu, \sigma) dx \\ & = \frac{1}{2\sqrt[4]{e}\sqrt{\pi}\sigma^2} \end{aligned} \quad (6.13)$$

In the analysis, only the negative part of the integral can be evaluated. The parameters to determine the whole peak area are μ , which is given by the minimum of $G''(x, \mu, \sigma)$ and σ , which can be calculated via equation 6.11 as soon as μ and the values x_1 and x_2 ,

$$x_1 = \frac{1}{2}(2\mu - \sqrt{2}\sigma) \quad (6.14a)$$

$$x_2 = \frac{1}{2}(2\mu + \sqrt{2}\sigma) \quad (6.14b)$$

are known, where x_1 and x_2 are determined numerically for each interesting peak region. The value for σ for the peak in question is then

$$\sigma = \sqrt{2}(x - \mu) \quad (6.15)$$

The maximum of the peak in question is determined by the maximum of the Gaussian function, located at $x = \mu$, multiplied by its amplitude A_1 . To obtain the multiplication factor between the calculated minimum of the second derivative (also located at $x = \mu$) the relation between the maximum of the peak to the minimum of the second derivative (given by the measured value A_2) of the same peak is needed. The maximum of the peak is given by

$$G(x = \mu, \mu, \sigma) = \frac{A_1}{\sqrt{2\pi}\sigma} \quad (6.16)$$

the minimum of the second derivative of this peak is given by

$$G''(x = \mu, \mu, \sigma) = -\frac{\sqrt{\frac{2}{\pi}} A_2}{\sigma^3} \quad (6.17)$$

The value of eq. 6.17 is given by the measurement data. As a moving average filter over six values (for details, see next section) is used to smooth the second derivative after calculating it numerically, the minima of the second derivatives used for evaluation are expected to be biased towards a value closer to the x-axis. This bias has to be evaluated numerically by comparing the minima of the smoothed versus the values of the non-smoothed values. This is done via comparing the minima before and after smoothing to obtain the multiplication factor between them.

By multiplying the bias-corrected values of the minima of the second derivatives with the factor

$$\frac{\frac{A}{\sqrt{2\pi}\sigma}}{-\frac{\sqrt{\frac{2}{\pi}} A}{\sigma^3}} = -\frac{\sigma^2}{2} \quad (6.18)$$

the correct value for $G(x = \mu, \mu, \sigma)$ can be calculated.

6.2 Enhancing signal quality for analysis: smoothing

Application of second-derivative methods for peak finding is limited by statistical noise introduced by the measurement equipment. This noise has to be filtered out before peak searching to get reasonable results. A suitable filter for this task is binomial smoothing [20], also called the moving average.

For example consider fig. 6.4. In the upper part of the plot the input data $N(x)$ (blues) and the smoothed data $N_s(x)$ (red) are shown. In the lower part the second derivatives $N_s''(x)$ for previously smoothed input data (blue) and the nonsmoothed data $N''(x)$ (fuchsia) are shown. It is clearly visible that the second derivative of the previously non-smoothed data is dominated by noise and cannot be analyzed easily. Figure 6.5 shows a close-up of the second derivatives for a fourth order binomial smoothing filter.

Choosing the order of the binomial smoothing filter is essential to maintain data integrity during evaluation and analysis. The choice is made based on efficiency of peak detection during a systematic investigation of peaks detection with various input data (high, medium and low dose rate measurements short after reactor shutdown, after about a day and after three days without operation).

The parameter σ depends on the detector type and channel number and can be determined by investigating each peak within one pulse height spectrum. Investigation means fitting each peak using function 6.7 and fitting the resulting σ versus channel number linearly. The data points used for the linear fit can be found in table 6.1, plots of the Gaussian shape fits in figure 6.7. The original spectrum used for the standard deviation fits is shown in fig. 6.6.

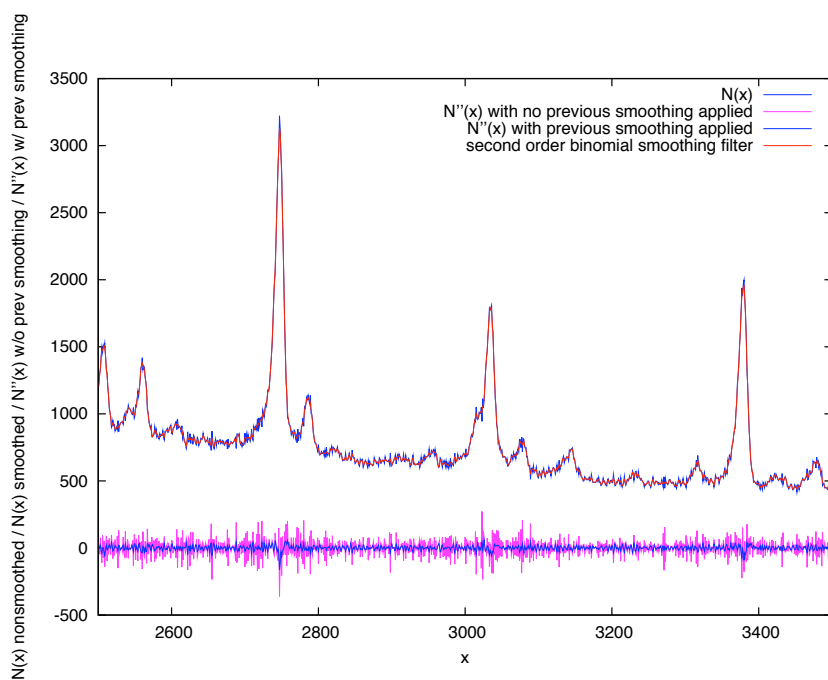
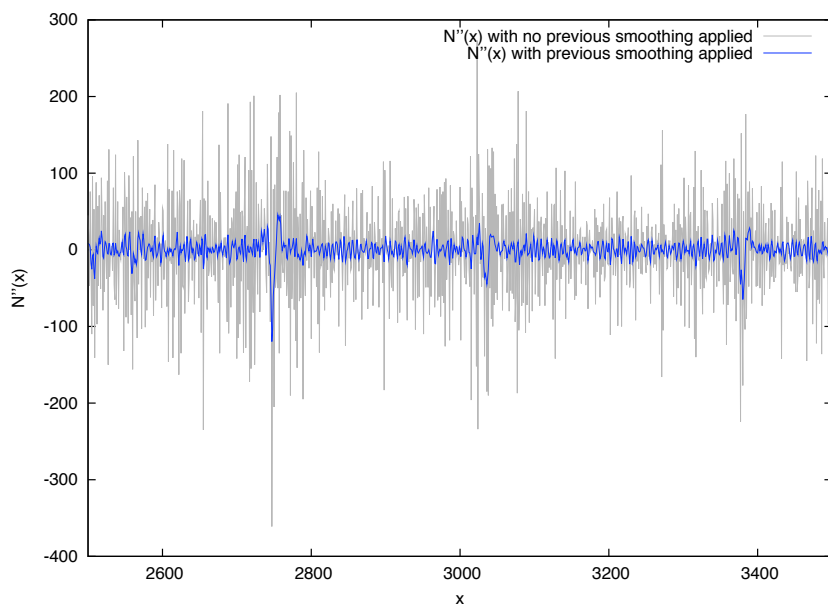
Figure 6.4: $N(x)$ and $N''(x)$ for unsmoothed versus smoothed input data

Figure 6.5: Close-up: comparison of the second derivatives of previously smoothed vs. unsmoothed input data, fourth order binomial smoothing filter

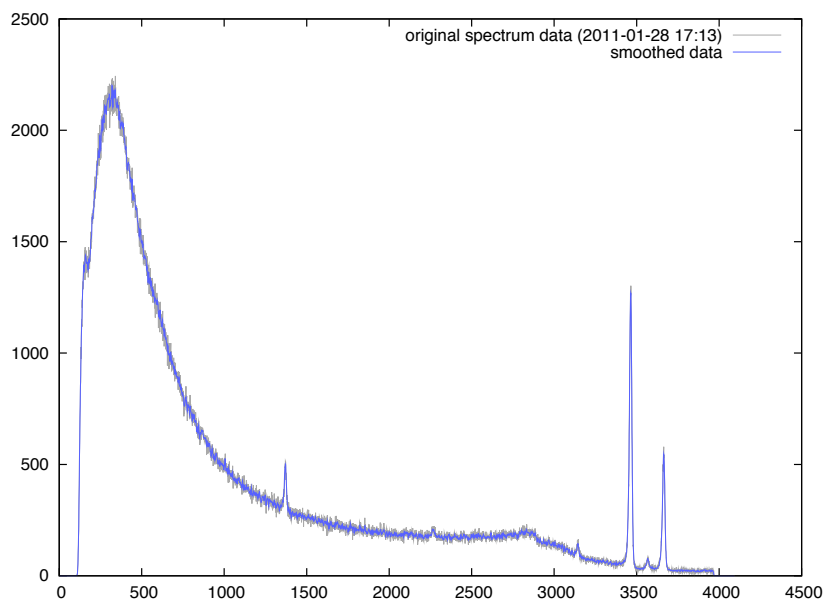


Figure 6.6: Original spectrum data and smoothed spectrum used for the standard deviation fits. After calibration the leftmost peak is at 511 keV (annihilation single escape), 1293.6 keV (^{41}Ar) and 1368.63 keV (^{24}Na)

Table 6.1: Standard deviation data points

channel number	standard deviation
1370.57	4.83175
3463.5	7.17422
3663.8	7.20697

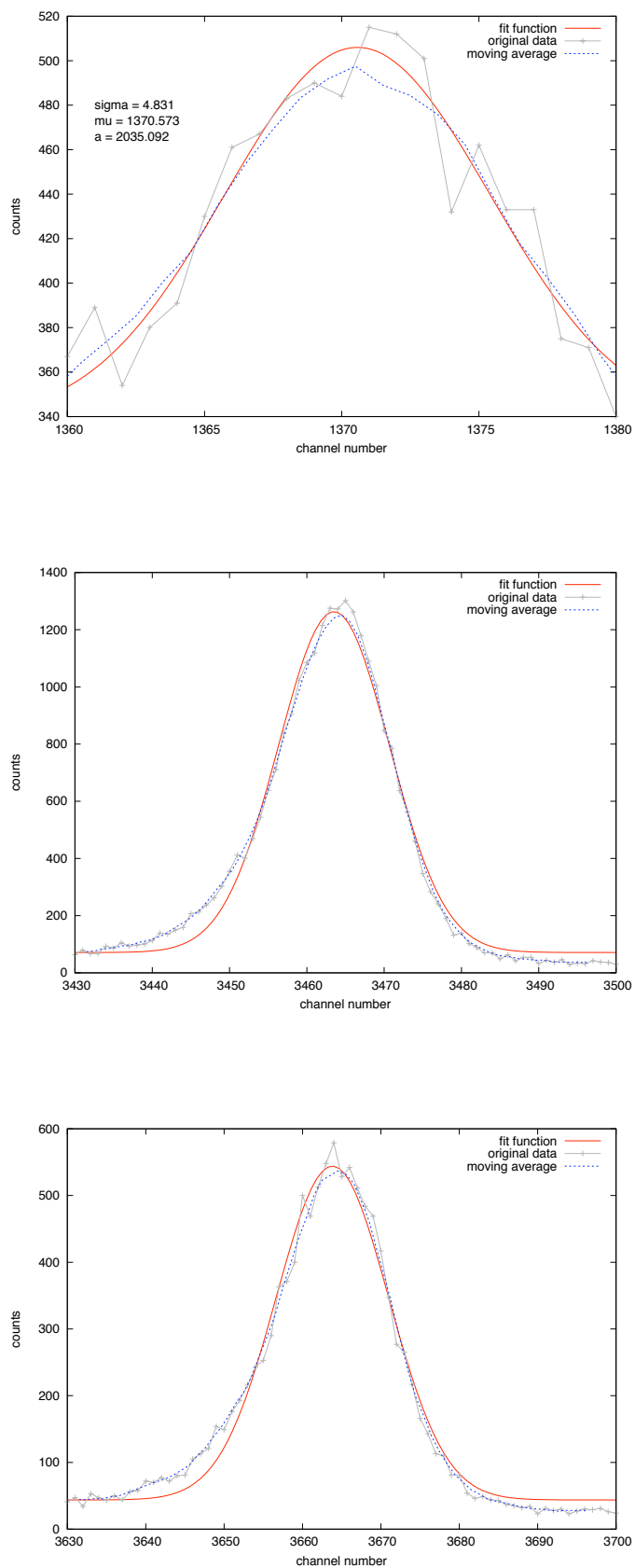


Figure 6.7: Peak fits to obtain the standard deviation versus channel number

6.2.1 Detailed description of the algorithm

After identifying the number of spectra to be processed each spectrum file is read in, eventually converted to a comfortable data format for later viewing and the spectrum data itself is stored in a list L of lists N_i . Each list N_i is filtered and the second derivative N_i'' is calculated. Each N_i'' is then searched for local minima below a threshold c . If such a minimum is encountered, the position μ , amplitude a and the standard deviation σ are appended to a list of peak candidates. This list of peak candidates is saved for post-processing (e.g. for validation, visualization or statistical evaluation).

Post-processing involves the calculation of the mean of the peak positions for each peak candidate (the channel number is expected to shift during the measurements), determining the peak minima, enhancing the signal quality of the second derivatives and calculating the bias of the enhanced signals. For each peak, the parameters μ , σ and the amplitude A is calculated, then the actual peak area can be determined.

This gives us, for each nuclide present in the measurement data, the peak areas for each time step and can be used to find all peaks and their behavior with respect to time leading to the possibility of the calculation of the half-life time.

Chapter 7

Numerical simulations

BEWARE OF BUGS IN THE ABOVE CODE; I HAVE ONLY PROVED IT CORRECT, NOT TRIED IT. *Donald E. Knuth, 1977*¹

7.1 The MCNP models

7.1.1 Generic model data

For all further considerations MCNP and the algorithm described in section 5.3 have been used depending on the specific problem statement (either solely or both methods combined).

The MCNP models used during the calculations were based on the model developed by R. Khan in his thesis [25]. This basis was modified concerning the temperatures of fuel, cladding and water, the geometry of the core and the tallies of demand. An overview of the model can be found in figures 7.1 to 7.3.

¹Donald Knuth's webpage (<http://www-cs-faculty.stanford.edu/~knuth/faq.html>) states the line was used to end a memo entitled *Notes on the van Emde Boas construction of priority deques: An instructive use of recursion*.

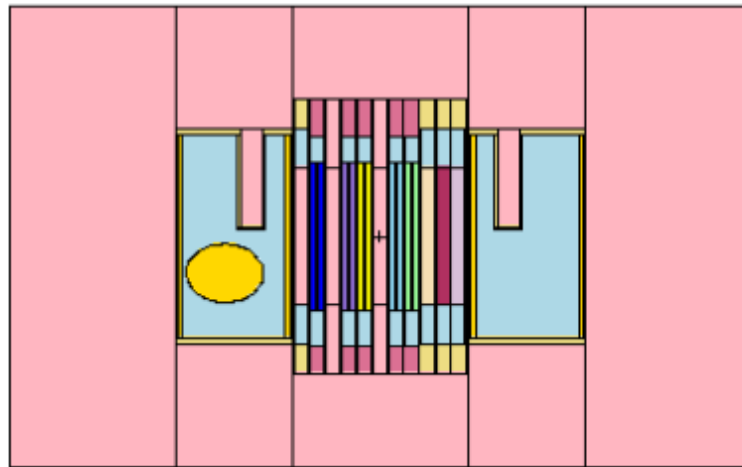


Figure 7.1: The MCNP model for the TRIGA Mark II reactor Vienna shown as xz plane view

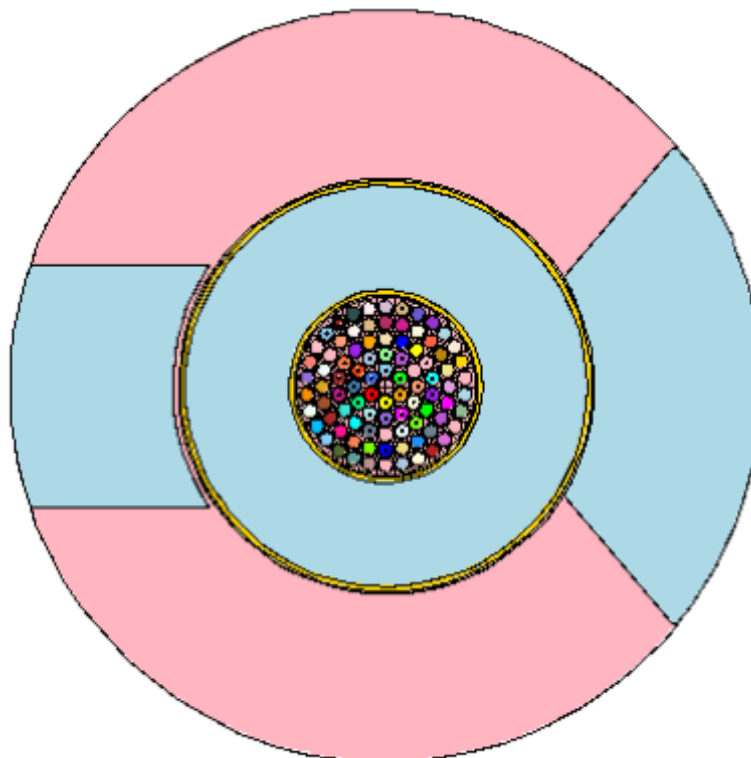


Figure 7.2: The MCNP model for the TRIGA Mark II reactor Vienna shown as xy plane view

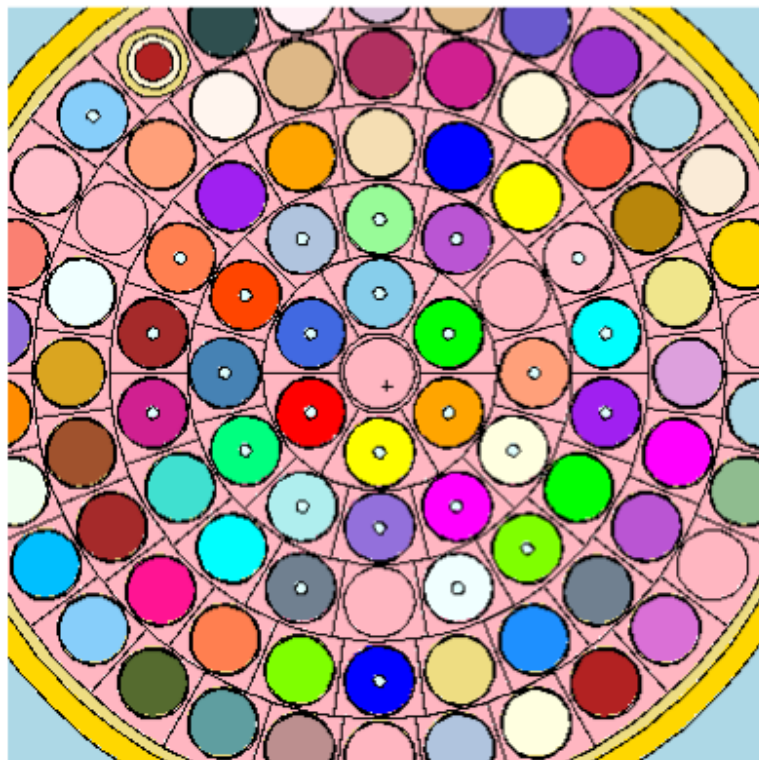





Figure 7.3: The MCNP model for the TRIGA Mark II reactor Vienna shown as xy plane view (zoomed to core)

7.1.2 Core layout

The layout of the current standard core is presented in fig. 7.4. This is the layout used for everyday operation. For certain issues like lab courses the core layout is changed to ensure proper reactor behavior for the experiments to be performed. For the shim rod calibration experiment performed on January 10th, 2011 the core has been modified by moving some of the FLIP type elements from ring B to ring C. The resulting layout is shown in fig. 7.5. The fuel type color scheme is outlined in table 7.1.

Table 7.1: Color coding for the fuel elements

	Fuel type 102
	Fuel type 104
	FLIP fuel

The three control rods in the core are labeled as *RR* (regulating rod), *SR* (shim rod) and *TR* (transient rod) in the schematics below. Element F28 is the neutron source (labeled as *Q*). Element F09 is a graphite element (labeled as *GE*).

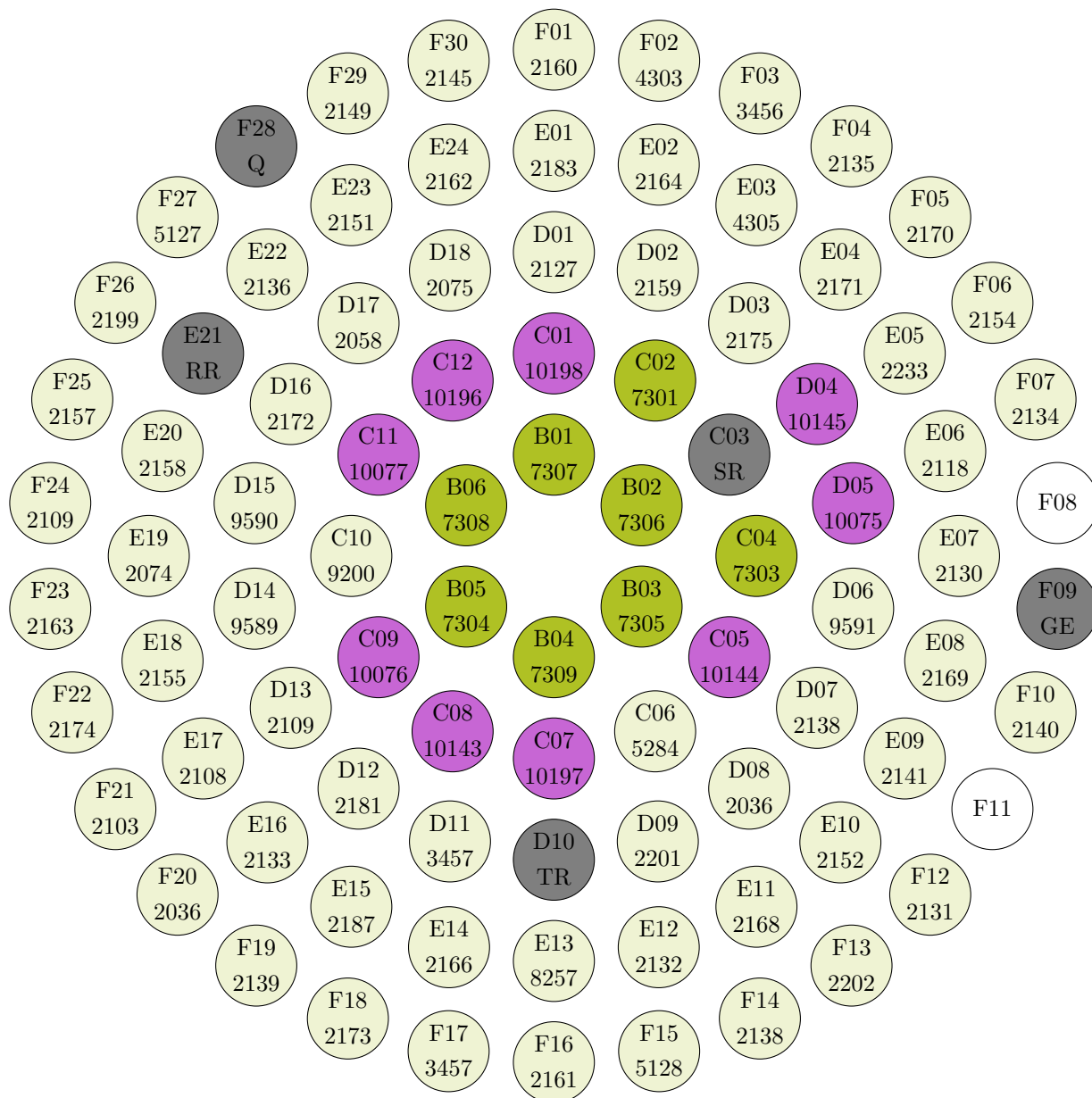


Figure 7.4: Current (standard) core layout of the TRIGA reactor Vienna. Each fuel element is numbered according to its position in the core, reflected in the upper numbers; the lower number indicates both fuel type (see chapter 3) and a element-specific numbering, reflected in the lower numbers.

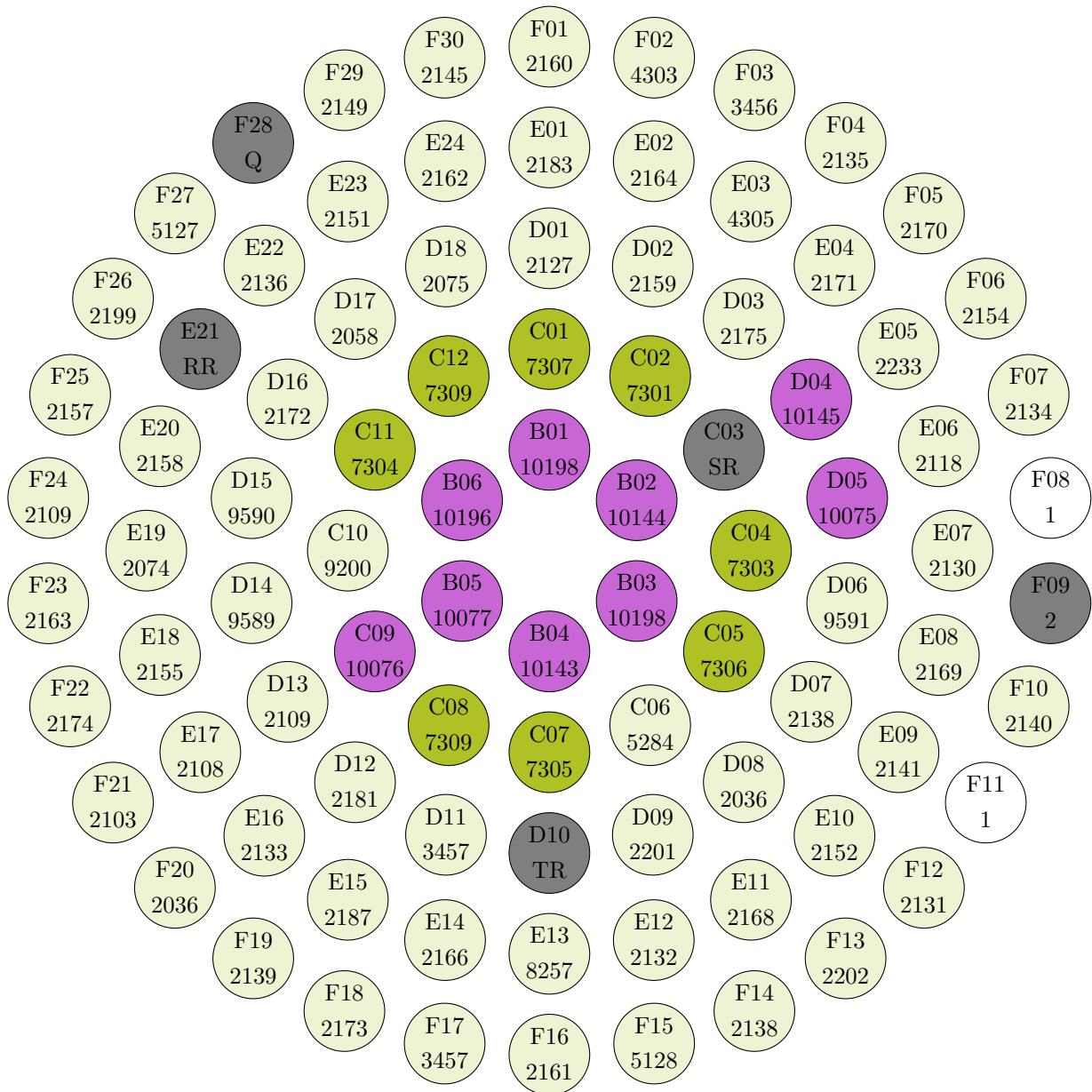


Figure 7.5: Core layout of the TRIGA reactor Vienna during the lab course in January 2011

7.2 Automatic generation of MCNP input files

For systematic investigations of the influence of changes in core layout, temperature or the repositioning of control rods a relatively large amount of input files - one for each problem statement, even if this just implies small changes in the input file - has to be created. If this files are created manually the chance of introducing errors is relatively high. For example, the swap of two fuel rods could result in small typing errors with large impact on the result which might not even be recognized as faulty input. The quality of the input data truly is an essential factor. Secondly, the content of the input files is constant for large areas, for example the material definitions do not change for the same material from one problem statement to another. To reduce the risk of errors the input files have been generated automatically following the scheme presented below.

7.2.1 Cell cards

There are cell cards for each fuel type (102, 104 and FLIP).

Fuel type 102

There is a total of 54 fuel rod elements of type102 with indices 1 to 489. Each of them is composed of the following cards:

```
INDEX <FUEL ROD NUMBER> -6.21 -2 7 -3 u=<FUEL ROD NUMBER> \
tmp=<TEMPERATURE> imp:n=1 (Fuel cell)
INDEX <FUEL ROD NUMBER>0 -2.85 -2 3 -4 u=<FUEL ROD NUMBER> imp:n=1 \
tmp=<TEMPERATURE> (upper Sm-disc)
INDEX <FUEL ROD NUMBER>0 -2.85 -2 8 -7 u=<FUEL ROD NUMBER> imp:n=1 \
tmp=<TEMPERATURE> (lower Sm-disc)
INDEX 1 -1.53 -2 4 -5 u=<FUEL ROD NUMBER> imp:n=1 tmp=<TEMPERATURE> \
(upper graph. refl.)
INDEX 1 -1.53 -2 9 -8 u=<FUEL ROD NUMBER> imp:n=1 tmp=<TEMPERATURE> \
(lower graph. refl.)
INDEX 2 -2.7 2:-9:5 u=<FUEL ROD NUMBER> imp:n=1 tmp=<TEMPERATURE> (Al-clad)
```

FLIP fuel

There is a total of 8 fuel rod elements of type FLIP with indices 309 to 363. Each of them is composed of the following cards:

```
INDEX 6 -5.8674 -45 48 -46 u=<FUEL ROD NUMBER> imp:n=1 tmp=TEMPERATURE \
central Zr rod)
INDEX <FUEL ROD NUMBER> -5.867 45 -44 48 -46 u=<FUEL ROD NUMBER> imp:n=1 \
tmp=TEMPERATURE (Fuel cell)
INDEX <FUEL ROD NUMBER>0 -10.28 -44 -48 50 u=<FUEL ROD NUMBER> imp:n=1 \
tmp=TEMPERATURE (lower Mb disc)
```

```

INDEX 1 -1.60 -44 -50 49 u=<FUEL ROD NUMBER> imp:n=1 tmp=\
TEMPERATURE (lower graphite reflector)
INDEX 1 -1.60 -44 46 -47 u=<FUEL ROD NUMBER> imp:n=1 tmp=\
TEMPERATURE (upper graphite reflector)
INDEX 5 -7.9 44:47:-49 u=<FUEL ROD NUMBER> imp:n=1 tmp=TEMPERATURE \
(SS Clad)

```

Fuel type 104

There is a total of 21 fuel rod elements of type 104 with indices 309 to 363. Each of them is composed of the following cards:

```

INDEX 6 -5.8624 -45 48 -46 u=<FUEL ROD NUMBER> imp:n=1 tmp=TEMPERATURE \
(Central Zr rod)
INDEX <FUEL ROD NUMBER> -5.8624 45 -44 48 -46 u=<FUEL ROD NUMBER> imp:n=1\
tmp=TEMPERATURE (Fuel cell)
INDEX 73010 -10.28 -44 -48 50 u=<FUEL ROD NUMBER> imp:n=1 tmp=TEMPERATURE \
<FUEL ROD NUMBER>-lower molydisc
INDEX 1 -1.60 -44 46 -47 u=<FUEL ROD NUMBER> imp:n=1 tmp=TEMPERATURE \
(upper gr. refl.)
INDEX 1 -1.60 -44 -50 49 u=<FUEL ROD NUMBER> imp:n=1 tmp=TEMPERATURE \
(lower gr. refl.)
INDEX 5 -7.9 44:47:-49 u=<FUEL ROD NUMBER> imp:n=1 tmp=TEMPERATURE (SS clad)

```

Core layout

After the different rod types the core layout is defined. The TRIGA core consists of 83 fuel elements, three control rods (the shim rod at position C03, the transient or safety rod at position D12 and the regulating rod at position E21), currently one graphite element at F09 and a neutron source positioned at F28. The positioning of the fuel elements in reactor rings B and C depends on the reactor operation mode (for example, during lab courses the HEU elements are moved from B to the C ring).

The location of each element, the spatial definitions and the indices remain constant but the universe which fills the specific rod position varies as does the temperature. An example (position B1) is given below.

```

INDEX like 522 but trcl (0 4.2 0) fill=<UNIVERSE NUMBER> imp:n=1 (B01)
INDEX1 3 -1 -30 29 -6 10 201 202 INDEX001 imp:n=1 tmp=TEMPERATURE

```

For the core a data structure holding the MCNP universe to fill each position with is defined. This allows easy modifications to implement core changes. Temperature of fuel rods, cladding and water is assumed to be constant over the whole core and during the simulation. It is calculated on basis of the current reactor power.

Elements with little adjustments

The core water, the reflector, the groove, the thermal and thermalising column and the beam ports are adjusted just for temperature. An example is given below.

```
INDEX 3 -1 -34 -42 6 imp:n=1 tmp=TEMPERATURE (water above core)
INDEX 3 -1 -34 -10 43 imp:n=1 tmp=TEMPERATURE (water below core)
```

Elements which remain constant

The graphite elements, water, neutron source and the regulating rods (RR, SR and TR) remain constant for each problem statement.

7.2.2 Surface cards

Surface cards define the surfaces the cells are composed of. For example, cell C3 consists of all surfaces defining the shim rod: two cylinders for the outer (cladding) and inner (boron carbide) and their limiting surfaces (upper and lower boundaries). If a surface card changes or stays constant depends on the problem statement. For example, if a shim rod calibration curve is calculated, k_{eff} has to be calculated for different positions of this rod and therefor the limiting surfaces will vary in the z direction while the radii will stay constant.

7.2.3 Material and tally cards

The material definitions stay constant as no material dependent problems are considered in this thesis. The number of histories to calculate is implemented as a variable to allow easy changes. For each run, a new random seed is generated to avoid identical simulations in different runs (for example to generate multiple output values for identical input data to investigate simulation uncertainties).

7.3 Temperature influence on k_{eff}

The MCNP model is equipped with values for fuel, cladding and water temperatures. The input values are generated using functions fitted to experimental data described in chapter 8. To verify this temperature assumptions the influence of the parameters has been investigated by calculating k_{eff} values in the interesting ranges for temperature values based on experimental data as well as fixed values for a single state.

In MCNP, kT is used to denote the thermal temperature of a cell and use units of MeV [1]. The

following formula can be used to provide the values of kT for temperatures in degrees Celsius:

$$kT[\text{MeV}] = 8.617 \times 10^{-11}(T[\text{C}] + 273.15) \quad (7.1)$$

7.4 Uncertainty analysis and runtime

Uncertainty analysis for the calculations using MCNP can be done only by analyzing the statistical fluctuations of the simulation results. Systematic uncertainties like uncertainties introduced by cross section libraries and the code package itself cannot be quantified except by comparison to actual experiments.

To quantify the uncertainty of the simulation results iterative calculations have been done together with different input parameters, especially with different numbers of cycles in kcode calculations and different numbers of particles per cycle. The repetitive results have been compared against each other and to their mean and standard deviation.

For a variation of the number of particles per cycle between $N = 10^2$ and $N = 10^5$ the standard deviation of the simulation result ranges between 0.026 and 0.0001. A graphical representation of the accumulated data can be found in fig. 7.6.

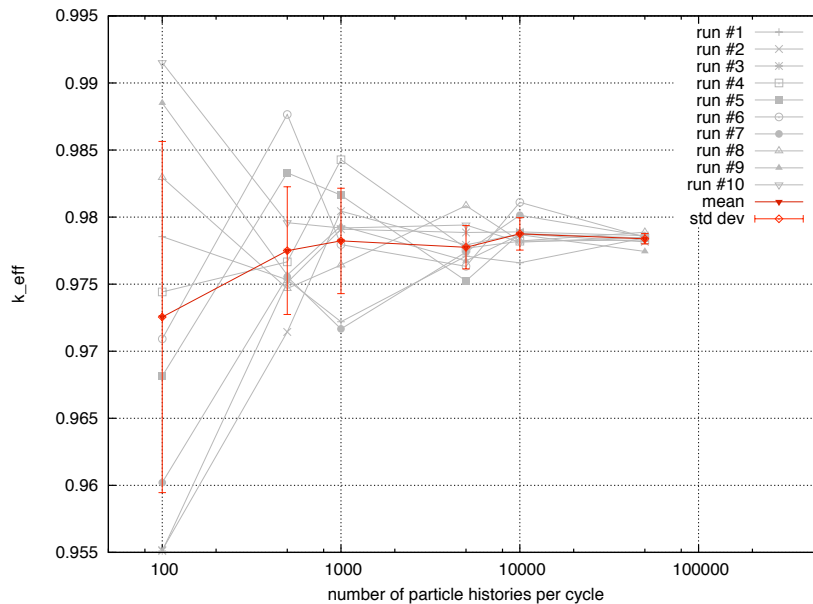


Figure 7.6: Uncertainties in the simulation results

At the same time, the runtime for the simulation versus the number of particles per cycle were analyzed to provide a solid basis for the optimization of how many particles per cycle have to

be considered to get a reproducible result together with not exceeding the available computing time. Figure 7.7 shows a graphical representation of the experimental data.

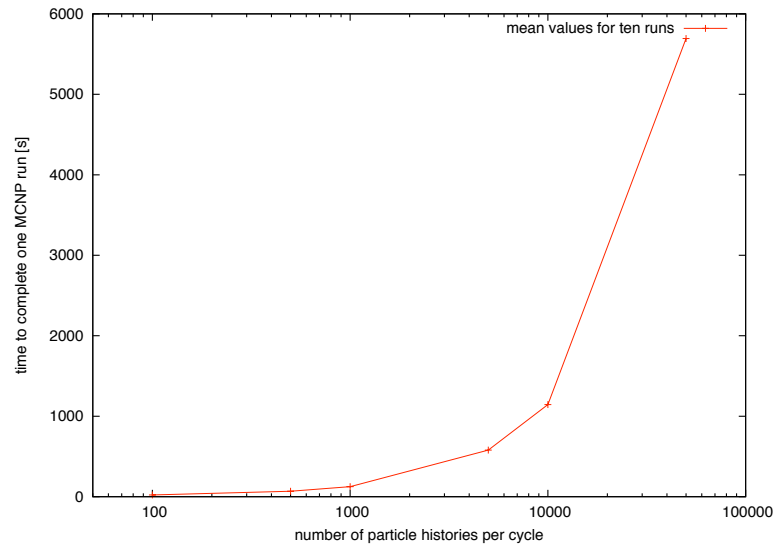


Figure 7.7: Computing time needed for different numbers of particles per cycle

The graphical representation of the computing time needed versus the resulting standard deviation shows a double logarithmic dependency shown in fig. 7.8.

7.5 Reactivity feedback

It has been implemented in the PERL programming language and applied to various reactor states from cold shutdown status to conditions which caused the reactor to automatically shut-down itself.

Each run is started from the conditions of the stable phase of the run before including the whole new parameter set.

7.5.1 Reactivity

The negative temperature feedback α_T coefficient of the TRIGA reactor fuel is strongly temperature dependent [18]. Typical values are in the range of $-7\text{E}^{-5} \Delta\text{k}$ per degree Celsius. As the numerical simulations are performed at various temperatures, an average value cannot be used. Figure 5 of ref. [18] contains information about this parameter in a graphical form. The data contained in this figure is linear in the interesting temperature range (30 - 100 C) and has been

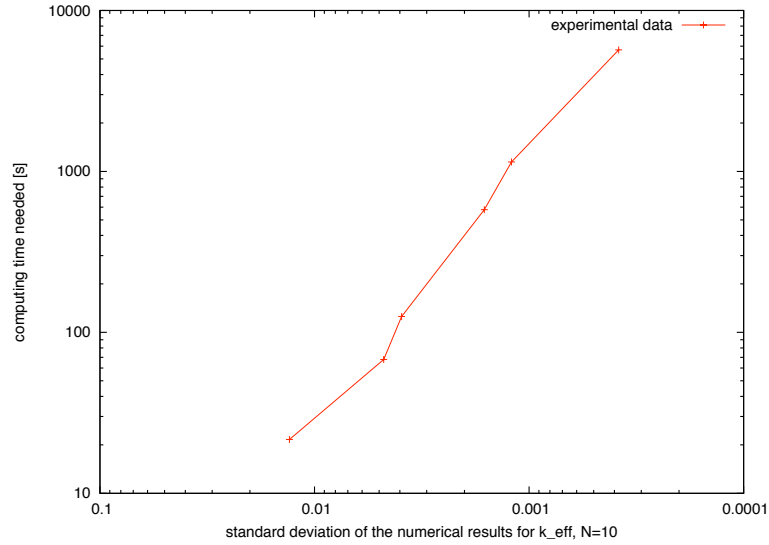


Figure 7.8: Computing time needed for different numbers of particles per cycle versus the resulting uncertainties of the numerical results

extracted and fitted linearly resulting in the following equation:

$$\alpha_F(T) = 2.96025(\pm 0.02735) + 0.0209174(\pm 0.0002119)T \quad (7.2)$$

7.5.2 Temperature

Fuel temperature at various power levels can be calculated by using MCNP (for a steady state) or the algorithm described in section 5.3 (further just called 'the algorithm' or the 'algorithmic version') if starting from a steady state with a given initial temperature. The advantage of using the algorithmic version is that one can obtain data about temperature development with time and it is a lot faster than Monte Carlo methods.

7.6 Systematic parameter investigation

Parameters 1-7, 9 and 13 (see table 5.1) are given in literature and are static values. The parameters 8, 10-12 and 14-18 are dependent on the nature of the problem investigated and defined by the steady state which is started from.

So the parameters to be varied are the initial internal reactivity $\rho(0)$ (par. 8), the initial temperatures for coolant $T_C(0)$ (par. 10), coolant inlet $T_{CI}(0)$ (par. 11) and fuel $T_F(0)$ (par. 12), the duration for the reactivity change τ (par. 14), the temperature feedback coefficients of fuel

α_F (par. 15) and coolant α_C (par. 16) and the heat removal capacities for coolant Θ_F (par. 17) and fuel Θ_C (par 18.). Parameters 8, 10-12 and 14-15 are given by the problem statement and/or literature but the heat removal capacities cannot be found in literature. there are values for standard BWR and PWR designs and power levels but not for the TRIGA reactor.

The heat removal capacities are of the form [16]

$$\Theta_F = V_F \rho_F c_{p,F} R_{F,C} \quad (7.3)$$

and

$$\Theta_C = V_C \rho_C c_{p,C} R_{F,C} \zeta \quad (7.4)$$

with V being the respective volume, ρ being the densities and $R_{F,C}$ being the thermal resistance between fuel and coolant. The parameters are temperature dependent as R is temperature dependent.

According to [16] the thermal flux through a surface S_j can be described using the relation

$$q_j S_j = \frac{T_j - T_{j+1}}{R_j} \quad (7.5)$$

with q_j being the average thermal flux density on the surface S_j , T_j and T_{j+1} being the temperatures of the respective zones j and $j + 1$ and R_j being the thermal resistance of zone j . The interesting quantity is the thermal resistance given in Kelvin per Watt.

The thermal flux density is defined as the rate of heat energy transfer through a given surface. The SI derived unit of heat rate is [$\frac{J}{s} = W$]. Heat flux is the heat rate per unit area. In SI units, heat flux is measured in units of [$\frac{W}{m^2}$]. Heat rate is a scalar quantity, while heat flux is a vectorial quantity. To define the heat flux at a certain point in space, one takes the limiting case where the size of the surface becomes infinitesimally small.

The heat removal capacities are clearly temperature dependent as the amount of heat transferred from one system (e.g. a rod) to another (e.g. the surrounding water) varies with the initial temperature difference between them. To get an idea of the dependency of the heat removal capacity on temperature the initial difference between fuel and coolant temperature, the heat transfer equation

$$\frac{\partial}{\partial t} u(t, \vec{r}) + \alpha \Delta u(t, \vec{r}) = 0 \quad (7.6)$$

has been solved numerically using just one dimension in space as the problem is considered to be symmetrical in z and in y assuming cylindrical rods. Different parameters α for fuel and coolant have been considered. The initial conditions can be found in fig. 7.11, the boundary conditions were set to $u(t, 0) = u(0, 0)$ and $u(t_{max}, 0) = u(0, 0)$. With this boundary conditions one can estimate an equilibrium established after a certain period of time which is of the form of $u(\infty, x) = a + bx$ well-defined by the values $u(\infty, 0)$ and $u(\infty, x_{max})$. The parameter of interest is the time to reach this steady state with different initial conditions for the temperature T_1 (in $x \in [0, 5]$) and T_2 (in $x \in (5, 10]$). The example for initial conditions in fig. 7.11 shows T_1 equal to 55 °C (fuel temperature) and T_2 equal to 23 °C (coolant temperature).

The assumed relationship for α_{TF} does not really hold for comparisons with experiments, the factor is off. The reason is probably that the fuel used in the specific reactor is not a standard fuel but a mixture of three fuel types, so the negative feedback coefficients for different fuel temperatures have to be considered to be the values found in literature plus an additional yet unknown correction factor (called c_{α_F} below). To determine this correction factor the results from numerical calculations have been compared to actual experiments. It clearly shows a quadratic deviation with a minimum at about 60 °C.

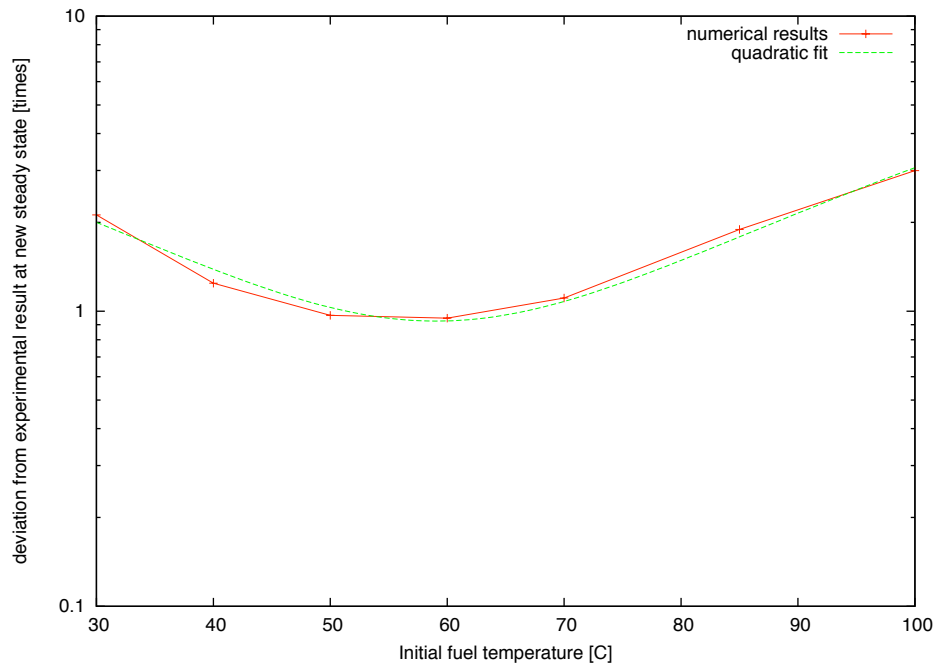


Figure 7.9: Deviation from experimental results

Table 7.2: Deviations from experimental results as shown in fig. 7.9

Initial fuel temperature [C]	Deviation [times]
30	2.1195
40	1.24476
50	0.967913
60	0.947309
70	1.1082
85	1.89333
100	2.99501

To determine this factor in dependence of the fuel temperature (as α_{TF} is temperature dependent the correction factor is assumed to be temperature dependent itself) calculations have been made to clarify the influence of a multiplication factor applied to α_{TF} during a calculation. The result is shown in fig. 7.10 and shows less influence relative the more this factor is increased.

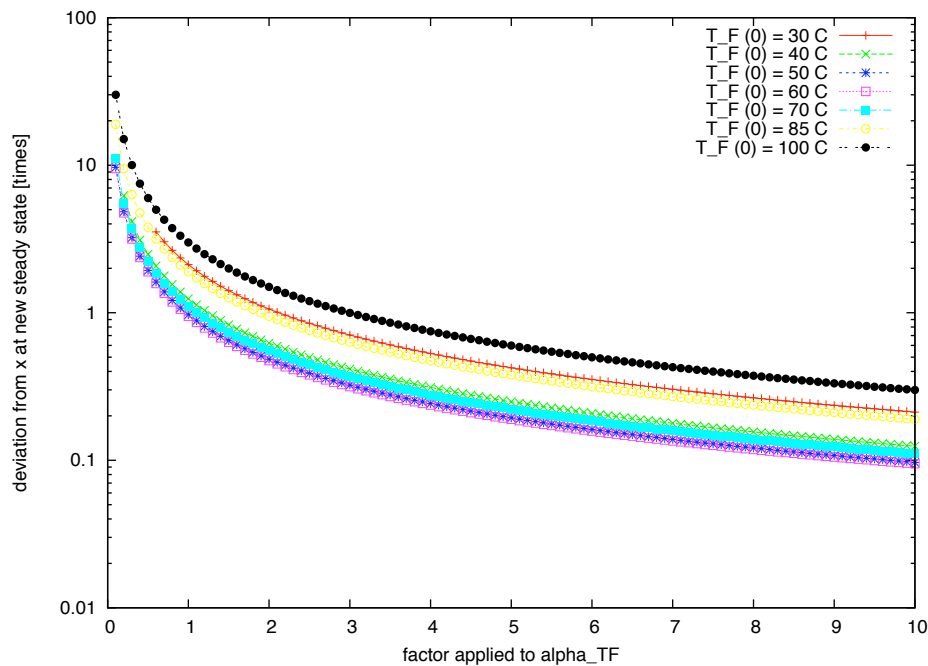


Figure 7.10: The influence of a multiplication factor applied to α_{TF} once per calculation.

Numerical solutions of the heat equation have been obtained by using Mathematica [23]. An iteration for fuel temperatures from 30 °C to 180 °C for a fixed coolant temperature of 23 °C has been performed by solving the partial differential equation 7.6 resulting in an interpolating function $u(t, x)$. The time derivatives of the results $u(t_{max}, x = 4.9)$ and $u(t_{max}, x = 5.1)$ have been analyzed numerically to obtain the times until they reach a steady state. The results are shown in fig. 7.12.

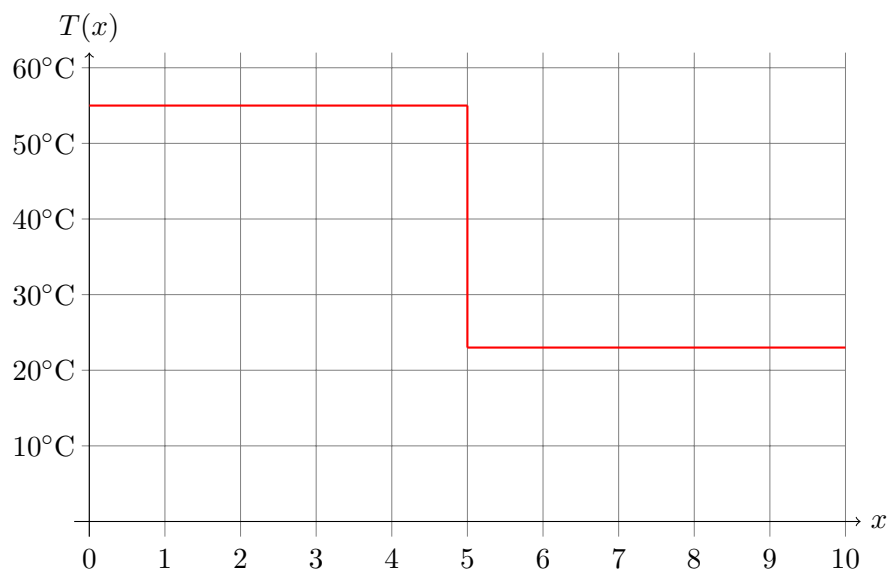


Figure 7.11: Initial conditions for the heat transfer model

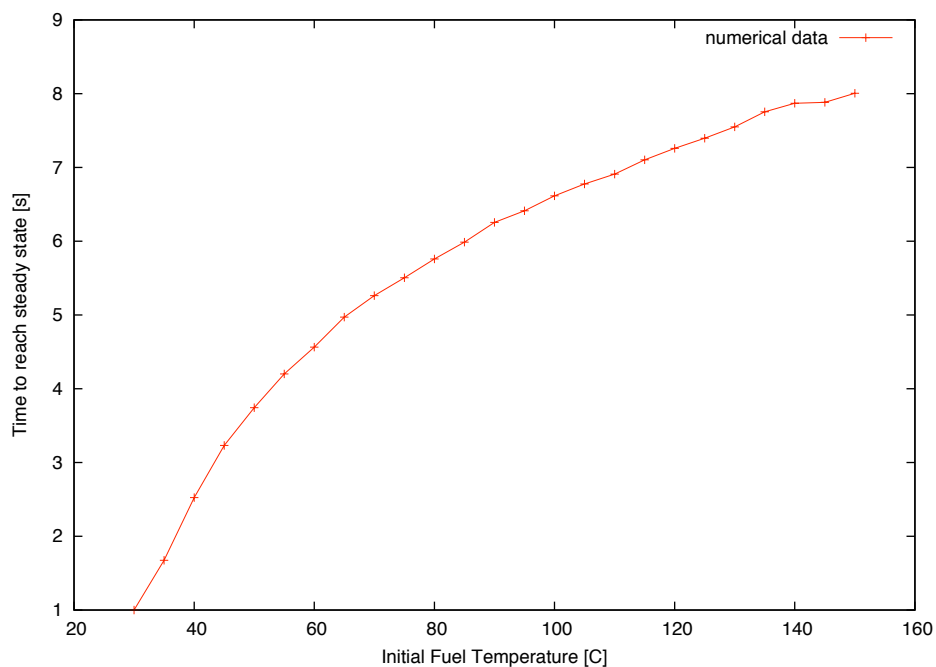


Figure 7.12: Times to reach a steady state versus initial fuel temperature as described above.

7.6.1 Variation of thermal feedback coefficients Θ_F and Θ_C

According to section 7.6 the factor Θ_F is assumed to be of a quadratic form. The factors obtained by experiment were fitted to a second order polynomial

$$\Theta_F(x) = a + bx + cx^2 \quad (7.7)$$

in the range [30:100] resulting in the following parameters when fitted:

Final set of parameters	Asymptotic Standard Error		
=====	=====		
a	= -25.6424	+/- 1.138	(4.439%)
b	= 1.01475	+/- 0.03808	(3.752%)
c	= -0.00500635	+/- 0.0002894	(5.781%)

This function has been used to determine the factor Θ_F in all calculations below.

7.6.2 Correction factors

The factor $\alpha_C F$ mentioned above has been calculated for experimental data and fitted to a quadratic for $f(x) = a + b(x - c)^2$. The results of the fit are shown below. This function has been used as correction factor in all calculations below.

Final set of parameters	Asymptotic Standard Error		
=====	=====		
a	= 1.04281	+/- 0.07739	(7.421%)
b	= 0.00137711	+/- 0.0001115	(8.099%)
c	= -58.9072	+/- 0.9739	(1.653%)

7.7 Various Perturbations

The algorithm has been applied to various problems defined by their fuel temperature and the external reactivities (perturbations). The interesting temperature range is between 30 C (normal shutdown conditions) and 150 C (temperature at a nominal reactor power of 250 kW). Various theoretical external reactivities were applied to states with fuel temperatures within the range mentioned above. The results are presented in both numerical and graphical form below.

7.7.1 Fuel temperature: 30 ° C, positive reactivities

Applied reactivities and resulting power deviations

Table 7.3: Effects of positive external reactivities at $T_F = 30^\circ\text{C}$

ρ_e	Power deviation [times]	ρ_e	Power deviation [times]
0.010	0.324	0.100	3.803
0.020	0.653	0.200	6.237
0.030	0.995	0.300	10.082
0.040	1.352	0.400	13.715
0.050	1.727	0.500	17.462
0.060	2.121	0.600	21.147
0.070	2.534	0.700	23.798
0.080	2.967	0.800	25.995
0.090	3.397	0.900	28.509

Graphical representation of the results

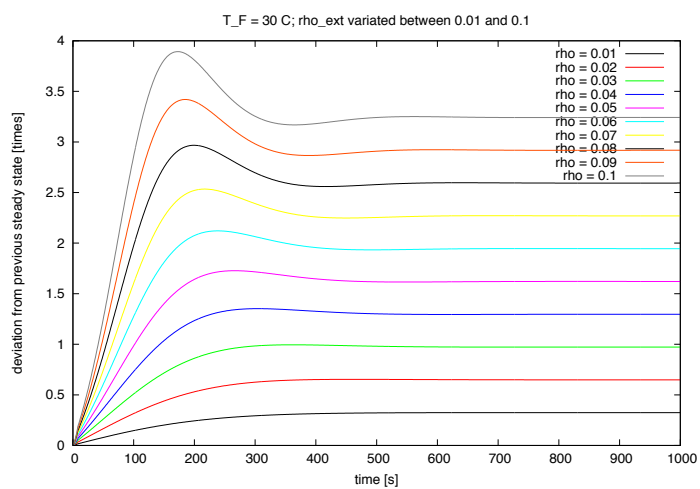


Figure 7.13: Applied positive reactivities and resulting power deviations

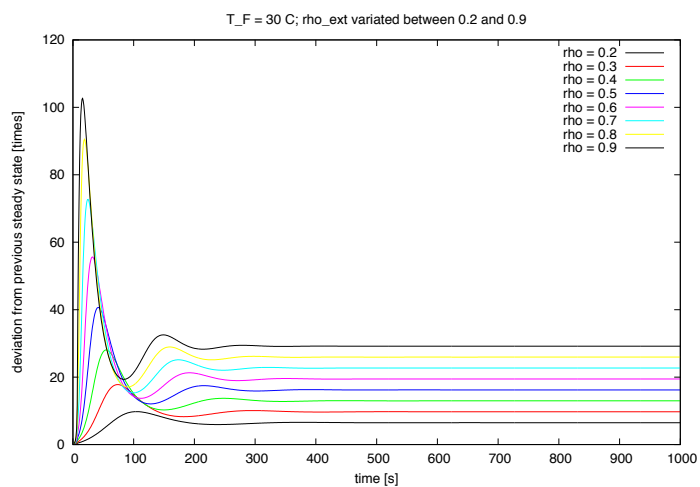


Figure 7.14: Applied positive reactivities and resulting power deviations

7.7.2 Fuel temperature: 30 ° C, negative reactivities

Applied reactivities and resulting power deviations

Table 7.4: Effects of negative external reactivities at $T_F = 30^\circ\text{C}$

ρ_e	Power deviation [times]	ρ_e	Power deviation [times]
-0.010	-0.203	-0.100	-0.910
-0.020	-0.369	-0.200	-0.991
-0.030	-0.503	-0.300	-0.999
-0.040	-0.610	-0.400	-1.000
-0.050	-0.694	-0.500	-1.000
-0.060	-0.761	-0.600	-1.000
-0.070	-0.813	-0.700	-1.000
-0.080	-0.854	-0.800	-1.000
-0.090	-0.886	-0.900	-1.000

Graphical representation of the results

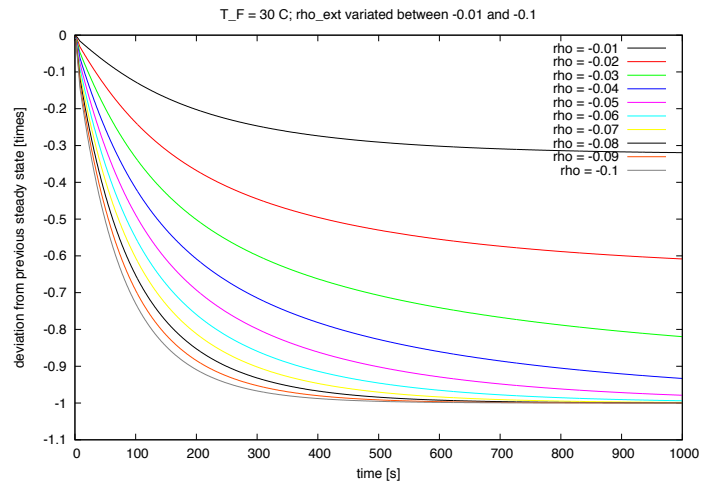


Figure 7.15: Applied negative reactivities and resulting power deviations

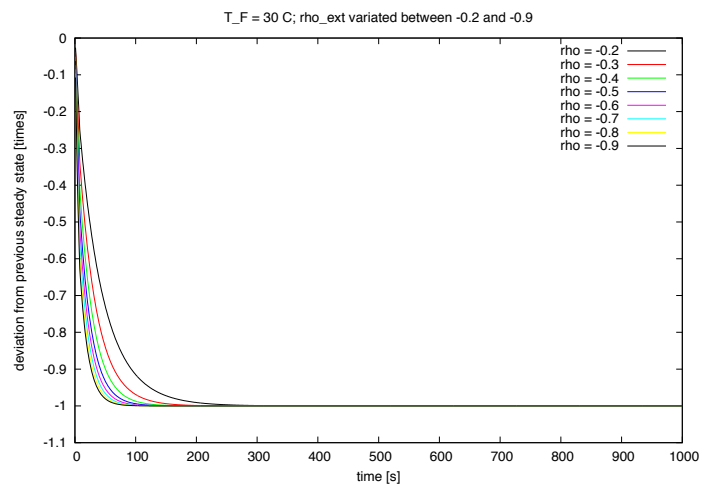


Figure 7.16: Applied negative reactivities and resulting power deviations

7.7.3 Fuel temperature: 40 ° C, positive reactivities

Applied reactivities and resulting power deviations

Table 7.5: Effects of positive external reactivities at $T_F = 40^\circ\text{C}$

ρ_e	Power deviation [times]	ρ_e	Power deviation [times]
0.010	0.131	0.100	1.156
0.020	0.264	0.200	2.359
0.030	0.397	0.300	3.630
0.040	0.525	0.400	4.957
0.050	0.648	0.500	6.328
0.060	0.765	0.600	7.600
0.070	0.874	0.700	8.449
0.080	0.975	0.800	9.132
0.090	1.069	0.900	9.921

Graphical representation of the results

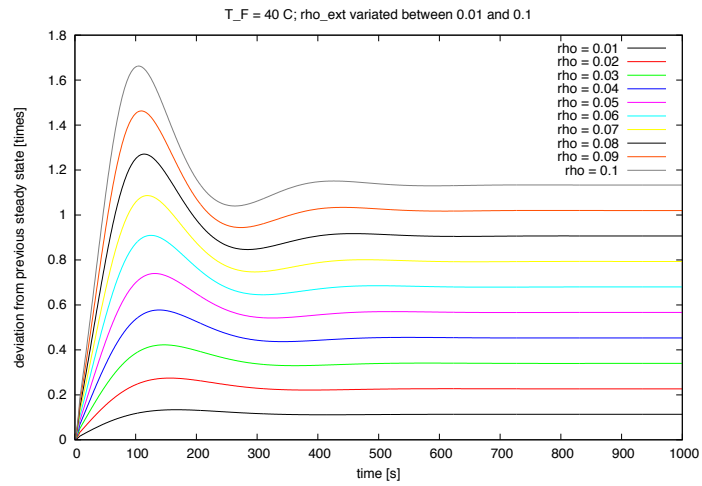


Figure 7.17: Applied positive reactivities and resulting power deviations

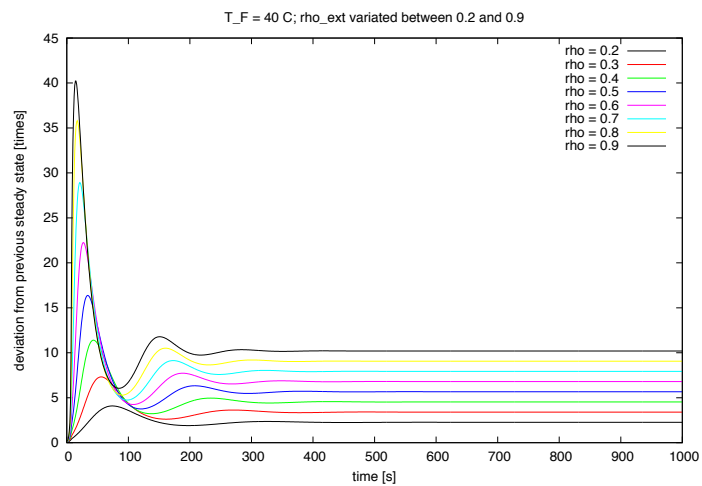


Figure 7.18: Applied positive reactivities and resulting power deviations

7.7.4 Fuel temperature: 40 ° C, negative reactivities

Applied reactivities and resulting power deviations

Table 7.6: Effects of negative external reactivities at $T_F = 40^\circ\text{C}$

ρ_e	Power deviation [times]	ρ_e	Power deviation [times]
-0.010	-0.113	-0.100	-0.835
-0.020	-0.247	-0.200	-0.982
-0.030	-0.358	-0.300	-0.998
-0.040	-0.459	-0.400	-1.000
-0.050	-0.548	-0.500	-1.000
-0.060	-0.626	-0.600	-1.000
-0.070	-0.693	-0.700	-1.000
-0.080	-0.749	-0.800	-1.000
-0.090	-0.796	-0.900	-1.000

Graphical representation of the results

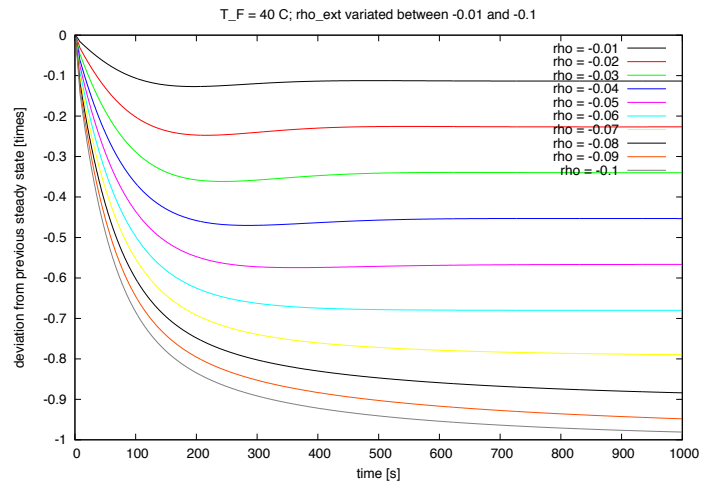


Figure 7.19: Applied negative reactivities and resulting power deviations

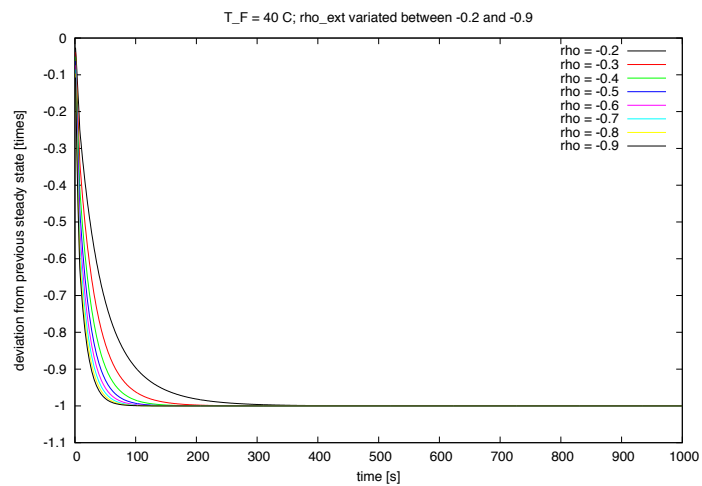


Figure 7.20: Applied negative reactivities and resulting power deviations

7.7.5 Fuel temperature: 50 ° C, positive reactivities

Applied reactivities and resulting power deviations

Table 7.7: Effects of positive external reactivities at $T_F = 50^\circ\text{C}$

ρ_e	Power deviation [times]	ρ_e	Power deviation [times]
0.010	0.071	0.100	0.556
0.020	0.139	0.200	1.400
0.030	0.203	0.300	2.162
0.040	0.262	0.400	2.957
0.050	0.318	0.500	3.778
0.060	0.370	0.600	4.470
0.070	0.420	0.700	4.908
0.080	0.467	0.800	5.259
0.090	0.512	0.900	5.674

Graphical representation of the results

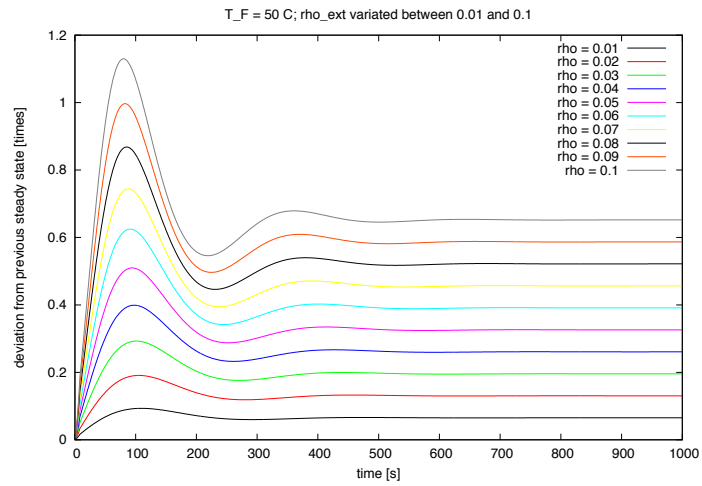


Figure 7.21: Applied positive reactivities and resulting power deviations

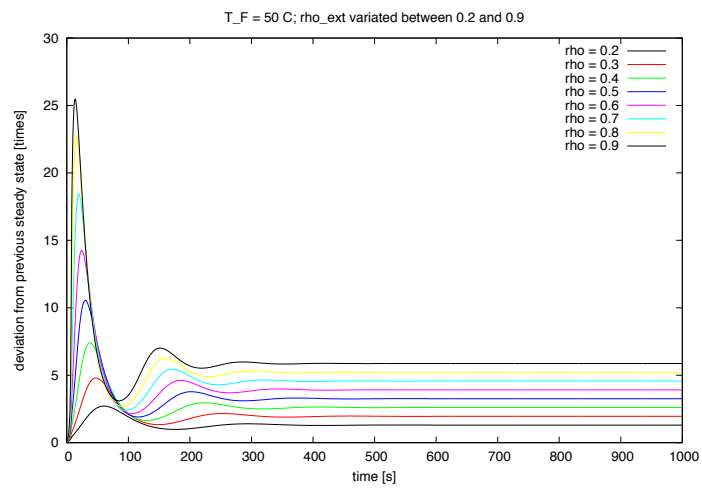


Figure 7.22: Applied positive reactivities and resulting power deviations

7.7.6 Fuel temperature: 50 ° C, negative reactivities

Applied reactivities and resulting power deviations

Table 7.8: Effects of negative external reactivities at $T_F = 50^\circ\text{C}$

ρ_e	Power deviation [times]	ρ_e	Power deviation [times]
-0.010	-0.061	-0.100	-0.709
-0.020	-0.123	-0.200	-0.960
-0.030	-0.187	-0.300	-0.995
-0.040	-0.251	-0.400	-0.999
-0.050	-0.316	-0.500	-1.000
-0.060	-0.382	-0.600	-1.000
-0.070	-0.449	-0.700	-1.000
-0.080	-0.516	-0.800	-1.000
-0.090	-0.583	-0.900	-1.000

Graphical representation of the results

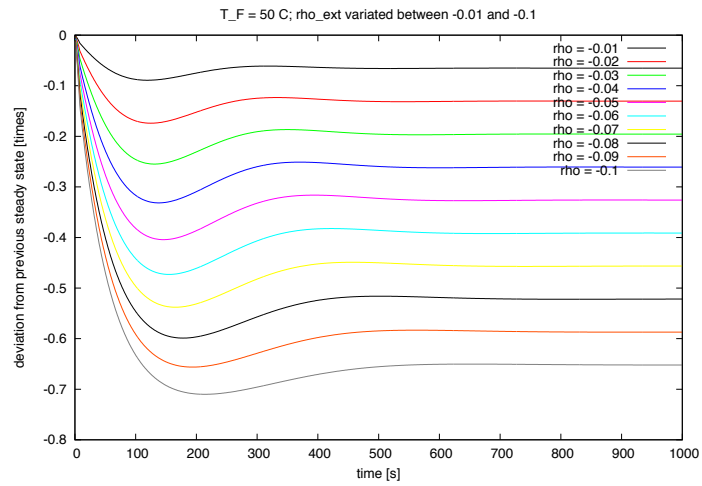


Figure 7.23: Applied negative reactivities and resulting power deviations

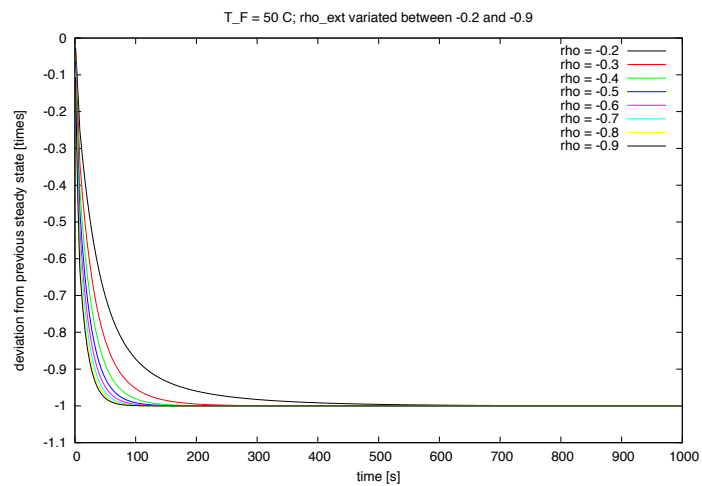


Figure 7.24: Applied negative reactivities and resulting power deviations

7.7.7 Fuel temperature: 60 ° C, positive reactivities

Applied reactivities and resulting power deviations

Table 7.9: Effects of positive external reactivities at $T_F = 60^\circ\text{C}$

ρ_e	Power deviation [times]	ρ_e	Power deviation [times]
0.010	0.039	0.100	0.475
0.020	0.076	0.200	0.982
0.030	0.111	0.300	1.517
0.040	0.145	0.400	2.075
0.050	0.177	0.500	2.641
0.060	0.208	0.600	3.052
0.070	0.239	0.700	3.311
0.080	0.377	0.800	3.530
0.090	0.426	0.900	3.800

Graphical representation of the results

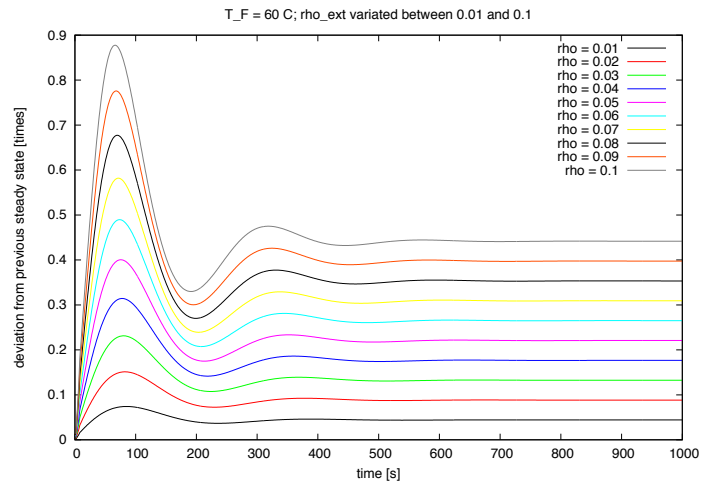


Figure 7.25: Applied positive reactivities and resulting power deviations

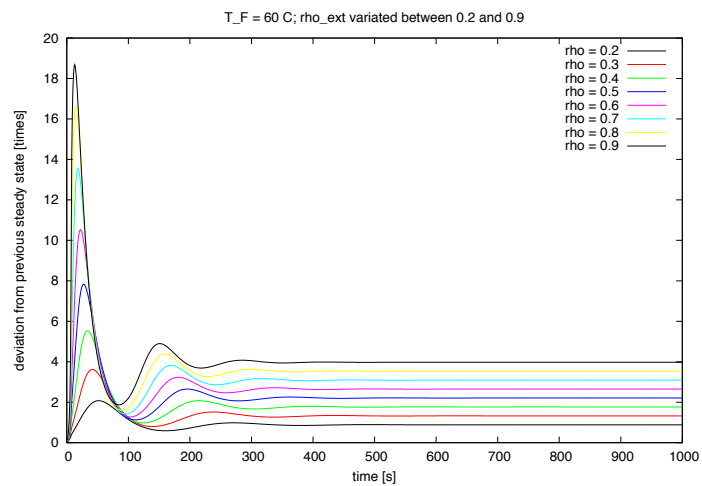


Figure 7.26: Applied positive reactivities and resulting power deviations

7.7.8 Fuel temperature: 60 ° C, negative reactivities

Applied reactivities and resulting power deviations

Table 7.10: Effects of negative external reactivities at $T_F = 60^\circ\text{C}$

ρ_e	Power deviation [times]	ρ_e	Power deviation [times]
-0.010	-0.038	-0.100	-0.416
-0.020	-0.076	-0.200	-0.909
-0.030	-0.115	-0.300	-0.988
-0.040	-0.156	-0.400	-0.998
-0.050	-0.197	-0.500	-1.000
-0.060	-0.239	-0.600	-1.000
-0.070	-0.282	-0.700	-1.000
-0.080	-0.326	-0.800	-1.000
-0.090	-0.371	-0.900	-1.000

Graphical representation of the results

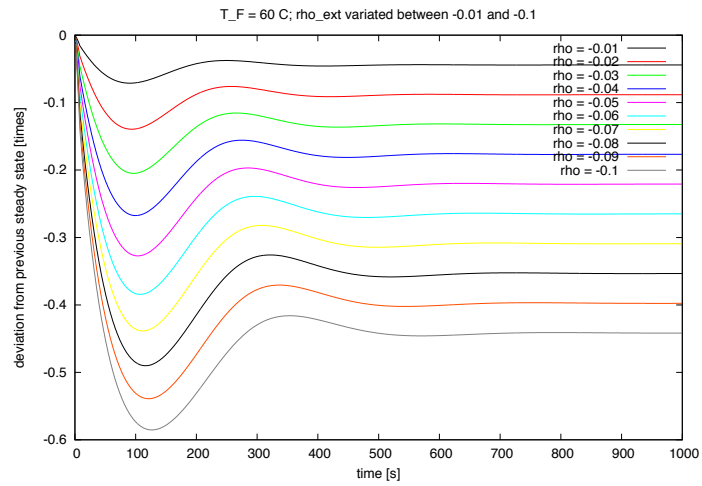


Figure 7.27: Applied negative reactivities and resulting power deviations

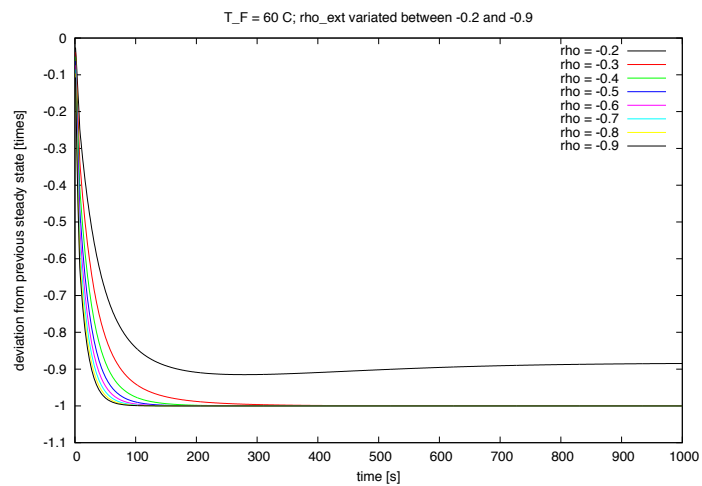


Figure 7.28: Applied negative reactivities and resulting power deviations

7.7.9 Fuel temperature: 70 ° C, positive reactivities

Applied reactivities and resulting power deviations

Table 7.11: Effects of positive external reactivities at $T_F = 70^\circ\text{C}$

ρ_e	Power deviation [times]	ρ_e	Power deviation [times]
0.010	0.024	0.100	0.362
0.020	0.070	0.200	0.749
0.030	0.106	0.300	1.155
0.040	0.142	0.400	1.578
0.050	0.178	0.500	1.967
0.060	0.214	0.600	2.218
0.070	0.251	0.700	2.387
0.080	0.288	0.800	2.544
0.090	0.325	0.900	2.748

Graphical representation of the results

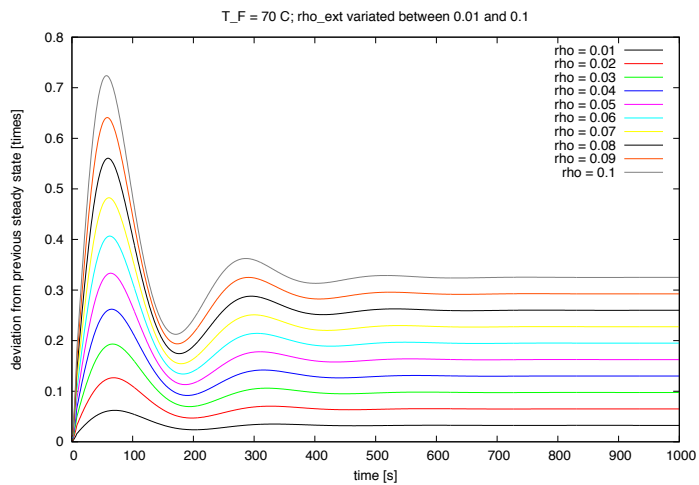


Figure 7.29: Applied positive reactivities and resulting power deviations

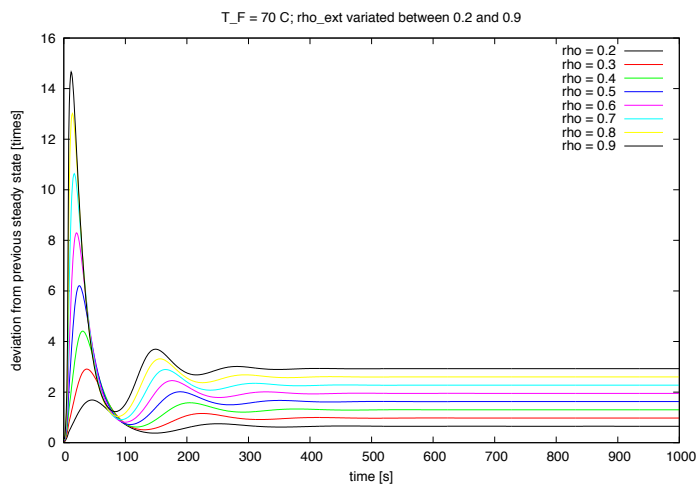


Figure 7.30: Applied positive reactivities and resulting power deviations

7.7.10 Fuel temperature: 70 ° C, negative reactivities

Applied reactivities and resulting power deviations

Table 7.12: Effects of negative external reactivities at $T_F = 70^\circ\text{C}$

ρ_e	Power deviation [times]	ρ_e	Power deviation [times]
-0.010	-0.024	-0.100	-0.275
-0.020	-0.050	-0.200	-0.621
-0.030	-0.075	-0.300	-0.968
-0.040	-0.102	-0.400	-0.996
-0.050	-0.129	-0.500	-0.999
-0.060	-0.157	-0.600	-1.000
-0.070	-0.185	-0.700	-1.000
-0.080	-0.214	-0.800	-1.000
-0.090	-0.244	-0.900	-1.000

Graphical representation of the results

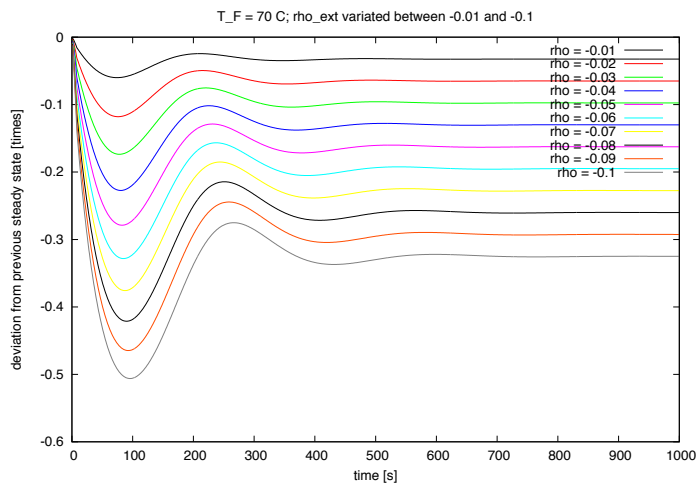


Figure 7.31: Applied negative reactivities and resulting power deviations

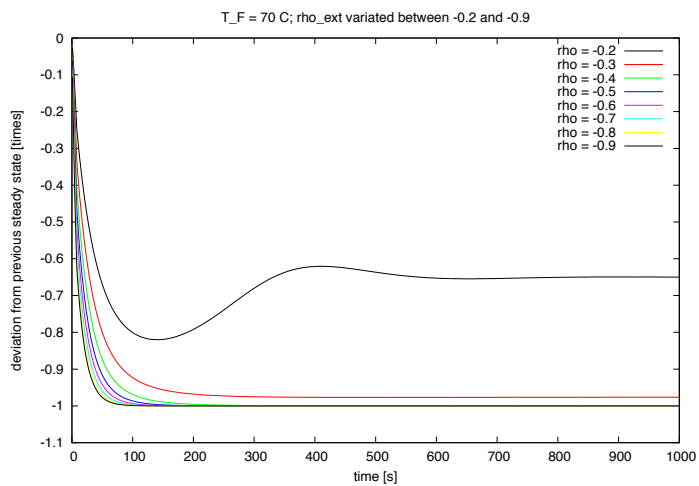


Figure 7.32: Applied negative reactivities and resulting power deviations

7.7.11 Fuel temperature: 80 ° C, positive reactivities

Applied reactivities and resulting power deviations

Table 7.13: Effects of positive external reactivities at $T_F = 80^\circ\text{C}$

ρ_e	Power deviation [times]	ρ_e	Power deviation [times]
0.010	0.028	0.100	0.291
0.020	0.057	0.200	0.599
0.030	0.085	0.300	0.923
0.040	0.114	0.400	1.250
0.050	0.143	0.500	1.497
0.060	0.172	0.600	1.658
0.070	0.201	0.700	1.780
0.080	0.231	0.800	1.911
0.090	0.261	0.900	2.084

Graphical representation of the results

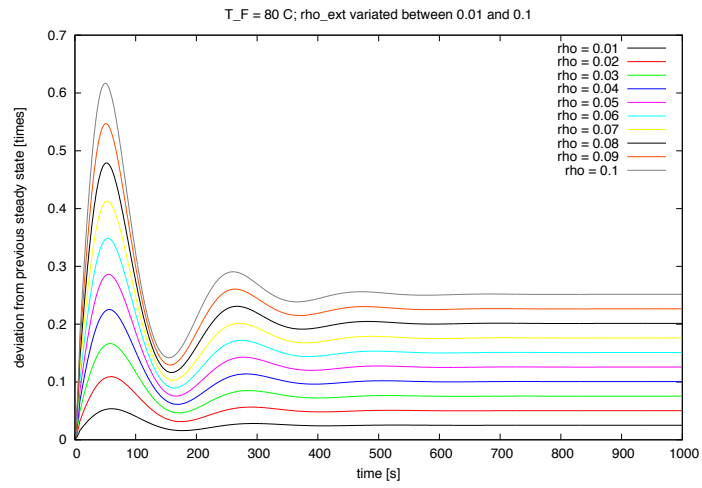


Figure 7.33: Applied positive reactivities and resulting power deviations

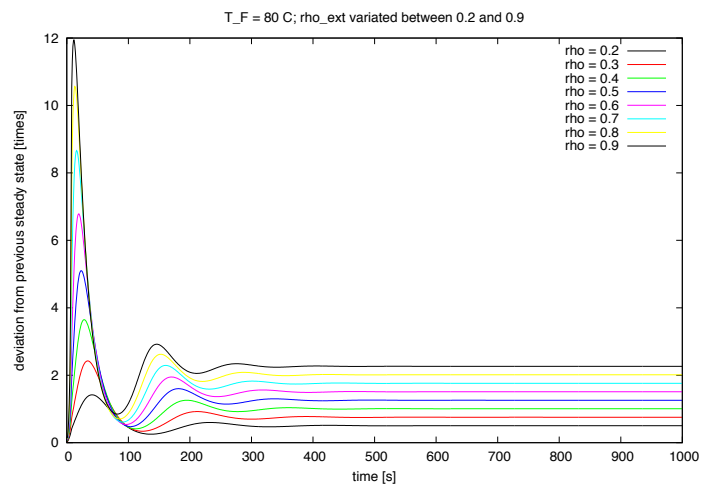


Figure 7.34: Applied positive reactivities and resulting power deviations

7.7.12 Fuel temperature: 80 ° C, negative reactivities

Applied reactivities and resulting power deviations

Table 7.14: Effects of negative external reactivities at $T_F = 80^\circ\text{C}$

ρ_e	Power deviation [times]	ρ_e	Power deviation [times]
-0.010	-0.017	-0.100	-0.186
-0.020	-0.034	-0.200	-0.428
-0.030	-0.052	-0.300	-0.727
-0.040	-0.069	-0.400	-0.987
-0.050	-0.087	-0.500	-0.998
-0.060	-0.105	-0.600	-1.000
-0.070	-0.125	-0.700	-1.000
-0.080	-0.145	-0.800	-1.000
-0.090	-0.165	-0.900	-1.000

Graphical representation of the results

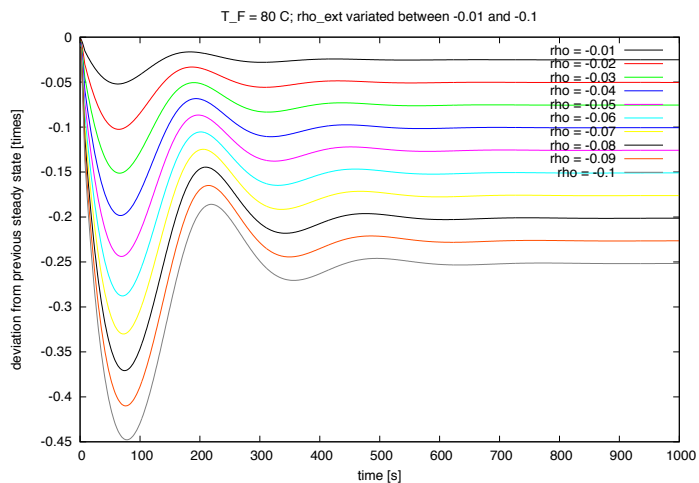


Figure 7.35: Applied negative reactivities and resulting power deviations

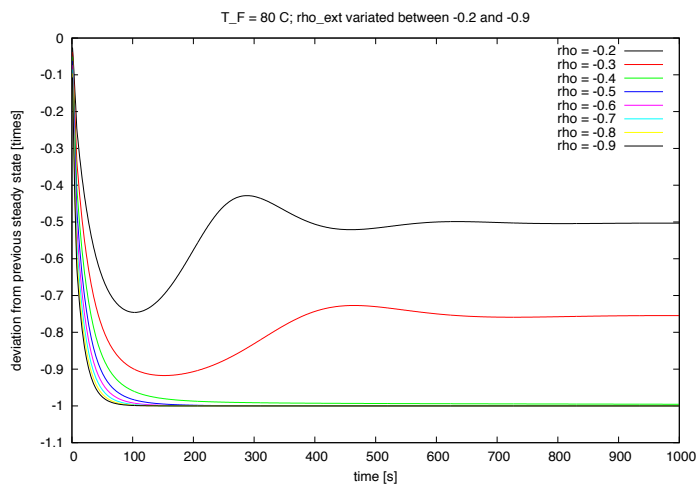


Figure 7.36: Applied negative reactivities and resulting power deviations

7.7.13 Fuel temperature: 90 ° C, positive reactivities

Applied reactivities and resulting power deviations

Table 7.15: Effects of positive external reactivities at $T_F = 90^\circ\text{C}$

ρ_e	Power deviation [times]	ρ_e	Power deviation [times]
0.010	0.023	0.100	0.240
0.020	0.047	0.200	0.494
0.030	0.071	0.300	0.758
0.040	0.094	0.400	0.986
0.050	0.118	0.500	1.143
0.060	0.143	0.600	1.256
0.070	0.167	0.700	1.359
0.080	0.191	0.800	1.482
0.090	0.216	0.900	1.641

Graphical representation of the results

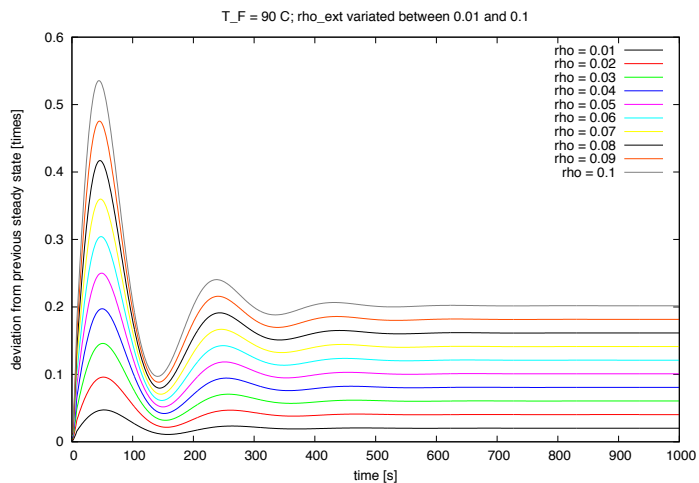


Figure 7.37: Applied positive reactivities and resulting power deviations

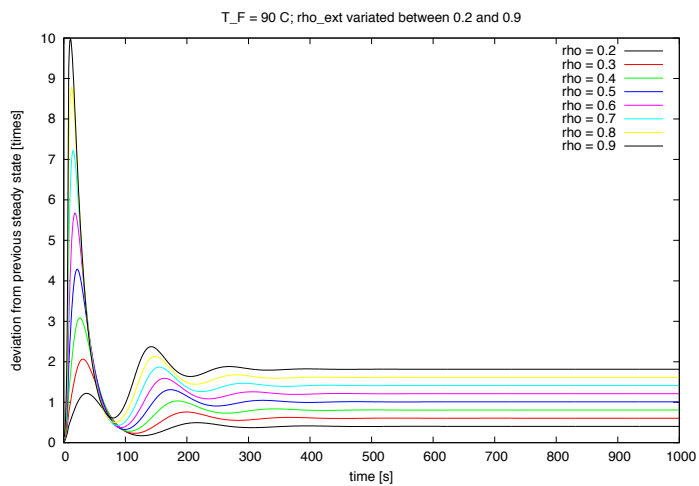


Figure 7.38: Applied positive reactivities and resulting power deviations

7.7.14 Fuel temperature: 90 ° C, negative reactivities

Applied reactivities and resulting power deviations

Table 7.16: Effects of negative external reactivities at $T_F = 90^\circ\text{C}$

ρ_e	Power deviation [times]	ρ_e	Power deviation [times]
-0.010	-0.016	-0.100	-0.133
-0.020	-0.031	-0.200	-0.296
-0.030	-0.045	-0.300	-0.516
-0.040	-0.058	-0.400	-0.779
-0.050	-0.071	-0.500	-0.994
-0.060	-0.084	-0.600	-0.999
-0.070	-0.096	-0.700	-1.000
-0.080	-0.108	-0.800	-1.000
-0.090	-0.120	-0.900	-1.000

Graphical representation of the results

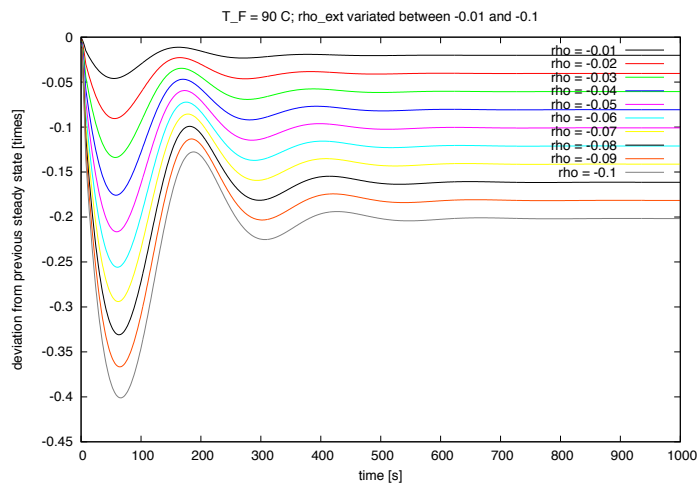


Figure 7.39: Applied negative reactivities and resulting power deviations

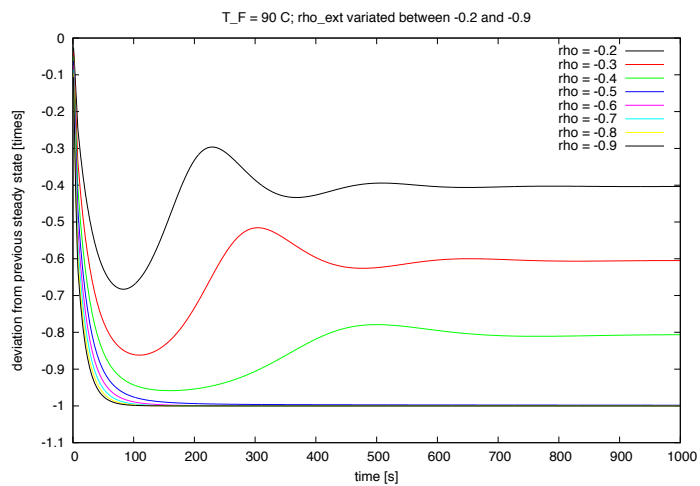


Figure 7.40: Applied negative reactivities and resulting power deviations

7.7.15 Fuel temperature: 100 ° C, positive reactivities

Applied reactivities and resulting power deviations

Table 7.17: Effects of positive external reactivities at $T_F = 100^\circ\text{C}$

ρ_e	Power deviation [times]	ρ_e	Power deviation [times]
0.010	0.020	0.100	0.203
0.020	0.040	0.200	0.415
0.030	0.060	0.300	0.613
0.040	0.080	0.400	0.762
0.050	0.100	0.500	0.872
0.060	0.120	0.600	0.965
0.070	0.141	0.700	1.066
0.080	0.161	0.800	1.189
0.090	0.182	0.900	1.548

Graphical representation of the results

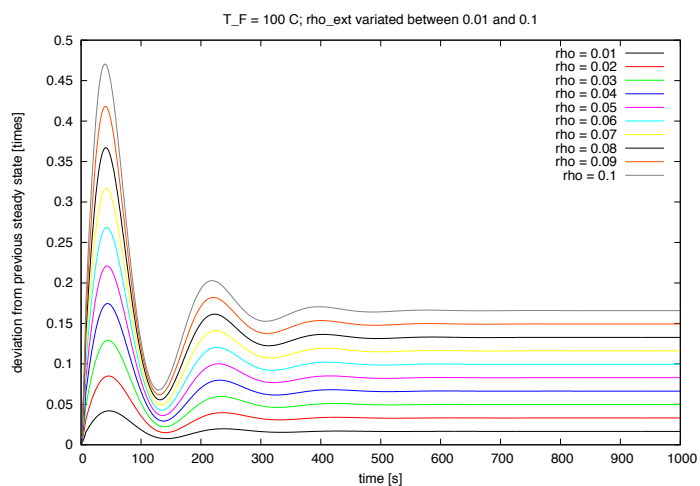


Figure 7.41: Applied positive reactivities and resulting power deviations

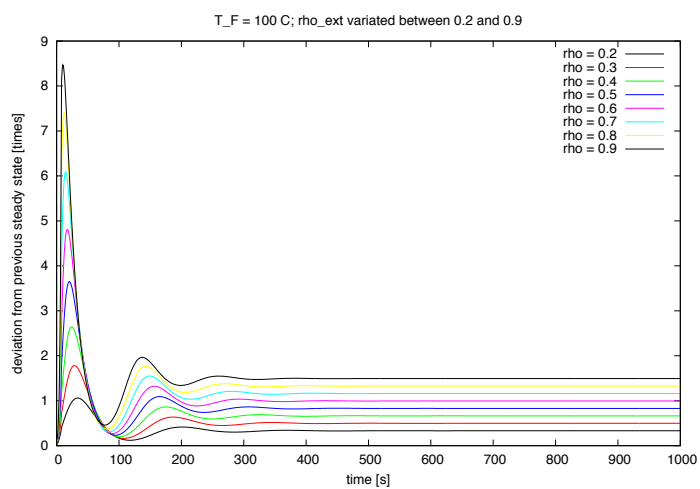


Figure 7.42: Applied positive reactivities and resulting power deviations

7.7.16 Fuel temperature: 100 ° C, negative reactivities

Applied reactivities and resulting power deviations

Table 7.18: Effects of negative external reactivities at $T_F = 100^\circ\text{C}$

ρ_e	Power deviation [times]	ρ_e	Power deviation [times]
-0.010	-0.016	-0.100	-0.127
-0.020	-0.031	-0.200	-0.211
-0.030	-0.046	-0.300	-0.362
-0.040	-0.060	-0.400	-0.562
-0.050	-0.073	-0.500	-0.797
-0.060	-0.085	-0.600	-0.996
-0.070	-0.097	-0.700	-0.999
-0.080	-0.107	-0.800	-1.000
-0.090	-0.118	-0.900	-1.000

Graphical representation of the results

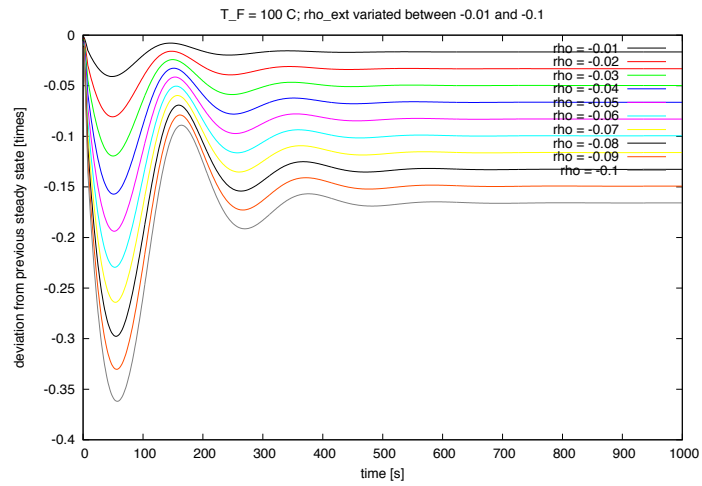


Figure 7.43: Applied negative reactivities and resulting power deviations

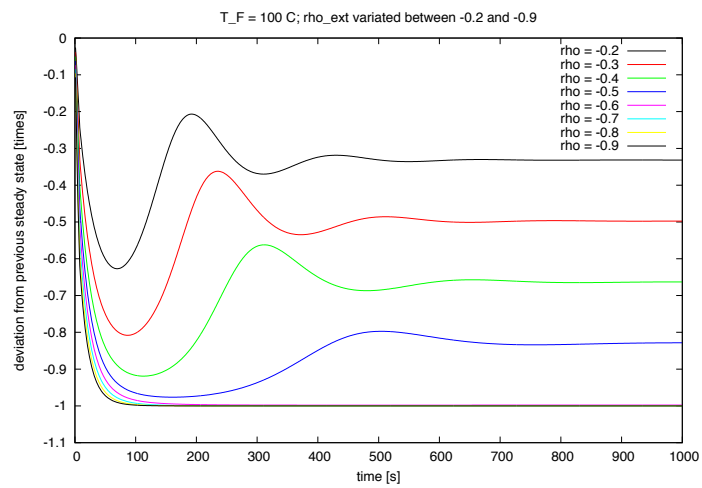


Figure 7.44: Applied negative reactivities and resulting power deviations

7.7.17 Fuel temperature: 110 ° C, positive reactivities**Applied reactivities and resulting power deviations**Table 7.19: Effects of positive external reactivities at $T_F = 110^\circ\text{C}$

ρ_e	Power deviation [times]	ρ_e	Power deviation [times]
0.010	0.017	0.100	0.173
0.020	0.034	0.200	0.341
0.030	0.051	0.300	0.478
0.040	0.068	0.400	0.583
0.050	0.086	0.500	0.672
0.060	0.103	0.600	0.763
0.070	0.120	0.700	0.869
0.080	0.138	0.800	1.155
0.090	0.156	0.900	1.296

Graphical representation of the results

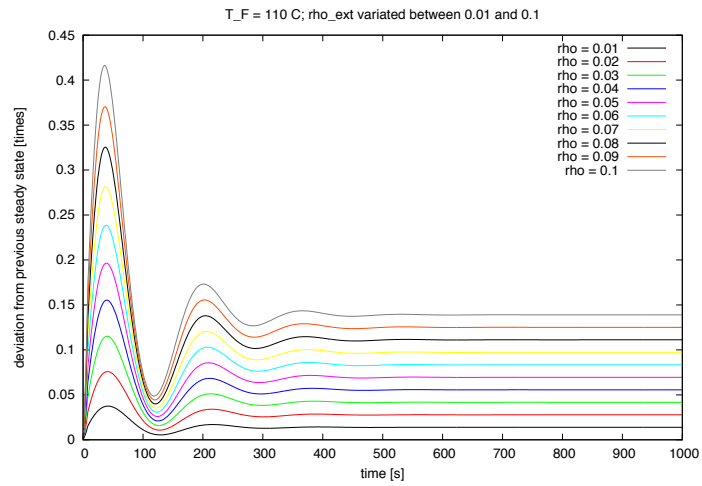


Figure 7.45: Applied positive reactivities and resulting power deviations

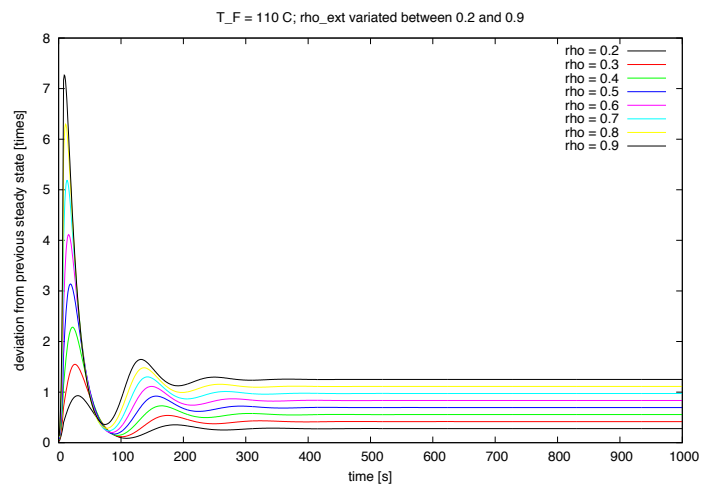


Figure 7.46: Applied positive reactivities and resulting power deviations

7.7.18 Fuel temperature: 110 ° C, negative reactivities

Applied reactivities and resulting power deviations

Table 7.20: Effects of negative external reactivities at $T_F = 110^\circ\text{C}$

ρ_e	Power deviation [times]	ρ_e	Power deviation [times]
-0.010	-0.016	-0.100	-0.137
-0.020	-0.032	-0.200	-0.213
-0.030	-0.047	-0.300	-0.261
-0.040	-0.061	-0.400	-0.400
-0.050	-0.076	-0.500	-0.581
-0.060	-0.089	-0.600	-0.793
-0.070	-0.102	-0.700	-0.997
-0.080	-0.115	-0.800	-1.000
-0.090	-0.126	-0.900	-1.000

Graphical representation of the results

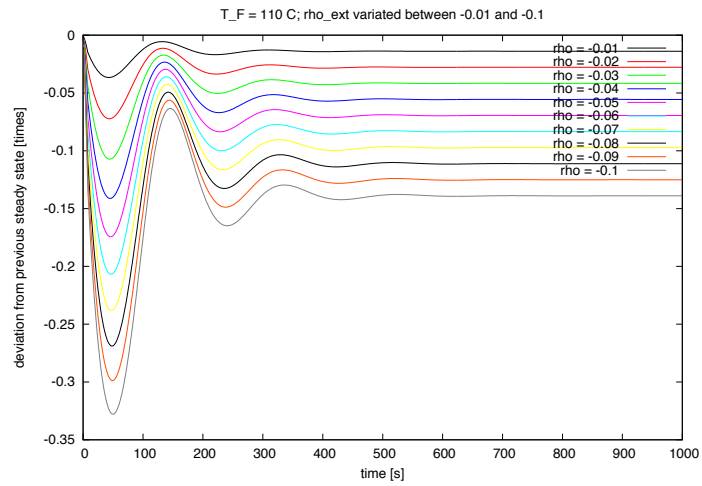


Figure 7.47: Applied negative reactivities and resulting power deviations

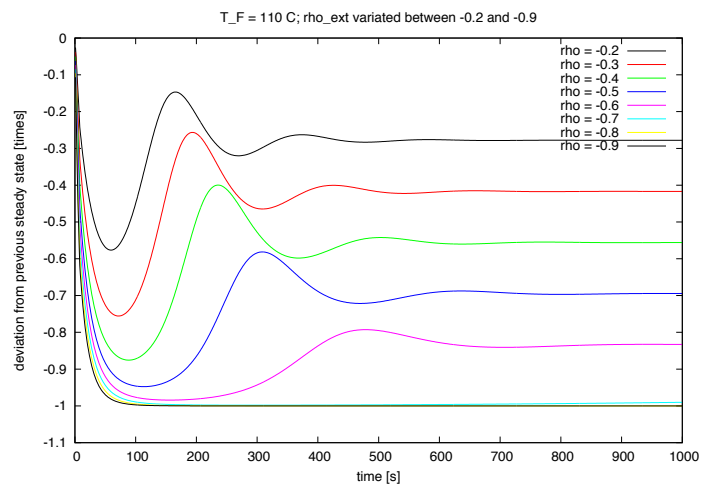


Figure 7.48: Applied negative reactivities and resulting power deviations

7.7.19 Fuel temperature: 120 ° C, positive reactivities

Applied reactivities and resulting power deviations

Table 7.21: Effects of positive external reactivities at $T_F = 120^\circ\text{C}$

ρ_e	Power deviation [times]	ρ_e	Power deviation [times]
0.010	0.015	0.100	0.143
0.020	0.029	0.200	0.265
0.030	0.044	0.300	0.365
0.040	0.058	0.400	0.452
0.050	0.073	0.500	0.538
0.060	0.087	0.600	0.634
0.070	0.101	0.700	0.859
0.080	0.115	0.800	0.980
0.090	0.129	0.900	1.100

Graphical representation of the results

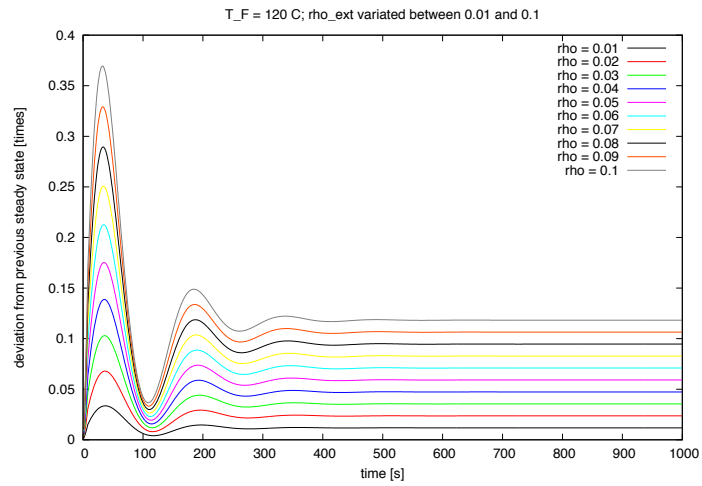


Figure 7.49: Applied positive reactivities and resulting power deviations

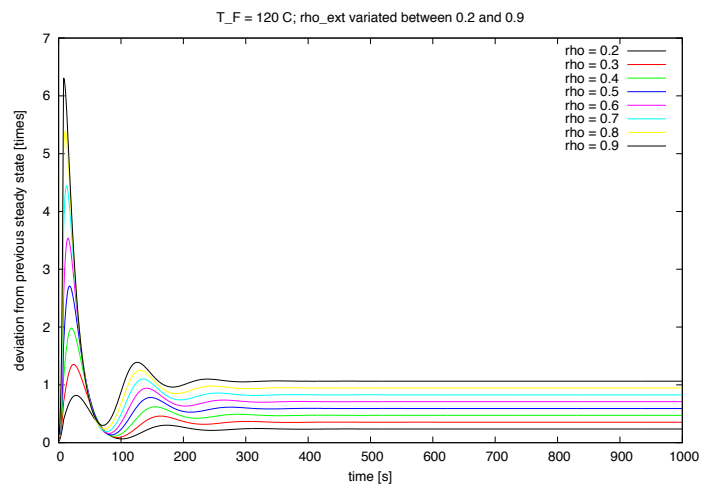


Figure 7.50: Applied positive reactivities and resulting power deviations

7.7.20 Fuel temperature: 120 ° C, negative reactivities

Applied reactivities and resulting power deviations

Table 7.22: Effects of negative external reactivities at $T_F = 120^\circ\text{C}$

ρ_e	Power deviation [times]	ρ_e	Power deviation [times]
-0.010	-0.015	-0.100	-0.139
-0.020	-0.029	-0.200	-0.240
-0.030	-0.044	-0.300	-0.283
-0.040	-0.058	-0.400	-0.298
-0.050	-0.072	-0.500	-0.419
-0.060	-0.086	-0.600	-0.582
-0.070	-0.100	-0.700	-0.772
-0.080	-0.113	-0.800	-0.998
-0.090	-0.126	-0.900	-1.000

Graphical representation of the results

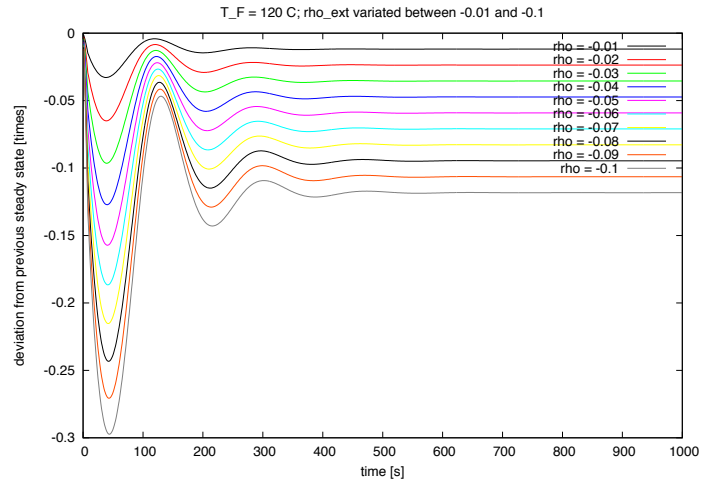


Figure 7.51: Applied negative reactivities and resulting power deviations

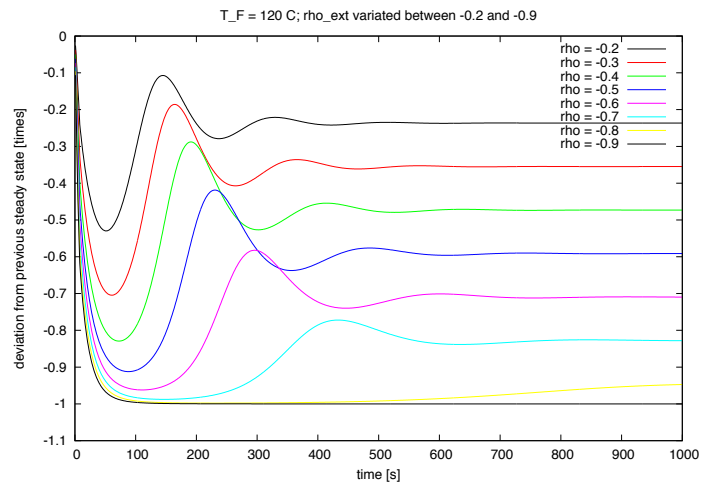


Figure 7.52: Applied negative reactivities and resulting power deviations

7.7.21 Fuel temperature: 130 ° C, positive reactivities

Applied reactivities and resulting power deviations

Table 7.23: Effects of positive external reactivities at $T_F = 130^\circ\text{C}$

ρ_e	Power deviation [times]	ρ_e	Power deviation [times]
0.010	0.012	0.100	0.110
0.020	0.023	0.200	0.203
0.030	0.035	0.300	0.287
0.040	0.046	0.400	0.369
0.050	0.057	0.500	0.527
0.060	0.068	0.600	0.633
0.070	0.079	0.700	0.737
0.080	0.090	0.800	0.841
0.090	0.100	0.900	0.944

Graphical representation of the results

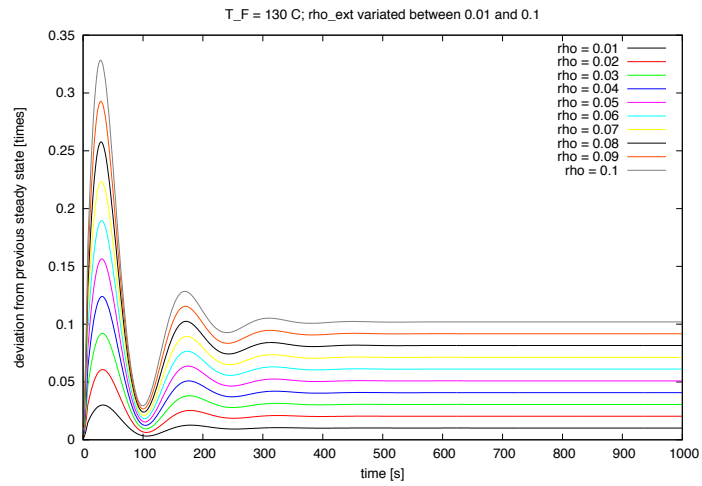


Figure 7.53: Applied positive reactivities and resulting power deviations

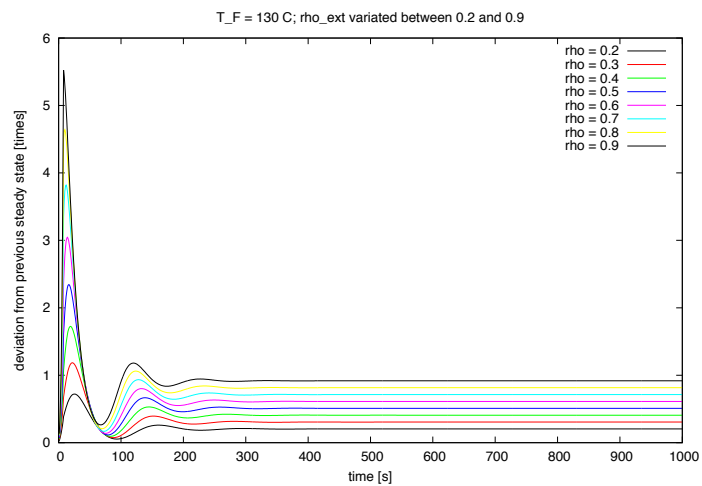


Figure 7.54: Applied positive reactivities and resulting power deviations

7.7.22 Fuel temperature: 130 ° C, negative reactivities**Applied reactivities and resulting power deviations**Table 7.24: Effects of negative external reactivities at $T_F = 130^\circ\text{C}$

ρ_e	Power deviation [times]	ρ_e	Power deviation [times]
-0.010	-0.009	-0.100	-0.094
-0.020	-0.019	-0.200	-0.241
-0.030	-0.028	-0.300	-0.324
-0.040	-0.037	-0.400	-0.352
-0.050	-0.047	-0.500	-0.339
-0.060	-0.056	-0.600	-0.426
-0.070	-0.066	-0.700	-0.572
-0.080	-0.075	-0.800	-0.740
-0.090	-0.084	-0.900	-0.997

Graphical representation of the results

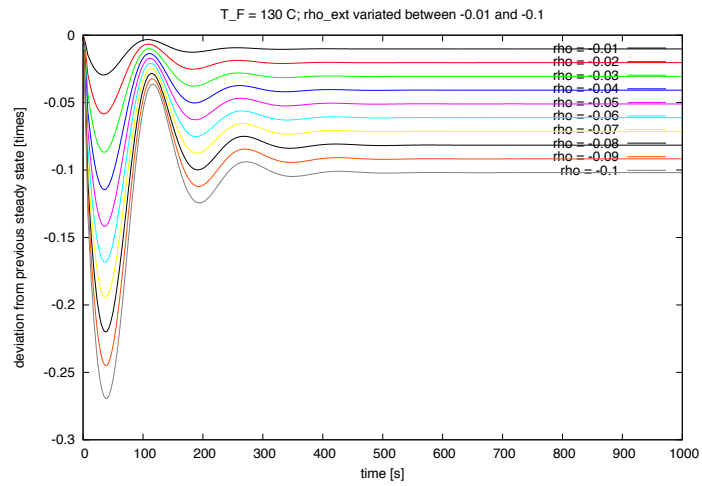


Figure 7.55: Applied negative reactivities and resulting power deviations

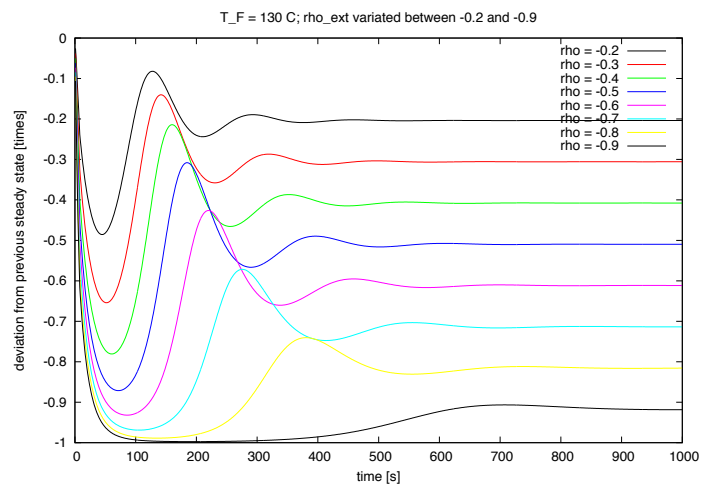


Figure 7.56: Applied negative reactivities and resulting power deviations

7.7.23 Fuel temperature: 140 ° C, positive reactivities

Applied reactivities and resulting power deviations

Table 7.25: Effects of positive external reactivities at $T_F = 140^\circ\text{C}$

ρ_e	Power deviation [times]	ρ_e	Power deviation [times]
0.010	0.009	0.100	0.085
0.020	0.018	0.200	0.164
0.030	0.027	0.300	0.243
0.040	0.035	0.400	0.366
0.050	0.044	0.500	0.457
0.060	0.052	0.600	0.548
0.070	0.061	0.700	0.639
0.080	0.069	0.800	0.729
0.090	0.077	0.900	0.818

Graphical representation of the results

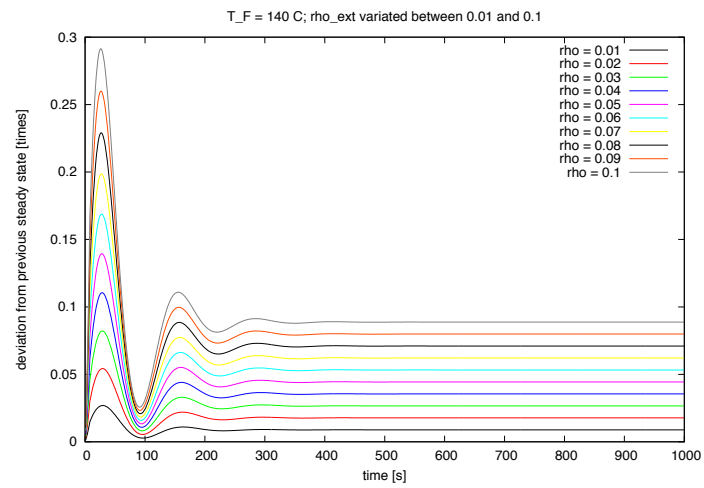


Figure 7.57: Applied positive reactivities and resulting power deviations

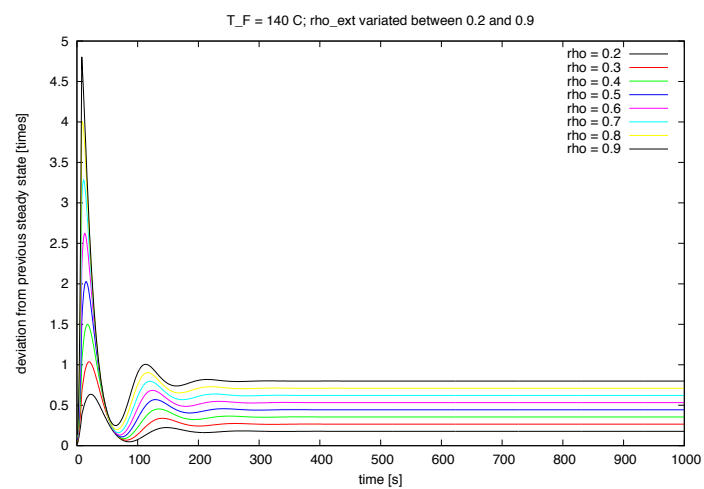


Figure 7.58: Applied positive reactivities and resulting power deviations

7.7.24 Fuel temperature: 140 ° C, negative reactivities

Applied reactivities and resulting power deviations

Table 7.26: Effects of negative external reactivities at $T_F = 140^\circ\text{C}$

ρ_e	Power deviation [times]	ρ_e	Power deviation [times]
-0.010	-0.008	-0.100	-0.082
-0.020	-0.016	-0.200	-0.165
-0.030	-0.025	-0.300	-0.314
-0.040	-0.033	-0.400	-0.394
-0.050	-0.041	-0.500	-0.425
-0.060	-0.049	-0.600	-0.403
-0.070	-0.057	-0.700	-0.428
-0.080	-0.066	-0.800	-0.555
-0.090	-0.074	-0.900	-0.703

Graphical representation of the results

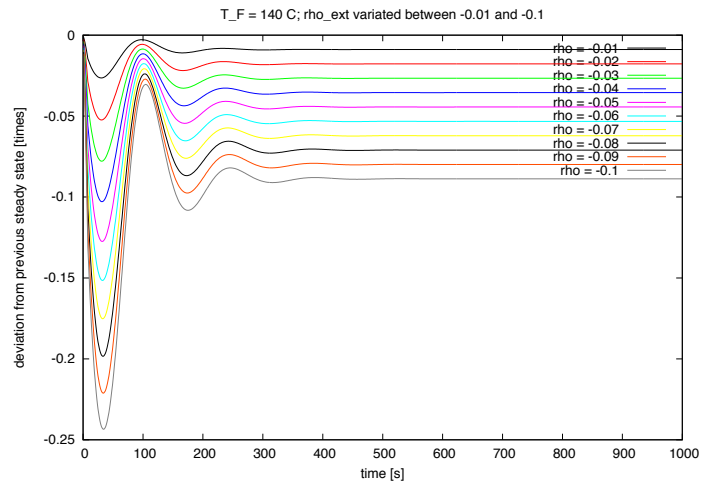


Figure 7.59: Applied negative reactivities and resulting power deviations

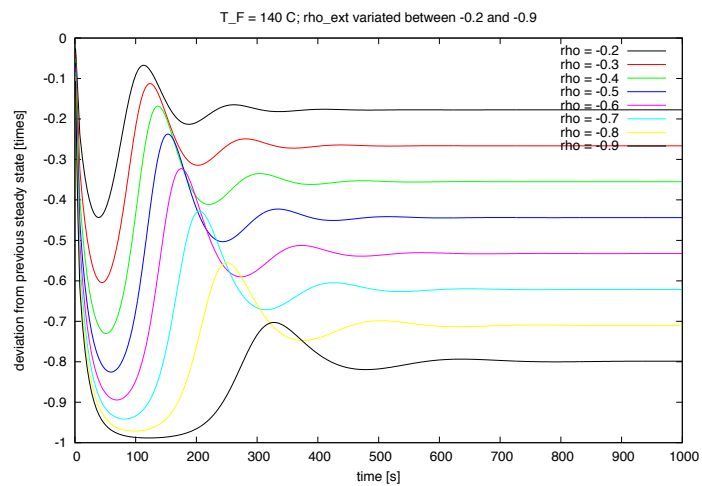


Figure 7.60: Applied negative reactivities and resulting power deviations

7.7.25 Fuel temperature: 150 ° C, positive reactivities**Applied reactivities and resulting power deviations**Table 7.27: Effects of positive external reactivities at $T_F = 150^\circ\text{C}$

ρ_e	Power deviation [times]	ρ_e	Power deviation [times]
0.010	0.007	0.100	0.072
0.020	0.015	0.200	0.160
0.030	0.022	0.300	0.239
0.040	0.029	0.400	0.319
0.050	0.036	0.500	0.399
0.060	0.044	0.600	0.478
0.070	0.051	0.700	0.557
0.080	0.058	0.800	0.636
0.090	0.065	0.900	0.715

Graphical representation of the results

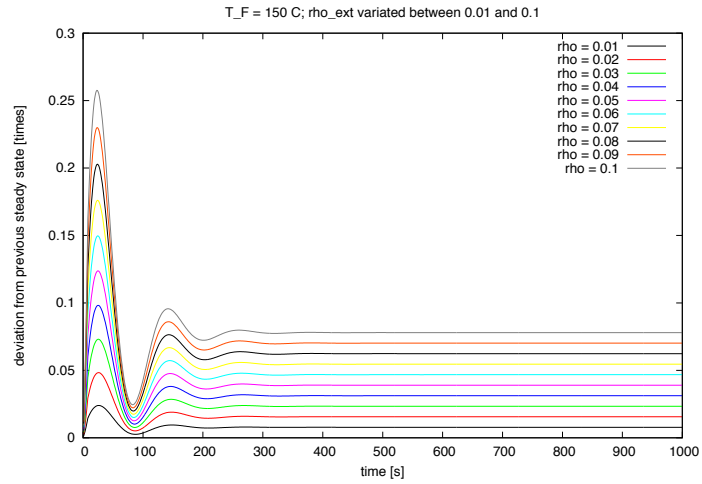


Figure 7.61: Applied positive reactivities and resulting power deviations

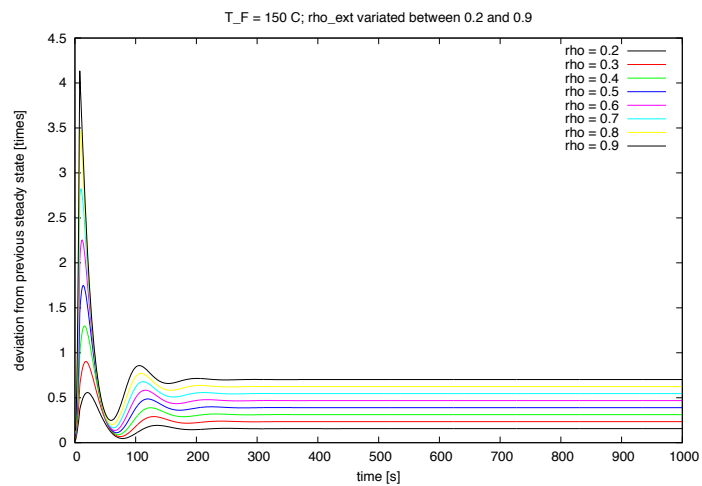


Figure 7.62: Applied positive reactivities and resulting power deviations

7.7.26 Fuel temperature: 150 ° C, negative reactivities

Applied reactivities and resulting power deviations

Table 7.28: Effects of negative external reactivities at $T_F = 150^\circ\text{C}$

ρ_e	Power deviation [times]	ρ_e	Power deviation [times]
-0.010	-0.007	-0.100	-0.073
-0.020	-0.015	-0.200	-0.146
-0.030	-0.022	-0.300	-0.220
-0.040	-0.029	-0.400	-0.295
-0.050	-0.036	-0.500	-0.443
-0.060	-0.044	-0.600	-0.492
-0.070	-0.051	-0.700	-0.488
-0.080	-0.058	-0.800	-0.455
-0.090	-0.065	-0.900	-0.539

Graphical representation of the results

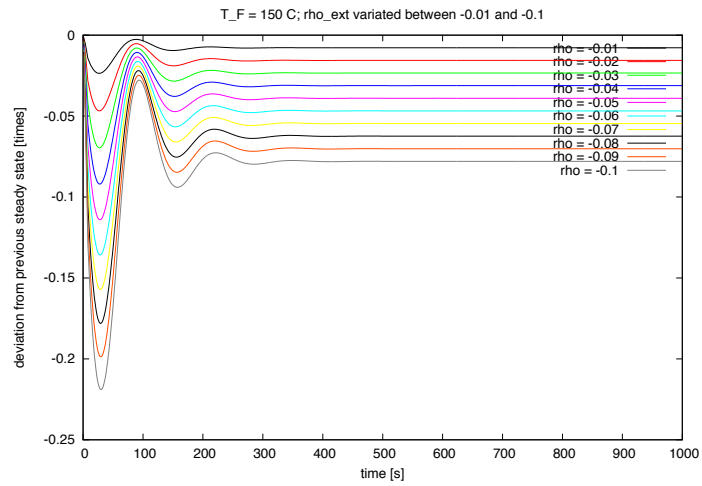


Figure 7.63: Applied negative reactivities and resulting power deviations

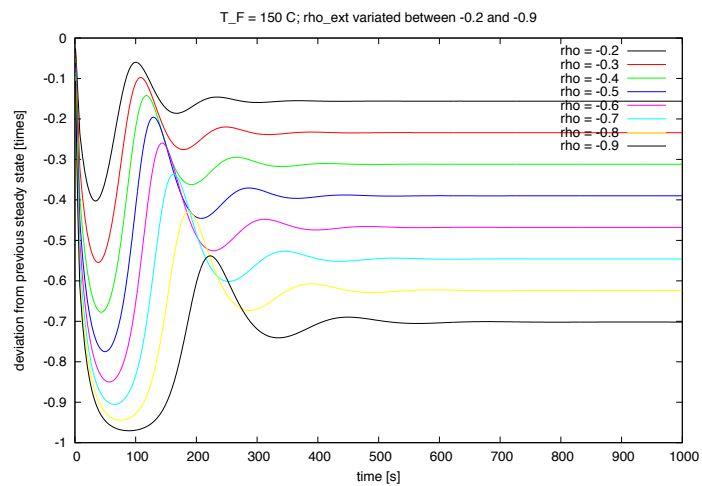


Figure 7.64: Applied negative reactivities and resulting power deviations

Discussion

Power deviation for perturbations between -0.01ρ and 0.9ρ for reactor core temperatures between $50\text{ }^{\circ}\text{C}$ and $150\text{ }^{\circ}\text{C}$ have been calculated numerically and presented both numerically and graphically. The results show clearly the increasing feedback mechanisms with increasing reactor temperature visible as oscillations in the graphical representations.

7.8 Fuel temperature

In the TRIGA reactor Vienna, two fuel rods equipped with three temperature couple sensors. Within these rods, the sensors are located at the vertical center and one inch above and below. As those sensors have been in the core since 1962 there has been a long history of radiation exposure and two out of this six sensors are no longer working. The uncertainty of those sensors is rather high (about $\pm 5\text{ }^{\circ}\text{C}$).

The energy deposited in materials (and hence the material heating) can be calculated with MCNP by using energy and/or heating tallies. The heating (F6) and energy deposition (F7) tallies are merely flux tallies (F4) multiplied by an energy-dependent multiplier (FM card). The units of the heating tally are MeV/g. The materials in question are the materials of rod E13 (the rod equipped with the thermocouples still in operation). Beyond this heating and energy deposition calculations have been made for all other rods including the dummy graphite and regulating rods. For rod E13, the results have been compared to experimental results in section 8.5.

Energy deposition in the water has also been calculated which provides information about the shielding properties of the water above the core (and hence the estimated dose rate at the reactor platform). Dose rate calculations for the experimental setup described in 8.7.1 have been implemented, too. The latter are described in section 8.7 experiments.

For this task a MCNP calculation with the current core model has been done with 100.000 initial particles per run has been done together with a mesh overlay for the whole core.

MCNP tally outputs are normalized to per initial fission neutron, therefore the output has to be multiplied by several factors to get real physical values. To obtain values for energy deposition under real operating conditions, first the target power (in Watts) has to be defined. Afterwards, the number of fissions per second for the given number of Watts can be determined in the following manner:

$$f_{U235} \left[\frac{1}{W_s} \right] = \frac{J}{W_s} \frac{MeV}{1.602E^{-19}J} \frac{1}{180.88MeV} = 3.45110^{10} \left[\frac{fissions}{Watt} \right] \quad (7.8)$$

The value of interest can then be calculated by multiplying the tally results by the desired power in Watts and by the result of equation 7.8.

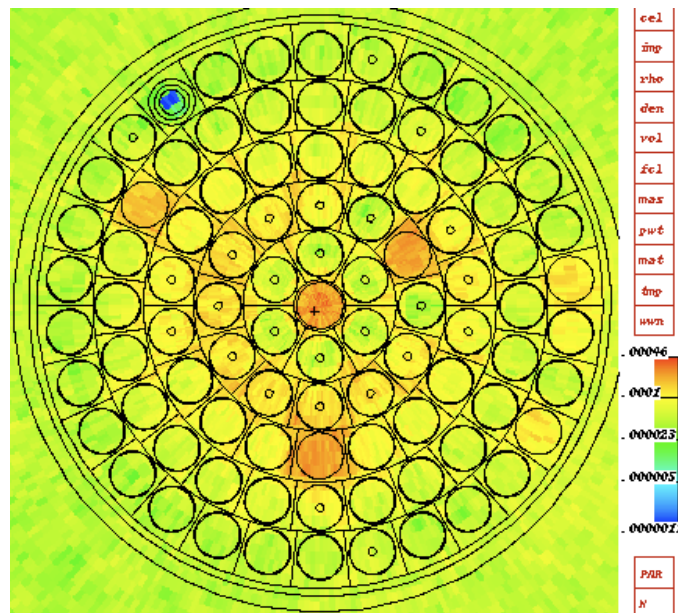


Figure 7.65: Energy deposition in MeV/g per initial fission neutron, $z = 0$

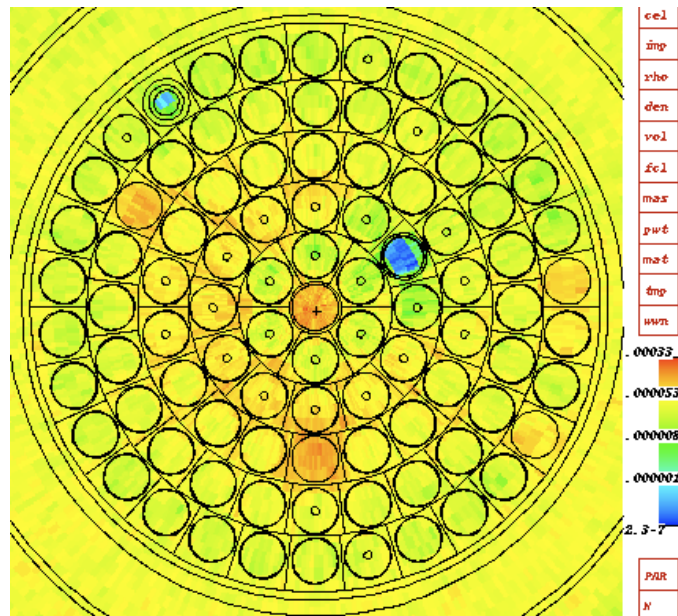


Figure 7.66: Energy deposition in MeV/g per initial fission neutron, $z = 15$

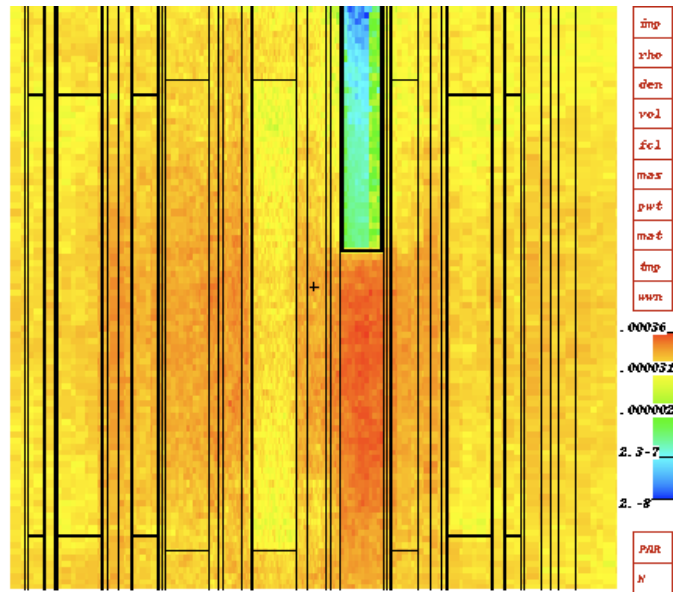


Figure 7.67: Energy deposition in MeV/g per initial fission neutron, close-up of shim rod

Heating and energy deposition in rod E13

In this simulation, a mesh tally of rod E13 has been superposed onto the Triga core model to estimate the energy deposition of rod E13. As this simulation can be verified directly by comparison to an actual experiment, this simulation is described together with the experiment in section 8.5.

7.9 Xenon buildup

The Xenon concentration depends on the neutron flux history and can be described by using the relations introduced in section 4.9. According to that chapter, numerical solutions for the development of Xenon and Iodine concentrations with time have been implemented. The calculations resulted in an equilibrium between Xenon production and decay after approximately 50 hours which is in accordance with analytical results and literature values [16; 12].

The Iodine and Xenon concentrations in equilibrium are given by the equations 4.15 (for Iodine) and 4.19 (for Xenon). A graphical representation of the results can be found in figures 7.68 and 7.69.

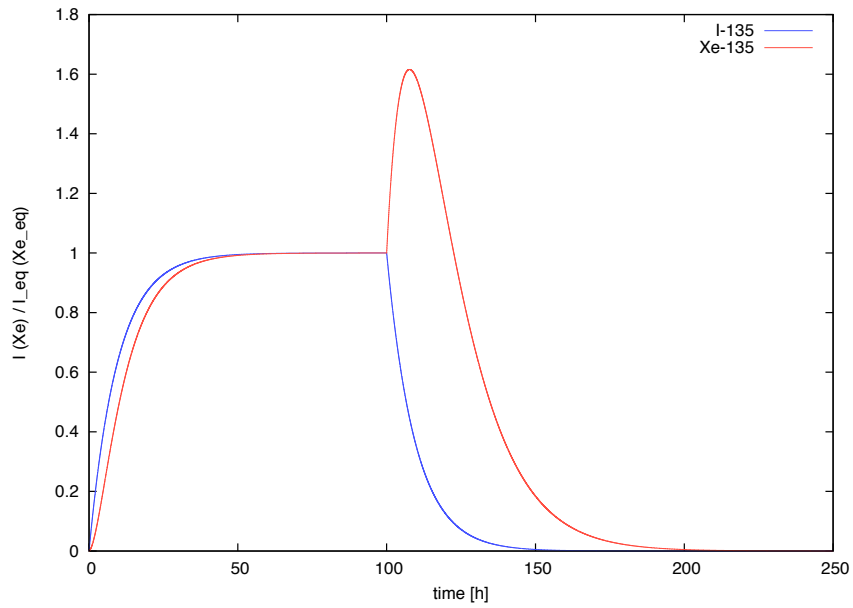


Figure 7.68: Buildup and decay of ^{135}Xe and ^{135}I for a neutron flux of 10^{13} ns^{-1} . Values are given relative to the equilibrium values $^{135}\text{Xe}_{\text{eq}}$ and $^{135}\text{I}_{\text{eq}}$ (see text).

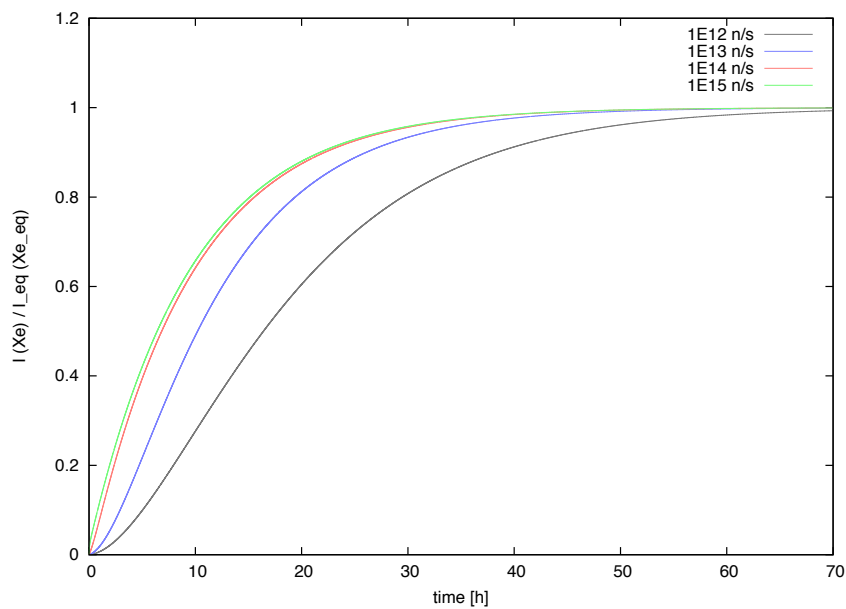


Figure 7.69: Xenon buildup: ratio of $^{135}\text{Xe} / ^{135}\text{Xe}_{\text{eq}}$ versus time for different neutron fluxes.

Chapter 8

Experimental verification

IT DOESN'T MATTER HOW BEAUTIFUL YOUR THEORY IS, IT DOESN'T MATTER HOW SMART YOU ARE. IF IT DOESN'T AGREE WITH EXPERIMENT, IT'S WRONG. *Richard Feynman*

8.1 Water temperature

Temperature measurements at cold shutdown and full power were used to fit a linear equation $f(x) = a + bx$ with x being the reactor power in kW to the measured temperature values. The fit converged to $a = 21.0$ and $b = 4.8e - 05$.

8.2 Fuel temperature

The temperatures of fuel, cladding and water were adapted for each reactor state to model the problem in an appropriate manner. To generate values for the input files the data described in section 8.5 has been used to fit a function $f(x) = a + bx + cx^2$. The parameters converged to

a	= 27.549	+/- 1.774	(6.441\%)
b	= 0.688319	+/- 0.03323	(4.828\%)
c	= -0.000816228	+/- 0.0001292	(15.83\%)

8.3 Power versus shim rod position

The measurements described in section 8.4 were used to acquire the power versus shim rod position calibration curve for the MCNP input file. The fit converged to $f(x) = a + bx + cx^2$ together with x being the power in Watts. The power versus shim rod position is almost linear

for rod positions 150 and above. For positions below 150, a power between zero and ten Watts has been assumed which fits the experimental values. The fit parameters are listed below.

a	= -181320	+/- 1.987e+04	(10.96\%)
b	= 1011.12	+/- 187.9	(18.59\%)
c	= 0.917091	+/- 0.4237	(46.2\%)

8.4 Shim rod reactivity calibration

The shim rod reactivity calibration was done by measuring the reactor period at various shim rod position intervals starting from steady-state 10W reactor power. Starting with a shim rod position at position 150 and steady-state 10W reactor power, the shim rod position has been increased promptly by 30 steps and the duration between 30-45W, 40-60W, 50-75W and 60-90W (50% increase in reactor power in each case) were measured (six measurements per interval).

The mean value of this six measurements is then converted to the reactor period by using the relation

$$P_t = P_0 e^{\frac{t}{T}} \Rightarrow T = 2.46t \quad (8.1)$$

The reactivity is then calculated using

$$\rho = \frac{l}{l+T} + \frac{T}{l+T} \frac{\beta}{1+\lambda T} \quad (8.2)$$

Table 8.1 shows the measured values, their means and the resulting reactor period as a function of the shim rod position together with the calculated and cumulative reactivities. The latter versus shim rod position are shown in Fig. 8.1.

The same curve can be obtained by using MCNP, calculating the value k_{eff} for each position of the shim rod and using the relation

$$\rho = \frac{k-1}{k} \quad (8.3)$$

or by calculating k_{eff} via MCNP and calculating k_{eff} from the experimental reactivity data via the relation

$$\rho = \frac{1}{1-k} \quad (8.4)$$

The MCNP model of the reactor has been modified to represent shim rod positions in the interval [100,400] together with both transient and regulating rod at position 500. An overview of the model is presented in fig. 8.3. The values for k_{eff} have been calculated for both the standard core (shown in fig. 7.4) and the lab course core (shown in fig. 7.5) for shim rod positions between step 100 and 400 in 25cm steps each. The results are shown in fig. 8.3 and show matching reactivity per unit length but different absolute values for k_{eff} .

Table 8.1: Experimental data

SR pos.	t_1	t_2	t_3	t_4	t_5	t_6	\bar{t}	T	ρ_{abs}
150	8.770	9.100	8.870	8.830	9.500	8.870	8.990	22.205	0.270
180	8.530	8.580	8.510	8.650	8.820	8.030	8.520	21.044	0.280
210	9.960	8.700	8.930	9.420	8.820	9.210	9.173	22.658	0.266
240	9.750	9.900	9.870	9.760	9.540	10.120	9.823	24.264	0.260
270	10.070	11.220	11.370	11.960	11.440	11.750	11.302	27.915	0.240
300	6.470	6.460	5.920	6.600	6.550	7.010	6.502	16.059	0.320
330	6.840	7.530	7.570	7.740	7.790	7.310	7.463	18.434	0.300
360	13.440	14.310	14.290	14.530	14.140	13.890	14.100	34.827	0.210
390	63.920	62.810	62.990	55.340	64.550	65.800	62.568	154.544	0.060

SR pos.	ρ [c]	$\Sigma \rho$ [c]
150	0.270	0.270
180	0.280	0.550
210	0.266	0.816
240	0.260	1.076
270	0.240	1.316
300	0.320	1.636
330	0.300	1.936
360	0.210	2.146
390	0.060	2.206

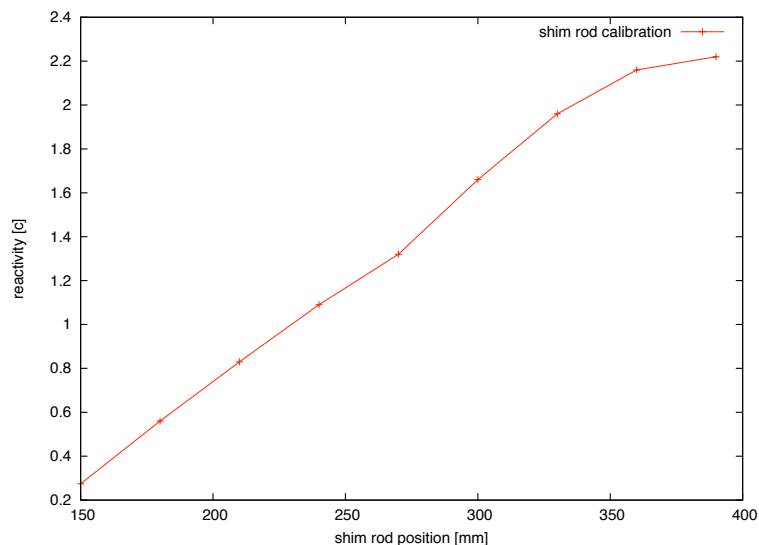


Figure 8.1: Cumulative reactivities versus shim rod position.

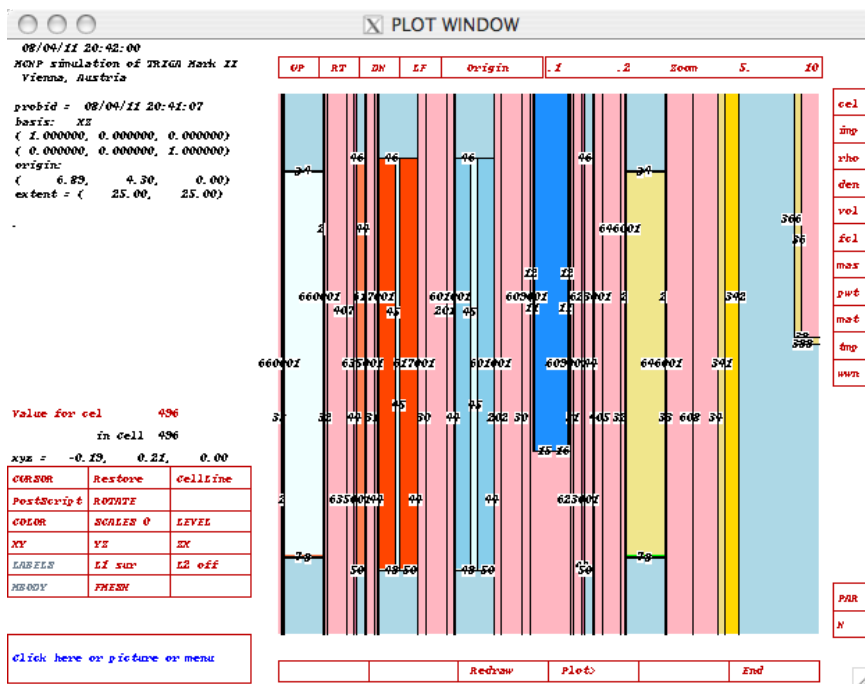


Figure 8.2: MCNP model for shim rod at position 150 (shown in petrol blue)

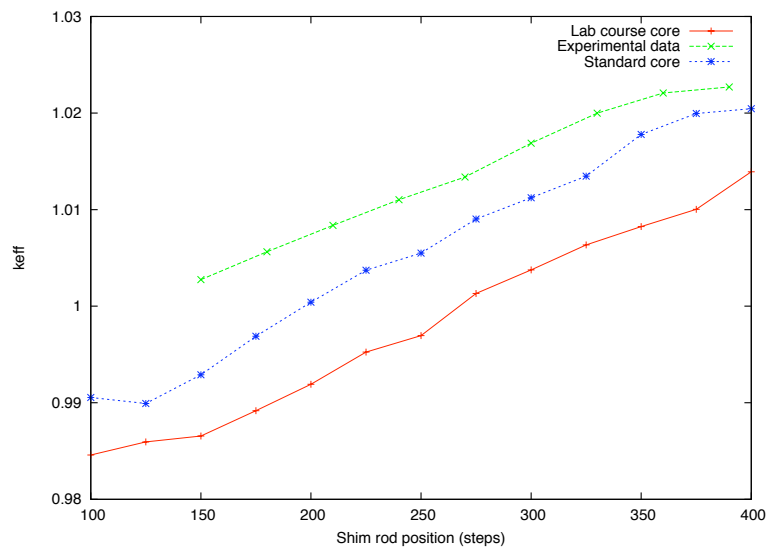


Figure 8.3: Results of MCNP calculations of the shim rod reactivity per unit length versus experimental data

8.5 Reactor core temperature

8.5.1 Experimental setup

The fuel temperature has been measured by the temperature sensors within rod E13 (positioned at the center and ± 1 inch above and below) and recorded for several different reactor power levels. The temperature changes within the fuel rod are nearly instantaneous.

8.5.2 Experimental results

Table 8.2: Temperature measurements (rod E13) for various reactor power levels

Power [kW]	SR pos.	+1in [°C]	center [°C]	-1in[°C]	uncertainty [\pm °C]
5	157	35	30	28	5
20	169	38	39	39	5
40	178	53	51	52	5
60	196	67	63	55	5
80	218	74	72	74	5
100	227	86	84	85	5
120	235	99	96	100	5
140	254	111	106	109	5
160	265	118	113	115	5
180	280	125	120	125	5
200	295	133	131	131	5
220	307	140	135	139	5
250	316	147	146	149	5

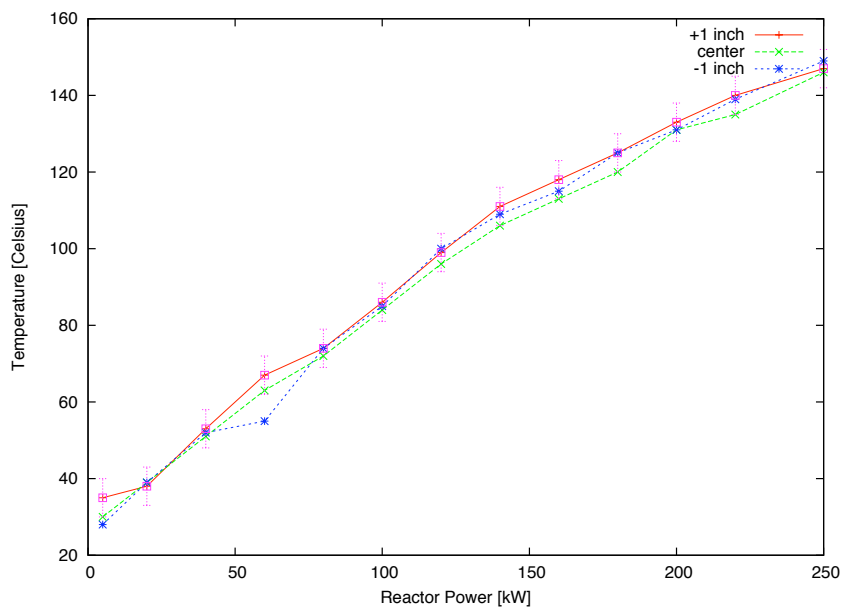


Figure 8.4: Fuel temperatures versus reactor power.

8.5.3 Comparison of experimental and MCNP results

The fission heating of various positions in rod E13 has been calculated by MCNP and converted to temperature changes as follows.

The output of MCNP is normalized to per initial fission neutron. The neutrons per fission number is given in the MCNP output file (2.463 neutrons per fission in this case). The number of fission per Watt-second equals $3.451E+10$ (see equation 7.8). The flux multiplier is given by the number of the total power P in Watts times the fissions per Watt-second times the number of neutrons per fission. To convert from MeV to Joules, the factor $1.603E-13$ has to be applied, too.

Given the numbers listed above, to get the energy deposited per gram and second E_{real} the MCNP tally results E_{MCNP} have to be multiplied by

$$E_{real} = E_{MCNP} * P * (3.45110E + 10) * 2.463 * (1.602E - 13) \quad (8.5)$$

The changes in fuel temperature are nearly instantaneous, so after one second of energy deposition thermal equilibrium is assumed. The heat capacity of Uranium ($0.116 \text{ J g}^{-1} \text{ K}^{-1}$) is then used to convert the deposited energy into temperature changes.

The results of the calculations are listed in table 8.5.3 and shown in fig. 8.5. A comprehensive overview about height dependent temperature changes in rod E3 for various power levels are presented in fig. 8.6.

Power [kW]	Experiment (average) [°C]	MCNP [°C]
5	31	30
20	38	36
40	52	48
60	61	67
80	73	73
100	85	87
120	98	97
140	108	107
160	115	117
180	123	127
200	131	127
220	138	137
250	147	152

Table 8.3: Comparison of experimental and MCNP results for temperature changes in rod E13 during the experiment

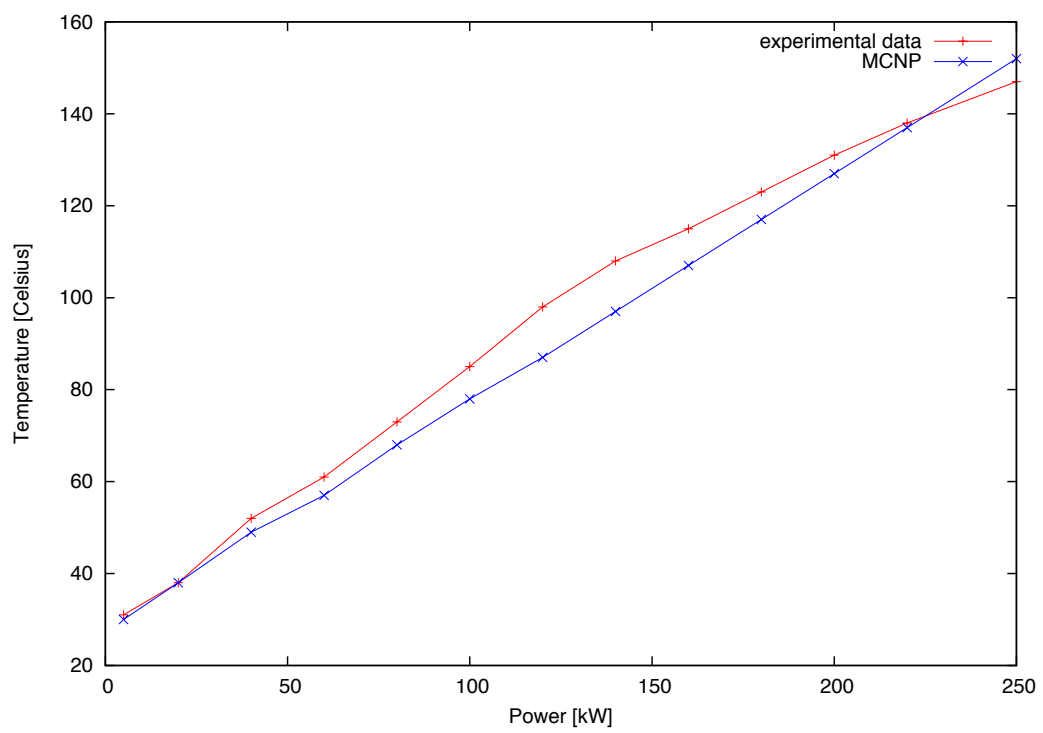


Figure 8.5: Comparison of experimental and MCNP data for temperature changes in rod E13 for various power levels

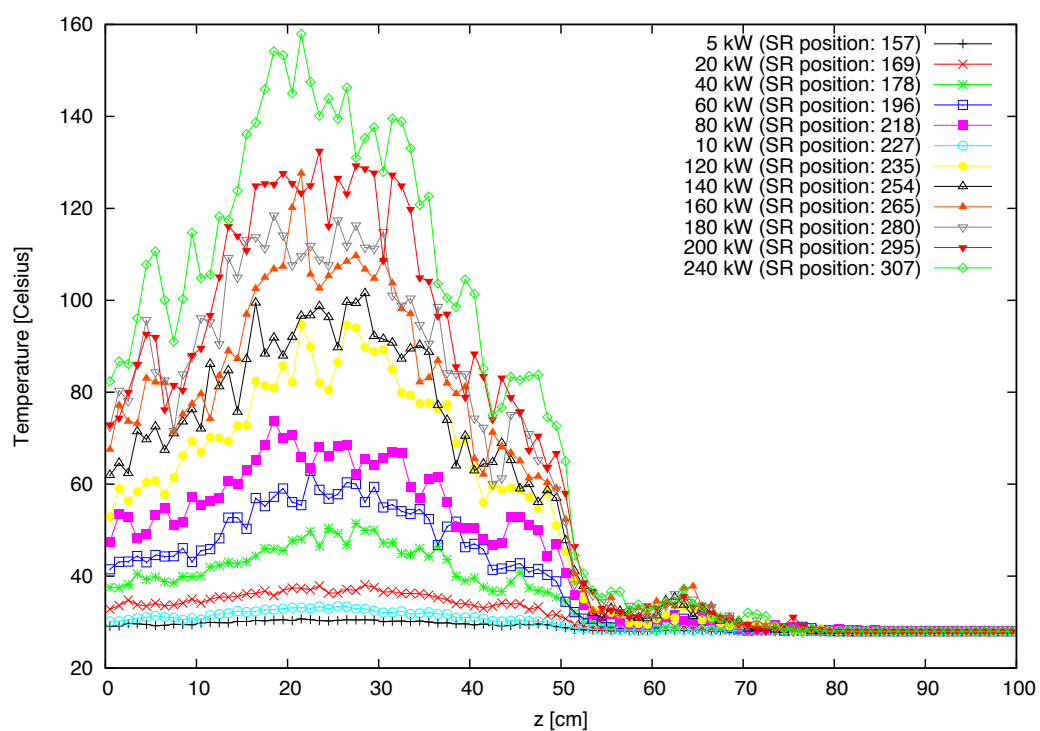


Figure 8.6: Energy deposition in rod E13, 5kW to 250kW

8.6 Reactor power development with time for various reactivity inserts

8.6.1 Experimental setup

The primary focus of this experiment was to gather information about the influence of reactivity changes on the reactor power and especially to record the change of power versus time to build a basis for the comparison of numerical simulations to the experimental data.

Measurement of reactor power at TRIGA Vienna is done by fission chambers. The signal of one fission chamber has been used to record time dependent neutron flux (and hence reactor power) data. The fission chamber has been connected to an Amperemeter and the resulting signal has been recorded by a simple LabView application.

As the Amperemeter used was not the one planned originally for this task a few calibrations had to be done beforehand, as the LabView application was designed for usage of the original (Keithley) amperemeter and the software built-in scaling factors did no longer apply. The Amperemeter has been calibrated by using a standard current generator to deliver a defined current input signal and recording both the gain settings of the amperemeter (A/V) and the software scale area. The resulting calibration is linear and shown in figure 8.7.

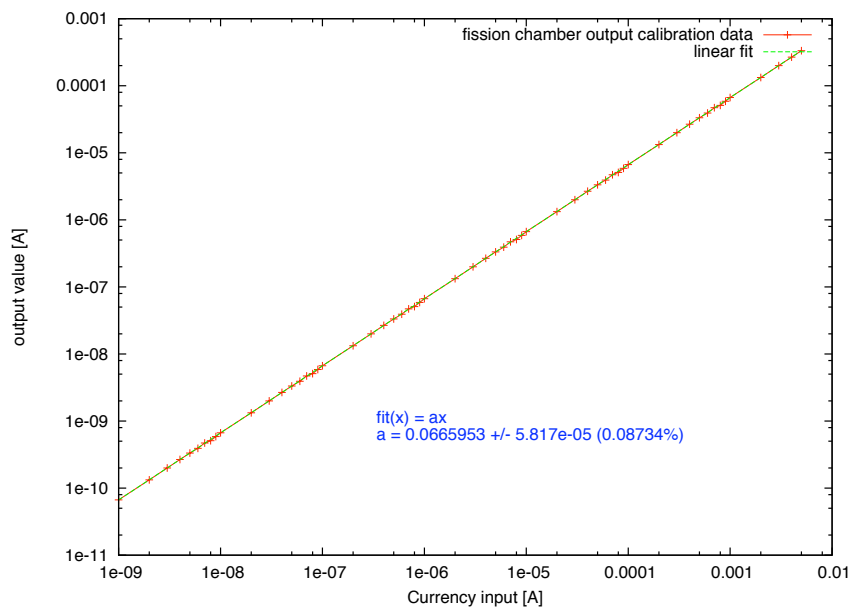


Figure 8.7: Amperemeter calibration

Starting at a steady-state power level of 10W with the transient and regulating rods fully

withdrawn from the core, the current on the fission chamber (CH) has been recorded. The shim rod has been moved from its steady state position (155) up with the steps described in table 8.4. The power levels and temperatures at each stable position have been recorded to make a fission chamber signal vs. reactor power calibration possible. An overview of the recorded, time dependent data is shown in fig. 8.8.

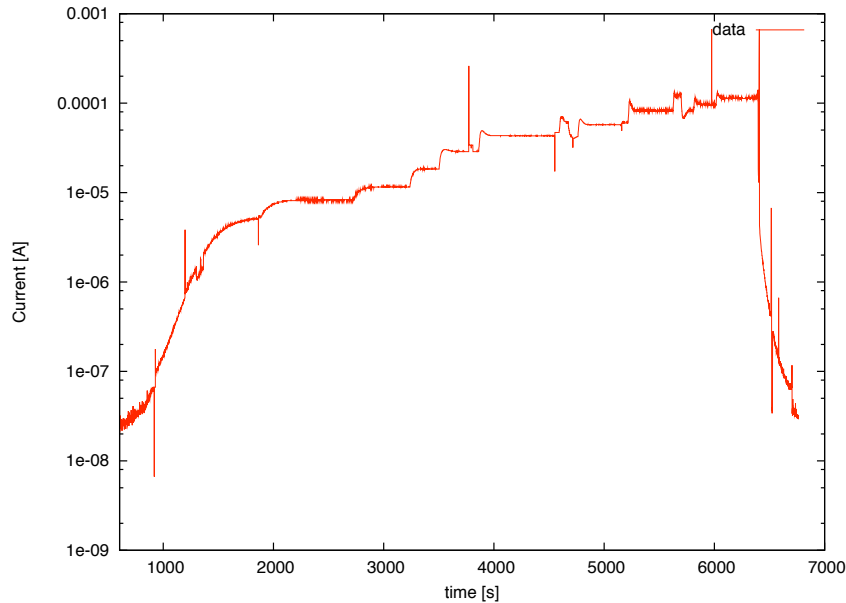


Figure 8.8: The complete data record for the reactivity feedback measurements as an overview. Note the clearly visible temperature feedback effects showing at about an hour after measurements started. The sharp peaks are artefacts caused by changes in the Amperemeter gain settings.

At different stable positions (see table 8.5) the power versus current values were taken to obtain a power calibration. The data has been fitted linearly resulting in a fit function $f(x) = a + bx$ with the parameters

$$a = 1.85806e-06 \pm 3.024e-06 \text{ (162.8\%)}$$

$$b = 7.66269e-07 \pm 2.371e-08 \text{ (3.095\%)}$$

The resulting data and the fit are shown together in fig. 8.9.

The power calibration fit is reasonable except for the very low power of 10W. This is caused by the large uncertainty of the offset parameter a due to statistic reasons (the curve is defined at this very low level by just one point). Steady-state current at a power of 10W has been noted manually and is shown at the very left of figure 8.8 (approximately 1.3E-08 Ampere before calibration correction).

Table 8.4: Experimentally determined values for power and temperature. The reactivity has been calculated from an interpolation of the values gained by a preceding experiment. The power and temperature values were taken before the reactivity has been inserted.

Phase	Uhrzeit	Time [s]	Power (vorher)	Temp (vorher)	rod from	rod to	rho [c]
1	10:35:09	614	35 W	35	155	165	0.0903
2	10:56:31	1896	9.5 kW	40	165	170	0.0452
3	11:10:23	2728	15.5 kW	45	170	175	0.0452
4	11:18:55	3240	22 kW	50	175	185	0.0903
5	11:23:17	3502	-	60	185	200	0.1355
6	11:29:17	3862	59 kW	70	200	220	0.1807
7	11:44:16	4761	59 kW	85	220	240	0.1807
8	11:51:50	5215	115 kW	100	240	270	0.2710
9	12:01:50	5816	158 kW	-	270	290	0.1807
10	12:05:12	6017	189 kW	130	290	310	0.1807

Table 8.5: Power calibration data. A/V is the gain setting on the SR Amperemeter, the LV scale factor means the factor given by the LabView application, the resulting factor is given by $10 \times \text{LabView factor} / \text{SR factor}$.

Power [kW]	Temp.	Current[A]	A/V	LV scale fac.	res. factor	SR pos.
9.5	40	7.61E-5	1.00E-05	1.00E-05	1.00E-01	165
15.5	45	1.22E-5	1.00E-04	1.00E-05	1.00E+00	170
22	50	1.73E-5	1.00E-04	1.00E-05	1.00E+00	175
59	70	4.31E-5	1.00E-04	1.00E-05	1.00E+00	200
65	76	6.51E-5	1.00E-04	1.00E-05	1.00E+00	220
115	100	8.63E-5	1.00E-04	1.00E-05	1.00E+00	240
150	115	1.22E-5	1.00E-03	1.00E-05	1.00E+01	270
158	115	1.18E-5	1.00E-03	1.00E-05	1.00E+01	270
160	115	1.22E-5	1.00E-03	1.00E-05	1.00E+01	270
189	130	1.45E-5	1.00E-03	1.00E-05	1.00E+01	290
220	140	1.73E-5	1.00E-03	1.00E-05	1.00E+01	310

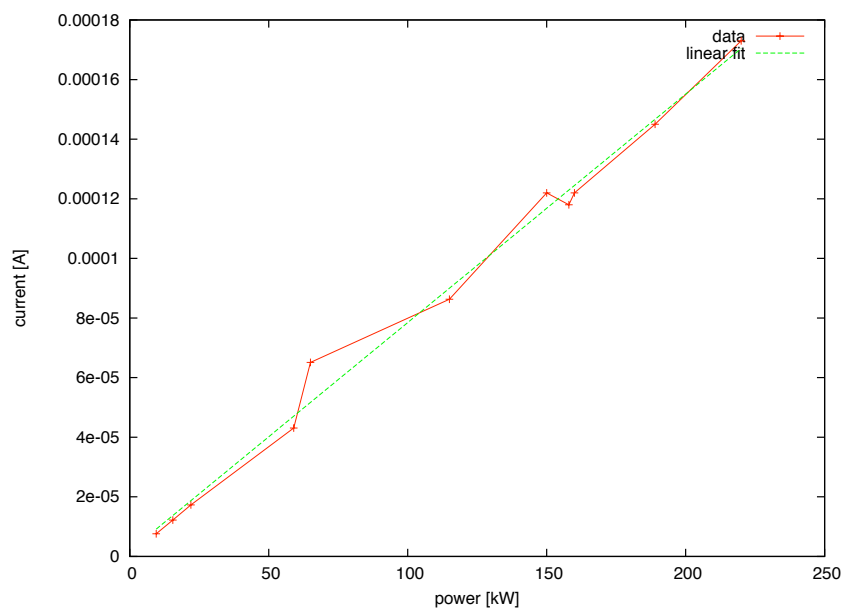


Figure 8.9: Final power calibration using the data from table 8.5. Note that the data shown in this table are values before correction with the calibration from the Amperemeter calibration data fit.

8.6.2 Results

The model described in chapter 5 has been applied to the experimental conditions described in section 8.6.1. The input values for initial temperature, inserted reactivity, temperature feedback coefficients and the thermal feedback time constants have been adapted to each step as described above. The steady-state of step n-1 has been taken as the new starting point for each step n.

The results of the numerical calculations are shown together with the experimental data in figures 8.10 to 8.16.

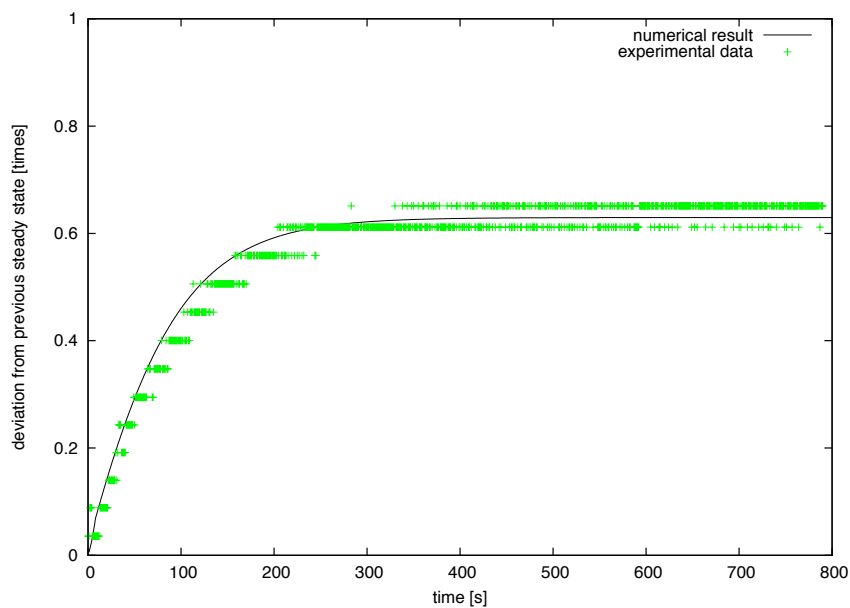


Figure 8.10: Deviation from steady state: Experimental versus numerical results for the first step

8.6.3 Discussion

The numerical results are found to be in good agreement if the correction factors described in section 5 are considered. A detailed investigation of these correction factors currently is in progress. Further studies are needed to include feedback caused related to the void coefficient of reactivity and reactivity changes caused by Doppler broadening. This has not taken into account as the temperature feedback coefficient clearly is the dominant factor when looking at the TRIGA reactor in Vienna. The results are not expected to change significantly.

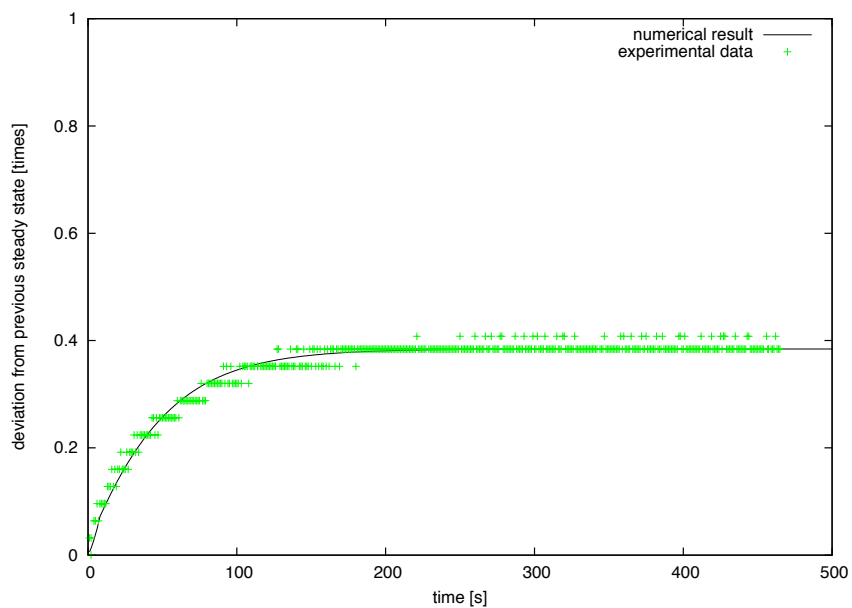


Figure 8.11: Deviation from steady state: Experimental versus numerical results for the second step

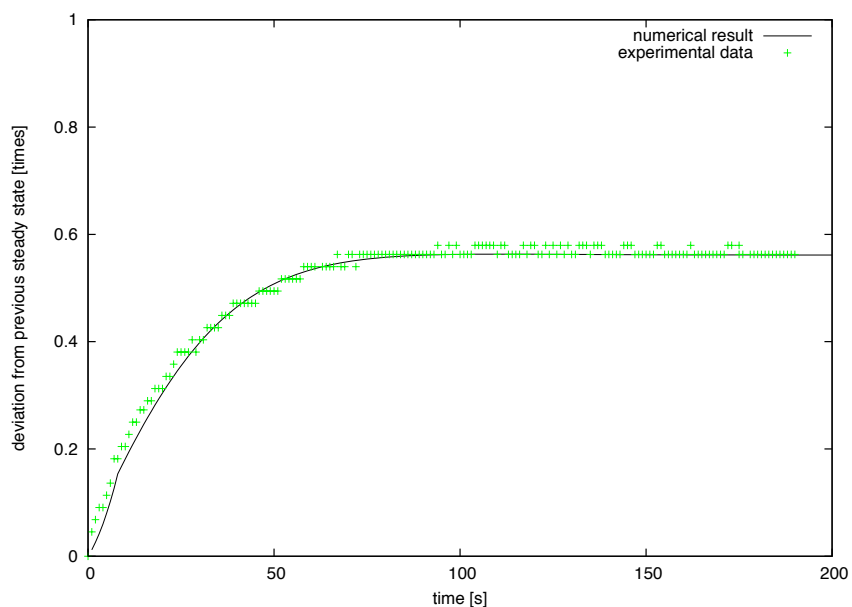


Figure 8.12: Deviation from steady state: Experimental versus numerical results for the third step

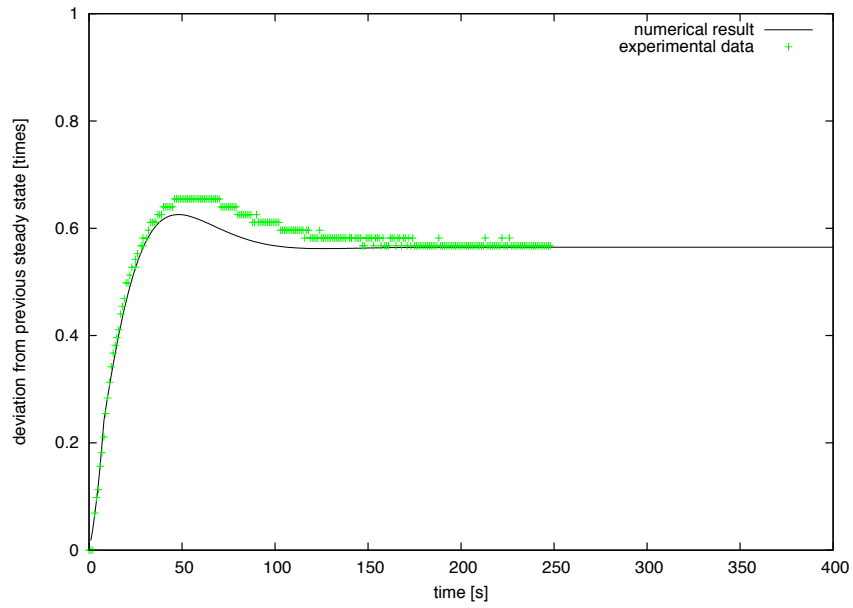


Figure 8.13: Deviation from steady state: Experimental versus numerical results for the fourth step

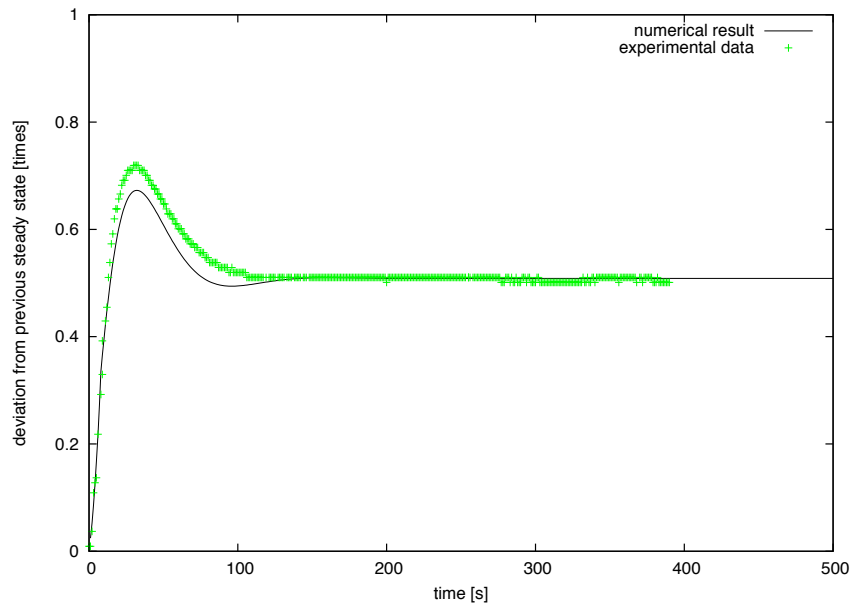


Figure 8.14: Deviation from steady state: Experimental versus numerical results for the fifth step

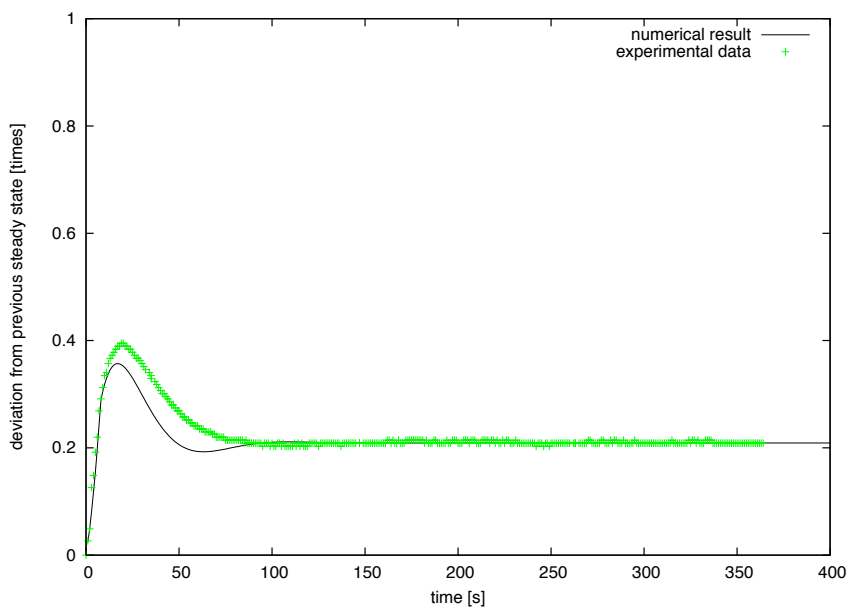


Figure 8.15: Deviation from steady state: Experimental versus numerical results for the sixth step

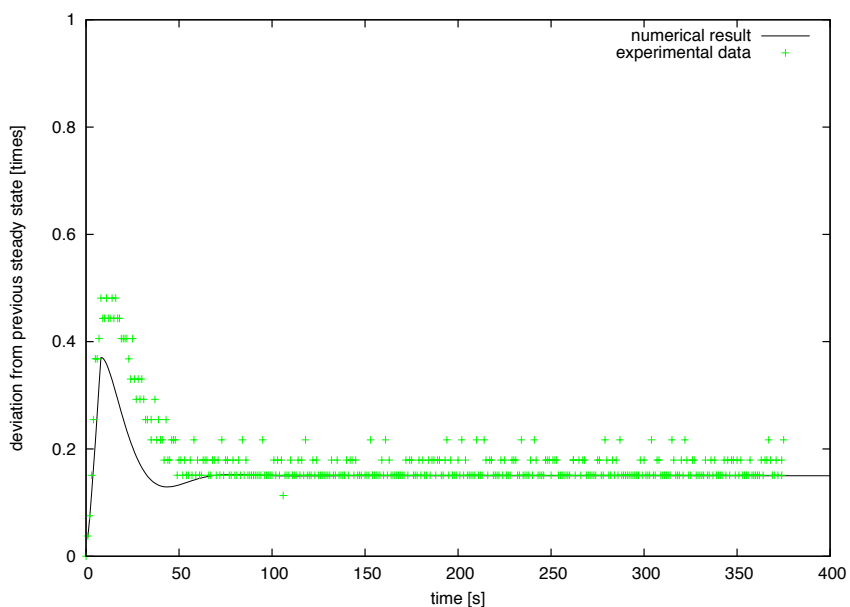


Figure 8.16: Deviation from steady state: Experimental versus numerical results for the seventh step

8.7 Incore gamma dose rate measurements

The original intention for trying in-core spectrometry originated from the need for experimental data for reactor poisoning caused by the nuclide ^{135}Xe . The idea was to find a way to measure the Xenon content in the fuel by generating a setup which measures the gamma rays emitted in the decay of this nuclide. The dominant gamma energy is 250keV.

Usually Xenon measurements by gamma spectrometry in the radiation field of a nuclear reactor, even when not operating, are considered to be very difficult. The reason for this is that the low energy of this decay is located in an area of the spectrum where reactor background is high. Another difficulty of in-core gamma spectrometry are the generally high dose rates. Applying lead shielding to reduce it results in weakening especially of the lower energy spectrum part which also influences the 250 keV peak to be measured.

The attempt to solve this difficulties and get reasonable results has been the usage of both CdZnTe and HPGe detectors and short measurement intervals (between 300 and 900 seconds). Dose rate measurements have been tried with CdZnTe detectors with very long cables fitting into the beamline cylinder (see description of the experimental setup below).

8.7.1 Experimental setup

The setup for this experiment (and also for the general gamma ray spectrometry and the Xenon and Iodine measurements) consisted of an High Purity Germanium detector (Princeton Gamma Tech) and a Zinc Cadmium Telluride detector (RITEC SDP 310/Z) together with a Multi Channel Analyzer manufactured by GBS (MCA166). The system was connected to a personal computer via serial bus for recording purposes.

As the measurements had to be done as close to the fuel as possible the fuel has been transferred from its original position to a mounting device made out of Aluminium shown in fig. 8.17. The cylinder in the middle holds the fuel element and can be rotated from an upright to ground plane parallel position (shown in the picture). The upright position is needed for easier fuel rod handling.

The cut in the upper side of the cylinder holding the fuel rod is equipped with a moveable device including a winding to fix a hollow Aluminium cylinder. This provides an air-filled tube from the bottom of the reactor tank up to the water surface where the detector is placed thus forming a kind of beamline. This beamline is positioned directly under the detector mounting to ensure an mostly undisturbed beam between the fuel element and the detector.

The beam is weakened by the bottom of the Aluminium tube and collimated by a lead slab with a 5mm hole in the center positioned at the bottom of the Aluminium tube. After placing the fuel rod mounting device onto the thermal column (see fig. 8.21), the Aluminium tube is screwed onto the scanning device thus creating a kind of beamline up to the gamma detector



Figure 8.17: Fuel rod scanning device

mounted at the top. An overview of the upper part of the measurement setup (upper part of the beamline tube and the detector mounting) can be seen in fig. 8.19. Measurements were done with a fuel element withdrawn from the core in February 2001 (element number 2176 from the spent fuel storage within the tank) and with an actual element from the F ring (F5, element number 2170). For element 2176, gamma ray spectrometry has been only done once mostly for testing purposes. For element number 2170, extensive measurements have been done.

An overview about the measurements taken can be found in table 8.7.

The length of the beamline described in section 8.7.1 between the fuel rod scanning device and the upper end of the beamline, near the HPGe detector, was 3.95 meters. The CdZnTe detector has been placed on top of the beamline and then moved towards the lower end of the beamline in 50 cm steps. The count rate at each position has been measured. At the same time, the dose rate directly on the upper end of the beamline has been measured with the Automess dose rate meter available as standard reactor measurement device. It showed an average of 3mSv/h.

The dose rate measurements of the CdZnTe detector and the values converted to dose rate units taking the Automess value as basis are shown in table 8.6.

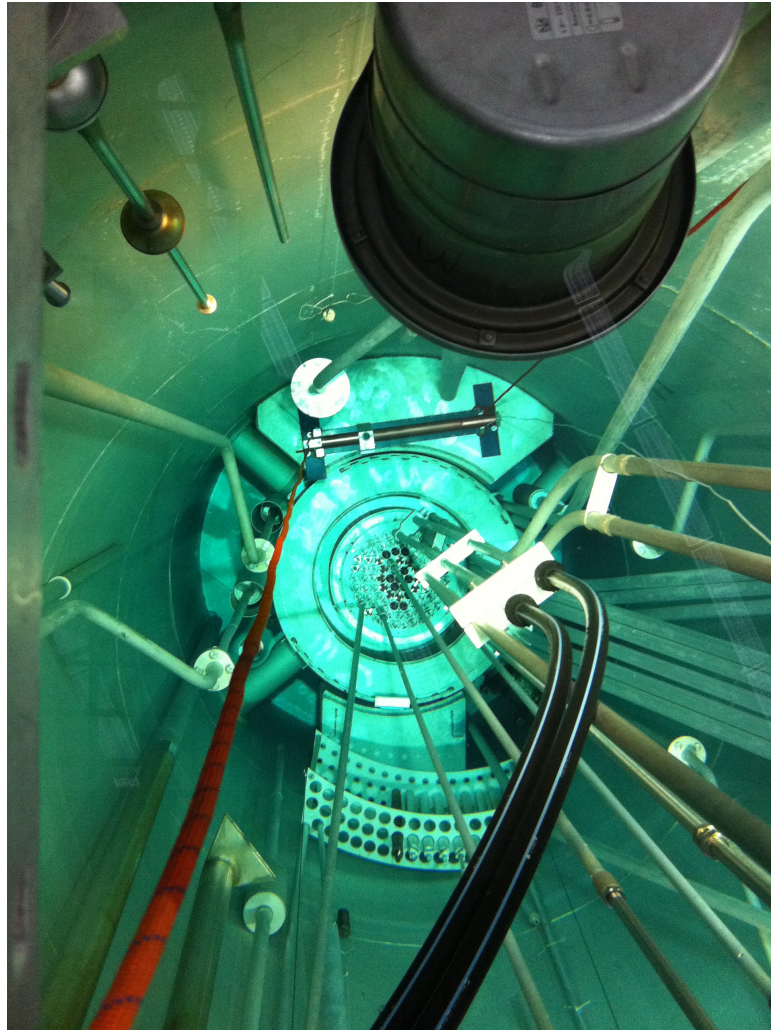


Figure 8.18: Fuel rod scanning device placed onto the thermal column (final position for measurements)

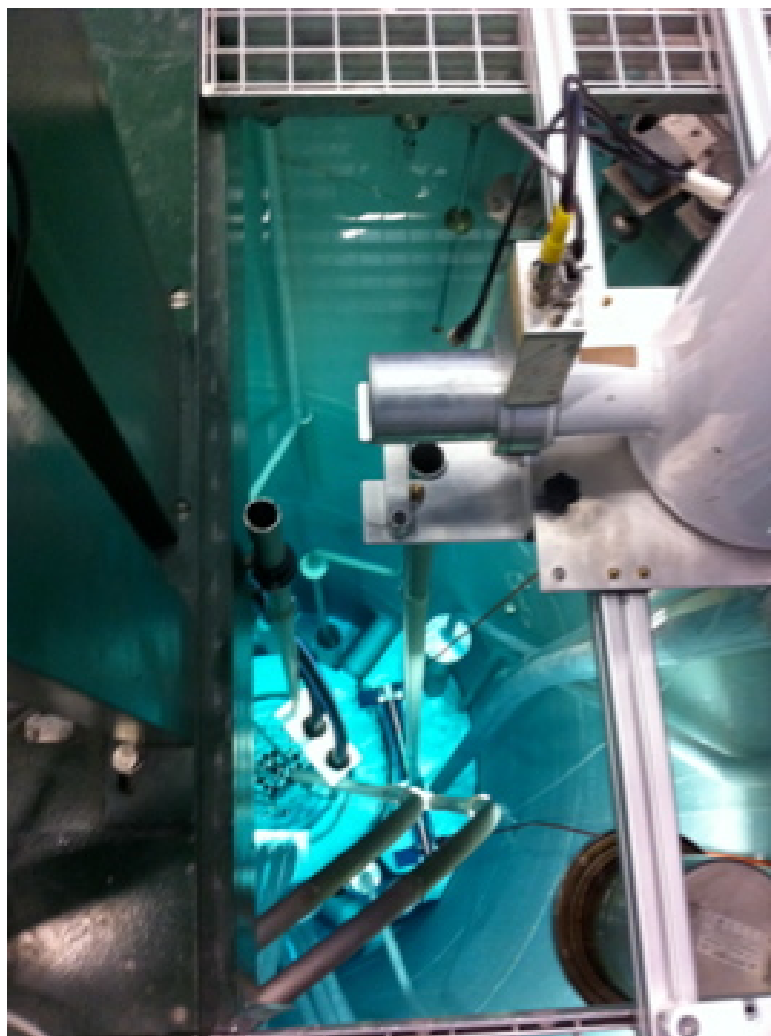


Figure 8.19: HPGe detector over the constructed beamline

8.7.2 Results

Table 8.6: Dose rate measurements in the TRIGA reactor after shutdown. The position (z) is relative to the lower end of the beamline.

Position [cm]	Counts [s^{-1}]	Dead time	Dose rate [$mSv h^{-1}$]
20	453706	99.5%	905.6
40	64991	53.8%	261.3
80	15392	20.2%	70.4
120	11334	15.3%	32.1
140	10057	14.0%	23.8
160	7082	10.4%	18.3
180	4666	6.9%	14.5
200	3095	4.7%	11.8
240	2703	4.0%	8.2
300	1888	2.8%	5.3
320	1172	1.7%	4.6

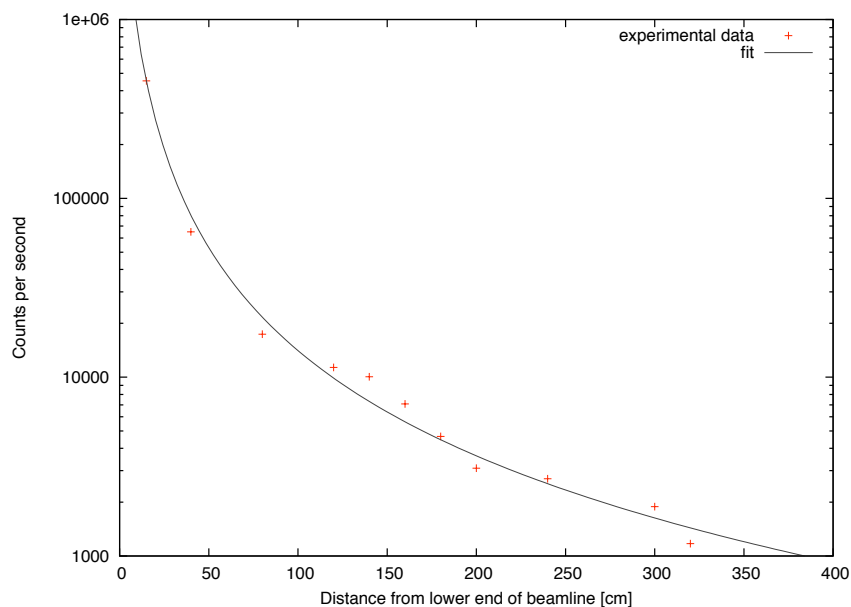


Figure 8.20: Experimental count rate measurements and the corresponding fit

8.7.3 Discussion

As expected, the CdZnTe detector showed such a large dead time after reaching about 20cm above the position of the fuel rod to be measured that the measurement had to be cancelled. The dose rate at the surface of the fuel rod is extrapolated to be in order of kSv/h.

8.8 Gamma spectrometry

8.8.1 Experimental setup

The setup has been the same as for the incore dose rate measurement except for the detector (the HPGe detector described above has been used for gamma spectrometry measurements). Please see section 8.7.1 for details.

Spectra have been recorded automatically starting shortly after reactor shutdown in the afternoon and ending in the morning of the next days with durations between 300 and 600 seconds for each spectrum. The recorded data has then been converted to a format readable by the evaluation program developed during this thesis and the relevant parameters (for example the number of peaks, peak positions and their amplitudes) have been extracted. A total of 1277

Table 8.7: Overview about gamma spectrometry measurements

Actual experiments				
Date	Part	Folder name	Spectrum files	Comment
2011-01-28	pre-midnight	05761101281745	54 (REP0000[00-53]), 300s	Weekend
2011-01-29	all-day	05761101290001	236 (REP00[054-289]), 300s	Weekend
2011-01-30	all-day	05761101300000	150 (REP00[290-439]), 300s	Weekend
2011-01-30	pre-midnight	05761101301640	83 (REP0000[00-82]), 300s	
2011-01-31	post-midnight	05761101310000	96 (REP000[083-178]), 300s	
2011-02-01	pre-midnight	05761102011557	38 (TUE0000[01-37]), 600s	
2011-02-02	post-midnight	05761102020004	48 (TUE0000[38-85]), 600s	

gamma ray spectra have been recorded during this period. Not all of them were usable. It took some time to find a suitable position for the detector to reduce dead time to an acceptable level and some tests with and without lead shielding provided to the detector were performed. A few examples of the measured spectra can be found in figures 8.21 to 8.24. Example analysis has been done for two sets of recorded spectra which are presented below. The following datasets have been used for evaluation:

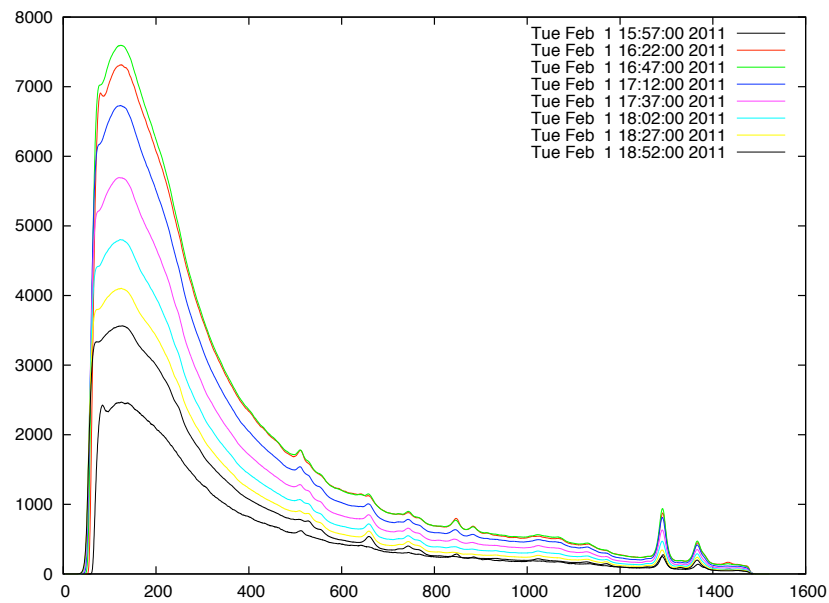


Figure 8.21: Gamma ray spectra (selection) Wednesday pre midnight; x-axis: energy [keV], y-axis: total counts

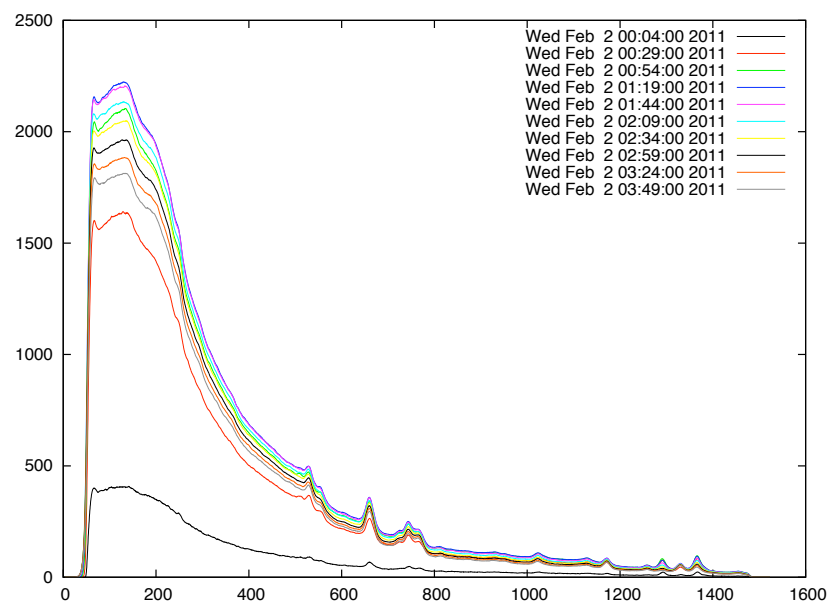


Figure 8.22: Gamma ray spectra (selection) Wednesday post midnight; x-axis: energy [keV], y-axis: total counts

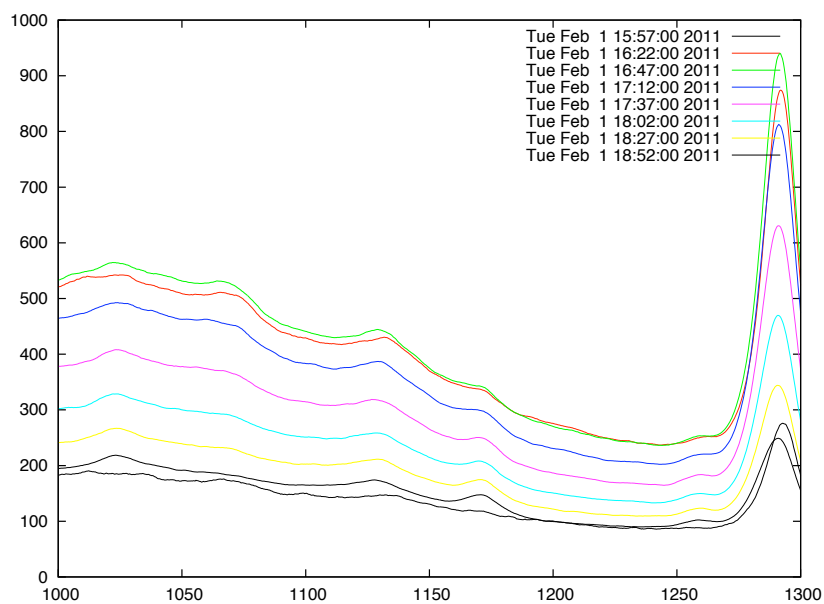


Figure 8.23: Gamma ray spectra (selection) Wednesday pre midnight; x-axis: energy [keV], y-axis: total counts

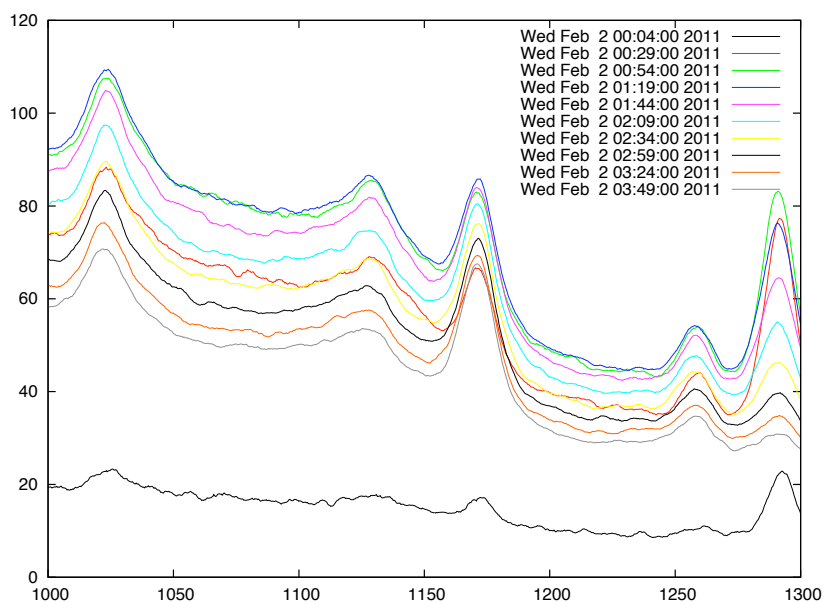


Figure 8.24: Gamma ray spectra (selection) Wednesday post midnight; x-axis: energy [keV], y-axis: total counts

Table 8.8: Datasets used for example analysis

Time range	Duration	# of measured spectra
Jan 28 2011 17:45 - Jan 30 2011 14:50	300s each	439
Feb 1 2011 15:57 - Feb 2 2011 08:40	600s each	84

8.8.2 Analysis: data from Jan. 28th - Jan. 30th, 2011

Identifying peak locations

To find the interesting peak regions, a histogram of all peaks according to the algorithm presented in chapter 6 is generated. Each spike represents one identified peak location in these spectra.

The histogram strongly depends on the given threshold c as defined in chapter 6. If the threshold is too small, too much minima are counted especially in the lower energy band resulting in a noisy analysis for low energy peaks, like for one of the nuclides in question (^{135}Xe at 249.7 keV). This nuclide is then no longer identified correctly. If defining the threshold too small, some weakly defined (by their minima of their second derivatives) peaks like the Iodine peaks at 1131.5 keV and 1260 keV are not identified correctly.

For this purposes, two runs of the same algorithms with different sensitivities. The sensitivity is given in units of the global minimum (all peaks, all spectra) c_{gm} . For correct identification of the low-energy peaks, a threshold of $c = 0.08c_{gm}$ has been used, for the higher energy peaks a threshold of $c = 0.02c_{gm}$ has been used. The generated histogram for the 243 spectra in this time range for $c = 0.08c_{gm}$ is shown in fig. 8.25, for $c = 0.02c_{gm}$ in fig. 8.26 and the two combined histograms to outline their differences is shown in fig. 8.27.

Fig. 8.26 clearly shows the noise in the lower energy range. The amount of peaks identified makes it impossible to clearly distinct between peaks located very closely to each other. On the other hand, it can clearly be seen that many of the peaks in the higher energy range are not correctly identified by using a too small threshold but for $c=0.08c_{gm}$ they are identified correctly.

Analysis of the time dependent peak areas

The amplitudes of the second derivatives (smoothed and non-smoothed) of this 84 example spectra have been investigated using the algorithm presented in section 6.1. For the peaks #7 (^{135}Xe) and #70 (^{135}I) the measurements and their corresponding fits are presented in figures 8.29 and 8.28.

The actual peak areas can then be obtained by using the multiplication factor given in eq. 6.18 resulting in the data presented in figures 8.38 (for ^{135}Xe) and 8.36 (for ^{135}I).

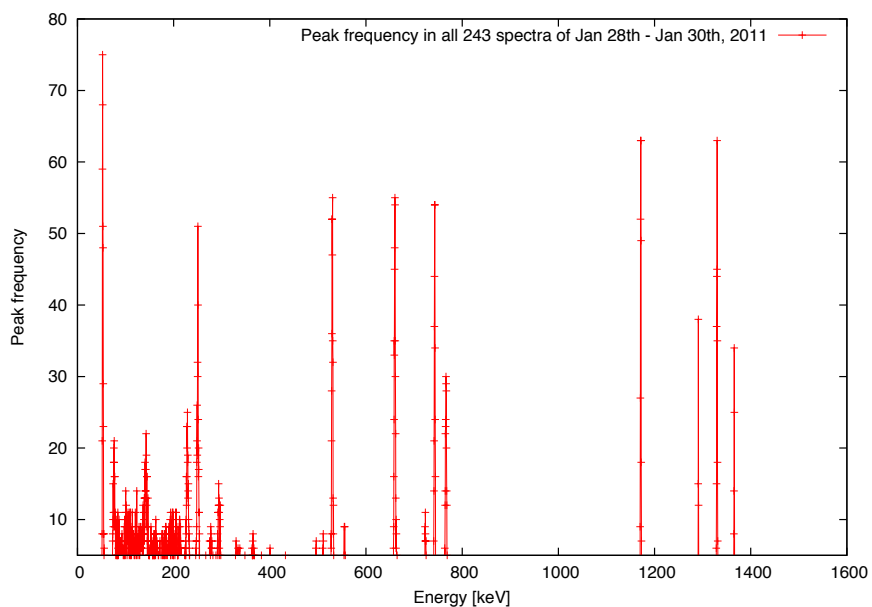


Figure 8.25: Peak frequency in all 243 spectra of Jan. 28th - Jan. 30th, 2011 ($c = 0.08c_{gm}$)

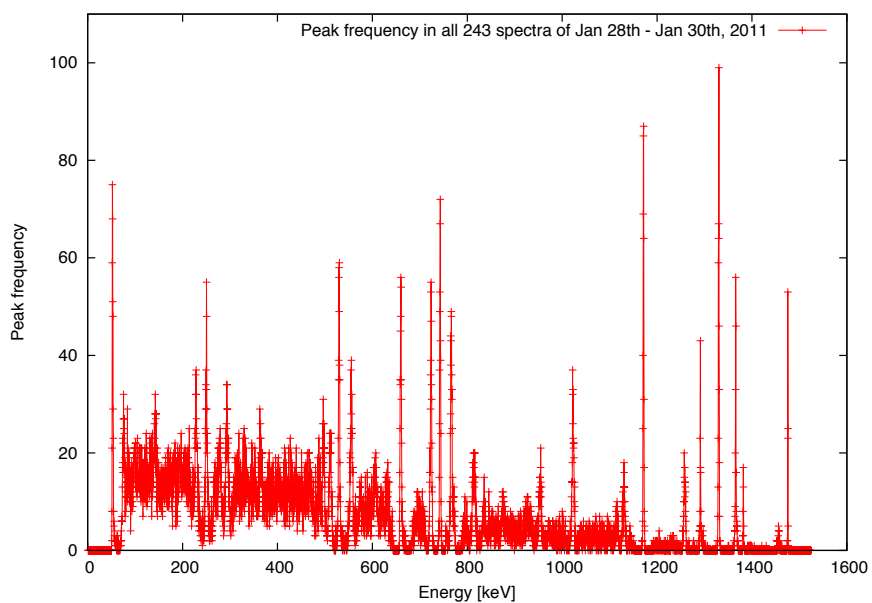


Figure 8.26: Peak frequency in all 243 spectra of Jan. 28th - Jan. 30th, 2011 ($c = 0.02c_{gm}$)

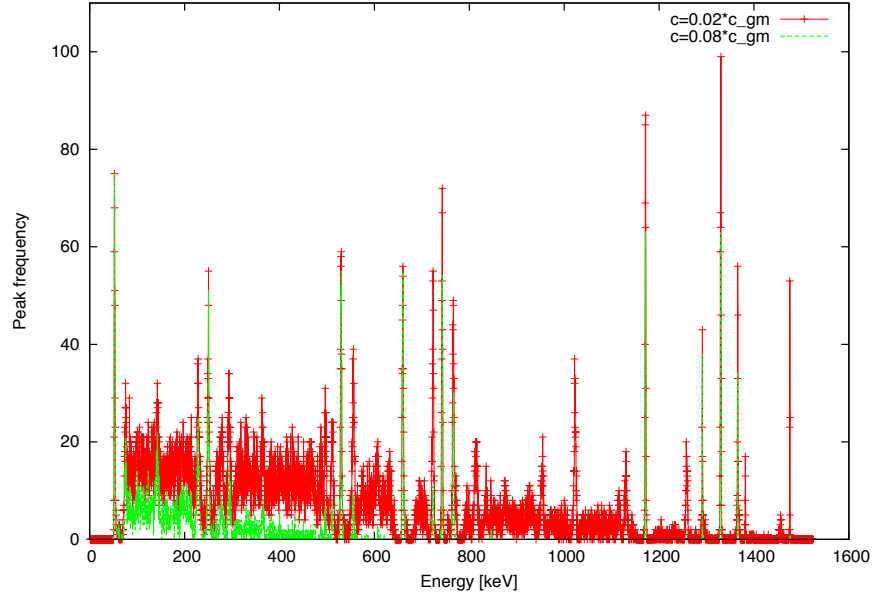


Figure 8.27: Peak frequency in all 243 spectra of Jan. 28th - Jan. 30th, 2011 (combined)

Table 8.9: Identified peaks in the 243 spectra measured between Jan. 28th - Jan. 30th, 2011 (excerpt)

peak #	x_1 [keV]	x_2 [keV]	\bar{x} [keV]	Nuclide
4 ($c = 0.02c_{gm}$)	137.6	149.0	143.3	^{235}U (143.8 keV)
5 ($c = 0.02c_{gm}$)	180.2	188.6	184.4	^{235}U (185.7 keV)
9 ($c = 0.02c_{gm}$)	243.7	257.1	250.4	^{135}Xe (249.7 keV)
31 (both)	507.9	514.3	511.1	annihilation peak (511 keV)
35 (both)	654.4	667.5	660.9	^{137}Cs (661.6 keV))
70 ($c = 0.08c_{gm}$)	1124.8	1135.7	1130.2	^{135}I (1131 keV))
71 ($c = 0.08c_{gm}$)	1166.2	1176.6	1171.4	^{60}Co (1171 keV)
73 ($c = 0.08c_{gm}$)	1287.9	1295.4	1291.6	^{41}Ar (1291 keV)
74 ($c = 0.08c_{gm}$)	1324.7	1335.1	1329.9	^{60}Co (1332 keV)
75 ($c = 0.08c_{gm}$)	1361.3	1370.2	1365.8	^{24}Na (1365 keV))

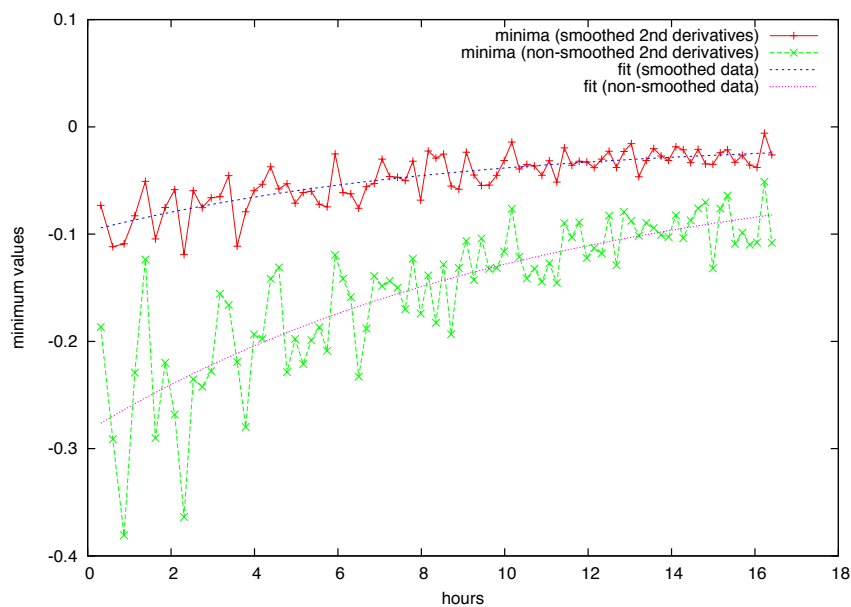


Figure 8.28: Values for the second derivatives of the first ^{135}I peak (1131 keV) over time

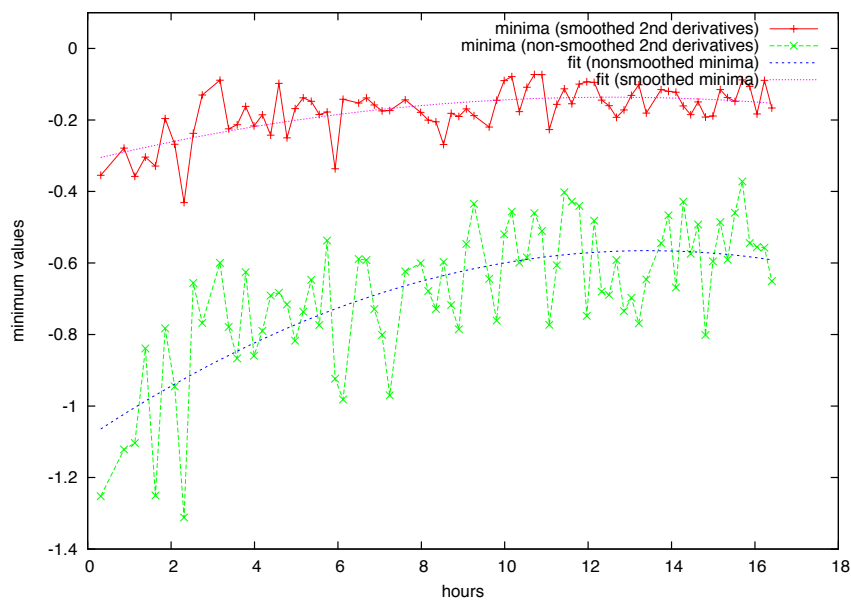


Figure 8.29: Values for the second derivatives of the dominant ^{135}Xe peak (249.7 keV) over time

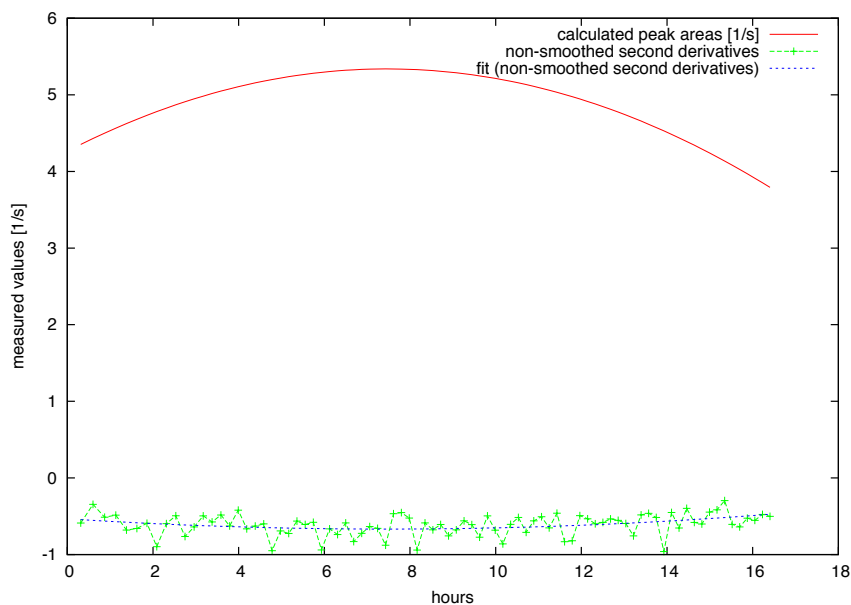


Figure 8.30: Peak areas $[\frac{1}{s}]$ of the dominant ^{135}Xe peak (249.7 keV) over time

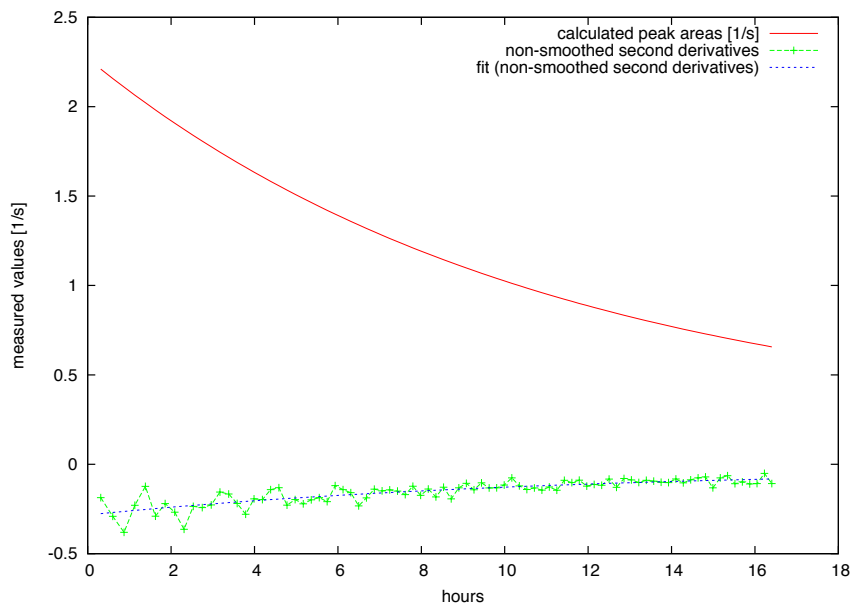


Figure 8.31: Peak areas $[\frac{1}{s}]$ of the first ^{135}I peak (1131 keV) over time

8.8.3 Analysis: data from Feb. 1st, 2011

For illustrational purposes, fig. 8.32 shows the second derivatives per total counts and channel numbers of three different spectra (out of 84 total measured on Feb 01, 2011) recorded after 600s, 22200s and 49800s. Each spectrum had a total measurement time of 600s. The different amplitudes at same peak locations for different times are clearly visible. The zero poles of the

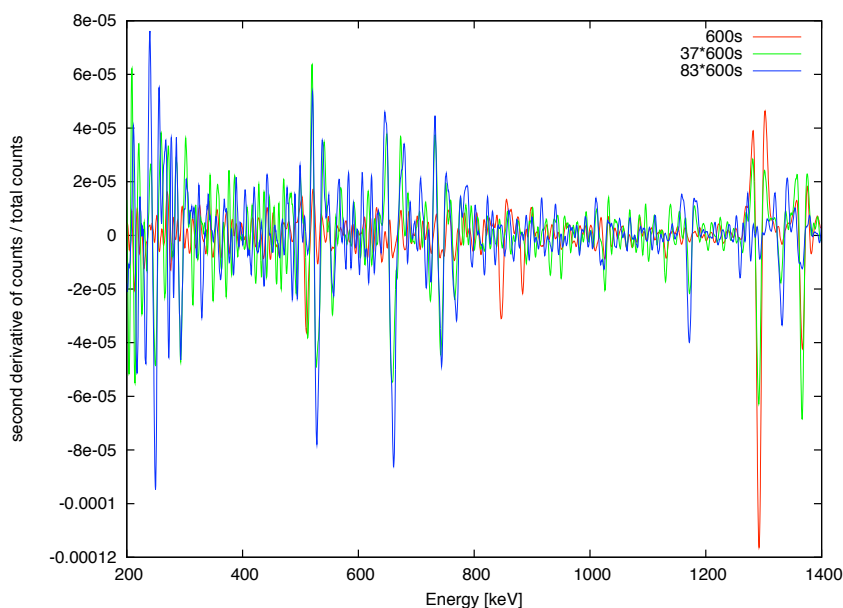


Figure 8.32: Second derivatives of three spectra out of the 84 spectra measured on Feb 01, 2011

second derivatives indicate the actual peak positions, the integral over the negative part of the second derivatives is used for calculation of the total peak area according to equations 6.11 to 6.14. It can clearly be seen that the peaks visible at the different spectra indicate different nuclides. An example analysis of the decay properties of the nuclides present after shutdown and during the measurements for the 84 spectra measured on Feb. 01, 2011 is presented below.

Identifying peak locations

To find the interesting peak regions, a histogram of all peaks according to the algorithm presented above is generated. An example of such a histogram is presented in fig. 8.33 which shows the peak frequencies of all 84 spectra mentioned above. After code execution, seven interesting peak regions $[x_1, x_2]$ are identified:

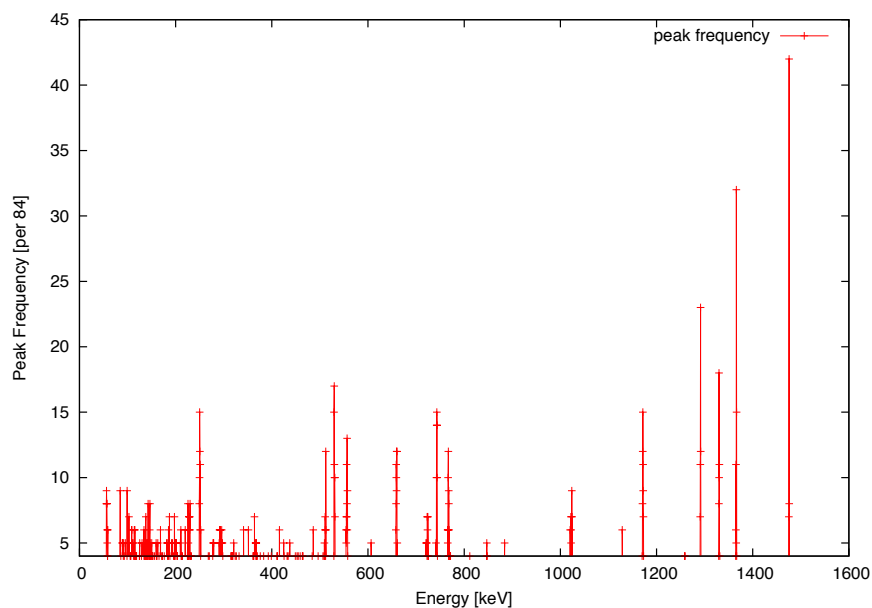


Figure 8.33: Peak frequency in all 84 spectra of Feb 01, 2011

Table 8.10: Identified peaks in the 84 spectra measured on Tue Feb 01, 2011 (excerpt)

peak #	x_1 [keV]	x_2 [keV]	\bar{x} [keV]	Nuclide
8	137.6	149.0	143.3	^{235}U (143.8 keV)
17	180.2	188.6	184.4	^{235}U (185.7 keV)
24	245.5	255.0	250.2	^{135}Xe (249.7 keV)
64	506.8	515.2	511.0	- (annihilation peak at 511 keV)
68	653.7	667.1	660.4	^{137}Cs (661.6 keV)
78	1124.8	1135.7	1130.2	^{135}I (1131 keV))
79	1166.4	1176.7	1171.5	^{60}Co (1173.2 keV)
81	1253.3	1263.6	1258.5	^{135}I (1260 keV))
82	1285.9	1297.0	1291.5	^{41}Ar (1291 keV)
83	1324.8	1335.3	1330.1	^{60}Co (1332.5 keV)
84	1360.4	1371.3	1365.8	^{24}Na (1365 keV))

Analysis of the time dependent peak areas

The amplitudes of the second derivatives (smoothed and non-smoothed) of this 84 example spectra have been investigated using the algorithm presented in section 6.1. For the peaks #24 (^{135}Xe) and #78 (^{135}I) the measurements and their corresponding fits are presented in figures 8.35 and 8.34.

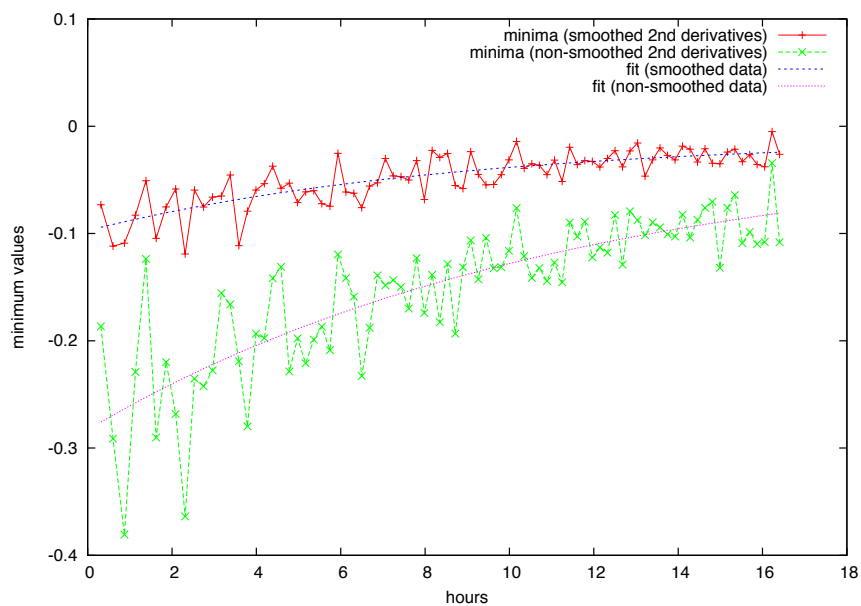


Figure 8.34: Values for the second derivatives of the first ^{135}I peak (1131 keV) over time

The actual peak areas can then be obtained by using the multiplication factor given in eq. 6.18 resulting in the data presented in figures 8.38 (for ^{135}Xe) and 8.36 (for ^{135}I).

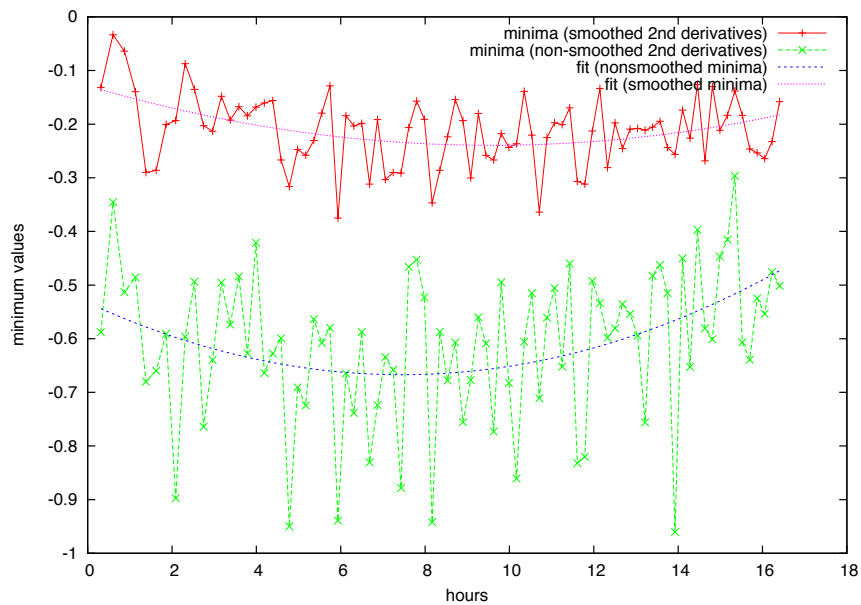


Figure 8.35: Values for the second derivatives of the dominant ^{135}Xe peak (249.7 keV) over time

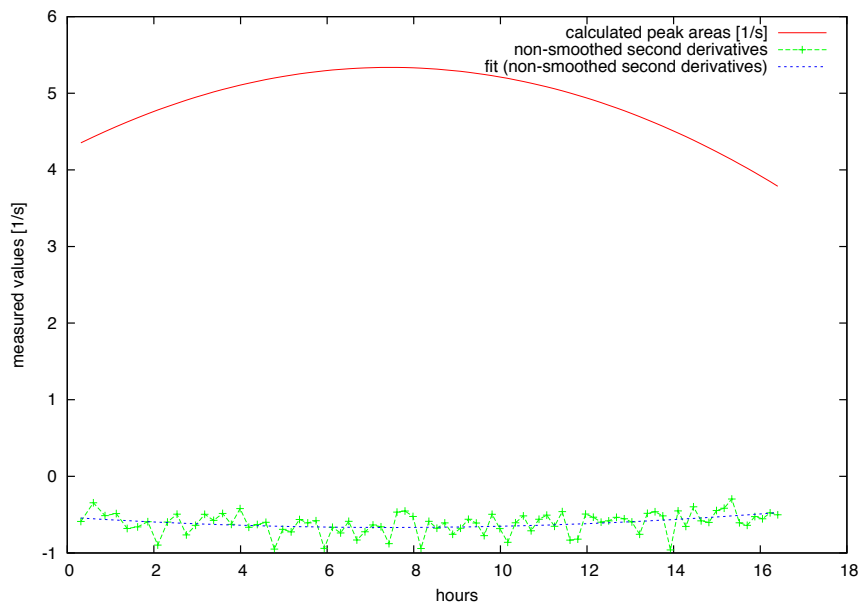


Figure 8.36: Peak areas $[\frac{1}{s}]$ of the dominant ^{135}Xe peak (249.7 keV) over time

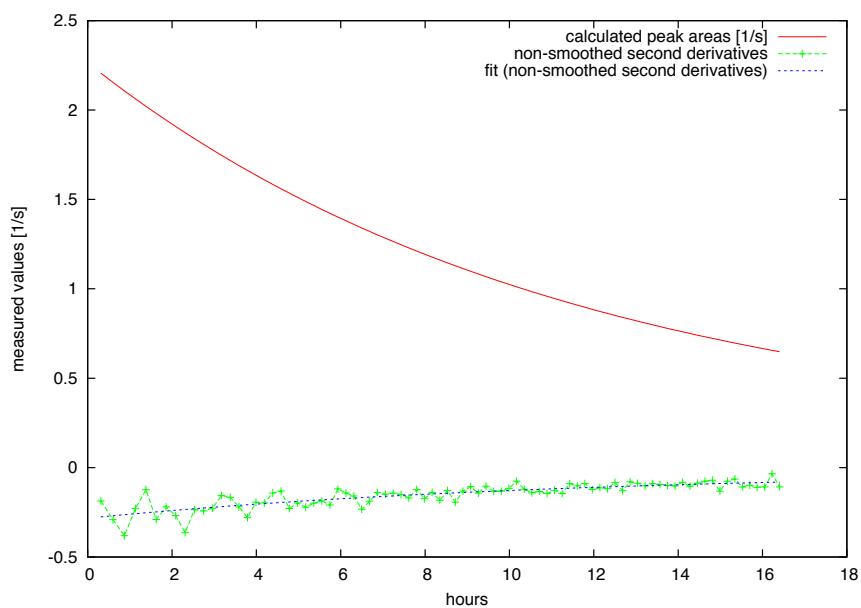


Figure 8.37: Peak areas $[\frac{1}{s}]$ of the first ^{135}I peak (1131 keV) over time

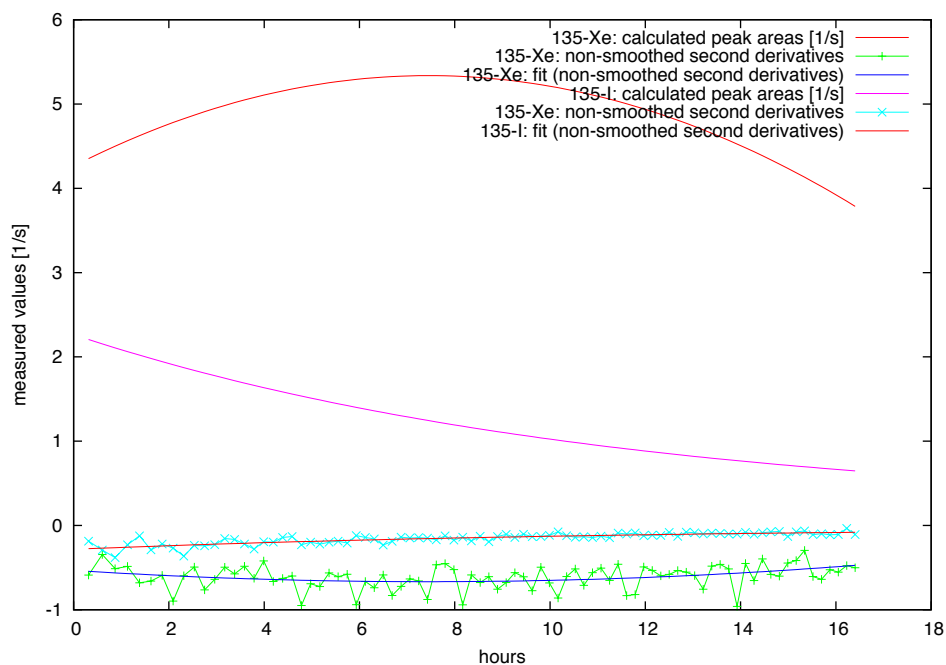


Figure 8.38: Peak areas $[\frac{1}{s}]$ and fits for ^{135}I and ^{135}Xe over time

Analysis of detector shifting with time

By comparing the channel positions of certain peaks in the gamma ray spectra recorded detector shifting with time can be investigated. For example, fig. 8.41 shows a histogram of the channel numbers of the located Xenon peak. In this histogram two peaks are visible, one small and a broader one. The reason must be the use of two different detector setups as the shift is not expected to this big at the one hand and not as clearly separated on the other hand. One Gaussian shape is expected. In fact two different detector settings were used in the experiment.

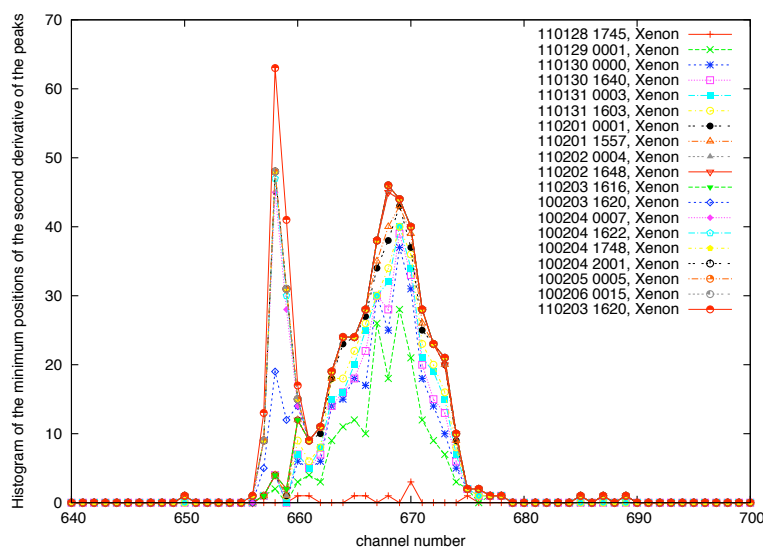


Figure 8.39: Histogram of Xenon peak locations

8.8.4 Discussion

The algorithm is stable and yields reproducible results. Visual comparison between the measured spectrum data and the identified peaks are found to be in good agreement. The time dependent behavior of nuclides present after reactor shutdown can be evaluated automatically with only little effort giving reasonable results: exponential decrease for the Iodine peak and a superposition of production and decay behavior of the Xenon peak (with equilibrium after about 6 hours after reactor shutdown) for example as shown above.

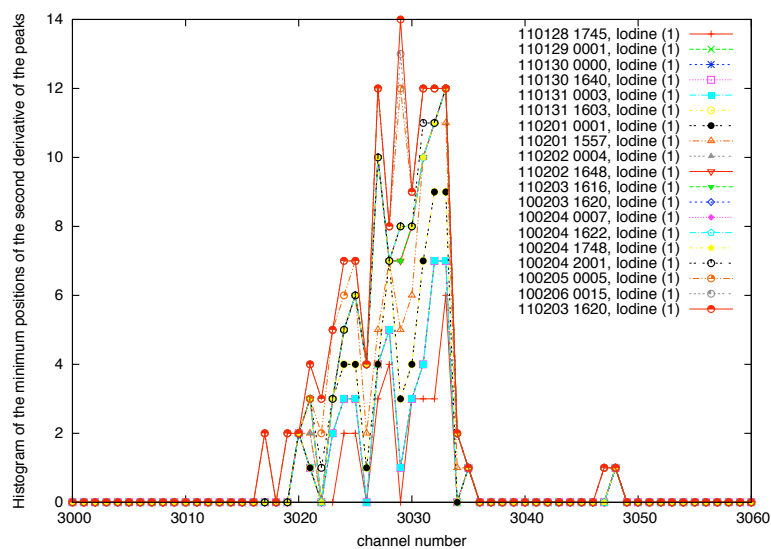


Figure 8.40: Histogram of Iodine (1) peak locations

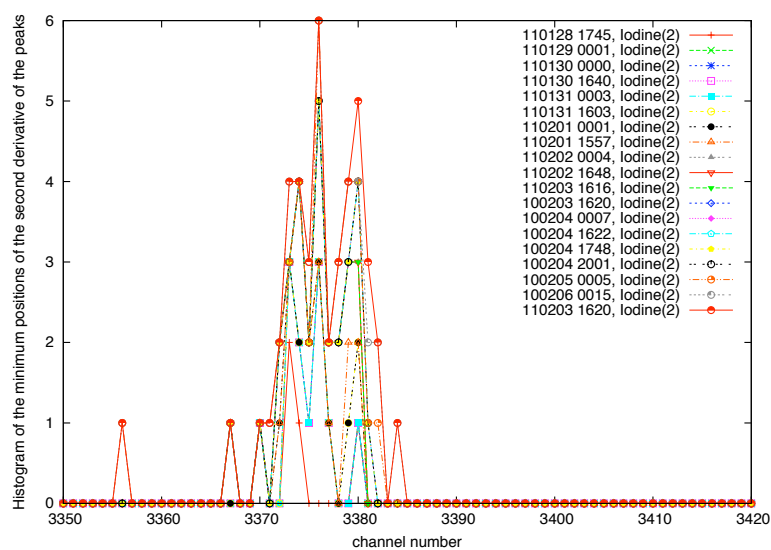


Figure 8.41: Histogram of Iodine (2) peak locations

8.9 Xenon and Iodine measurements

Using the setup described in section 8.7.1, spectra have been measured from Jan 28, 2011 to Feb 4, 2011 starting after reactor shutdown each day. An overview of the recorded spectra can be found in 8.7. Example analyses for the series from Jan. 28th to Jan. 30th, 2011 and Feb. 1st, 2011 have been presented above.

On each measurement day the reactor history has been recorded to be able to reproduce the Iodine and Xenon production and decay history. This data can be found in table 8.11. On the weekend between Jan 28 and Jan 31 the reactor remained in shutdown state. The measurements were continued over the whole weekend.

Table 8.11: Reactor operation between Jan 28, 2011 and Feb 3, 2011

Date	Weekday	Startup	Shutdown	Start of Meas.	End of Meas.
2011-01-26	Wednesday	10:57	15:06	-	-
2011-01-27	Thursday	09:49	16:15	-	-
2011-01-28	Friday	09:26	15:30	16:45	-
2011-01-29	Saturday	-	-	-	-
2011-01-30	Sunday	-	-	-	14:38
2011-01-31	Monday	09:16	15:45	16:03	08:46
2011-02-01	Tuesday	09:00	15:27	15:58	08:45
2011-02-02	Wednesday	09:05	15:45	16:48	08:00
2011-02-03	Thursday	09:04	15:45	16:21	08:00

8.9.1 Analytical Iodine and Xenon history in the relevant time period

To provide analytical data for Iodine and Xenon development over time including reactor operation periods equations 4.13 to 4.18 have been used to calculate $I(t)$ and $Xe(t)$. For $I(t)$, the analytical solution has been used. For calculation of $Xe(t)$ equation 4.18 has been integrated numerically.

8.9.2 Evaluation of the experimental data for Xenon and Iodine

Time dependent integral counts

First of all, the developing of the integral counts with time is of interest. This has been done by opening each spectrum, adding each channel content and printing the result to a file which can be viewed or processed later for each day separately. The graphical representation of the development of the integral counts with time can be used as a simple filter to decide between

useful data (e.g. recorded stable over 12 hours) versus useless data (e.g. a run started at 16:00, cancelled at 17:00 and restarted at 17:10 would not generate enough data for further Xenon peak search processing).

The most stable spectra were recorded on Feb. 1, 2011 and Feb. 3, 2011. Their integrated count rate development with time is shown on fig. 8.42.

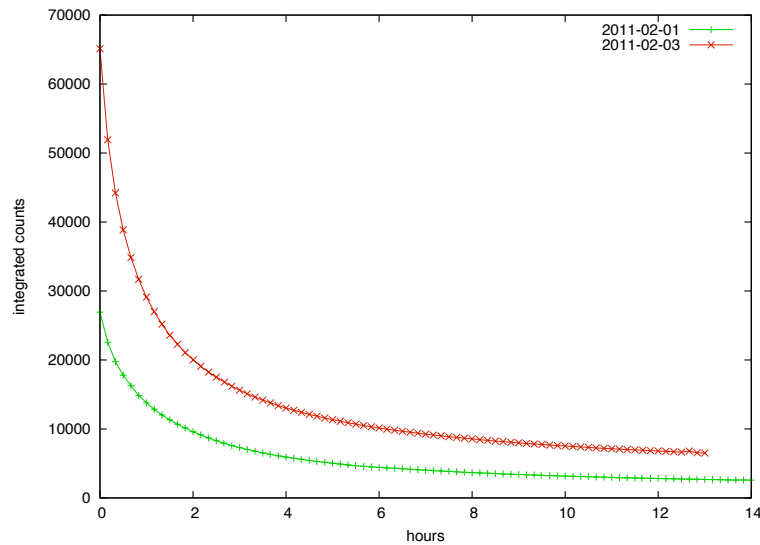


Figure 8.42: Integrated count rate over the whole energy range versus time

Searching for Xenon and Iodine peaks

As described in 8.9.1 the number of Xenon and Iodine nuclei in the period of interest have been calculated. The results are shown in fig. 8.43 together with the reactor operation history during this time.

The algorithm described in chapter 6 has been applied to the 1277 spectra recorded. Not all of them were usable due to either poor counting statistics and/or high dead times. Especially the latter has been a problem due to the high gamma ray background generated in presence of the reactor and the fuel element mounted in the measurement position. As the measurements could in fact be evaluated after finishing each experiment the results could not be foreseen. Two measurement batches were good enough to be evaluated: the measurement over the weekend from Jan 28th to Jan 31st and the overnight measurement starting on Jan 31st. The counting statistics become worse with time caused by the constant measurement time interval as the integral counts of each spectrum decrease proportional to $\exp(-t)$.

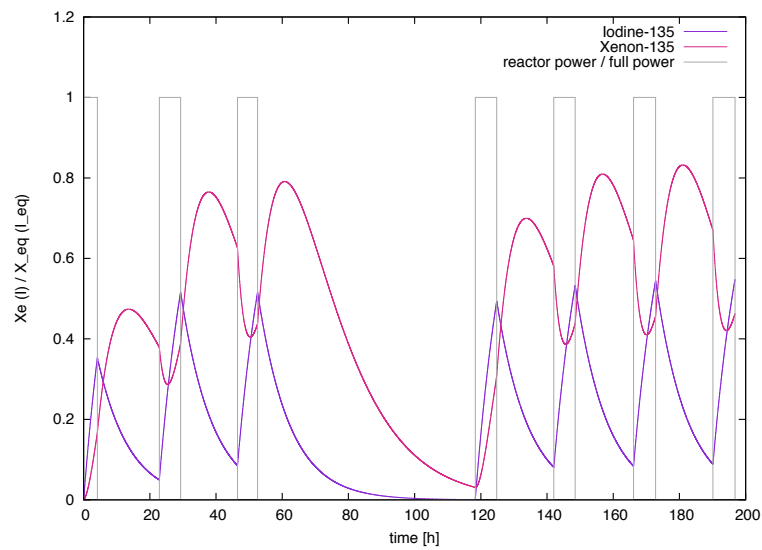


Figure 8.43: Theoretical Iodine and Xenon development with reactor operation history between 2011-01-28 and 2011-02-04

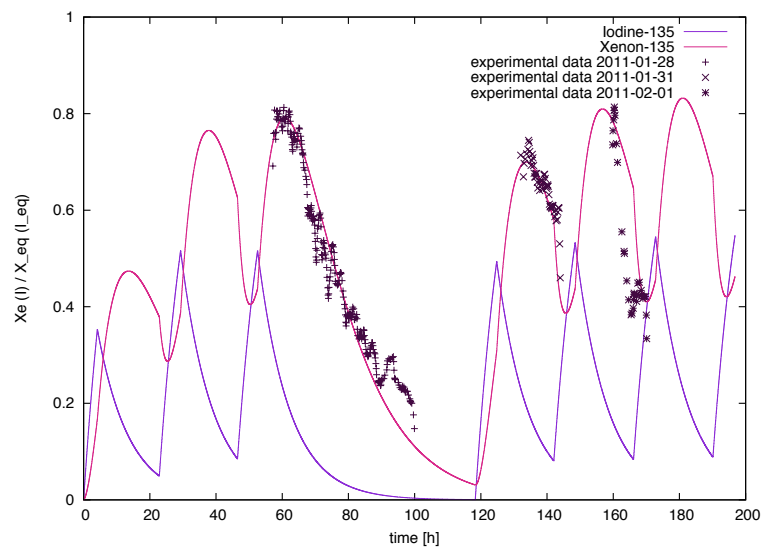


Figure 8.44: Xenon development (numerical results) and experimental data

8.10 Xenon poisoning effects on reactivity

Xenon poisoning can be effectively measured by watching the control rod positions over a certain time period. The more poisoning occurs, the more negative external reactivity has to be applied for the reactor to stay in a stable critical state. This positive external reactivity can be quantified by the recorded differences of the rod positions.

Recording of rod positions after reaching criticality and shortly before reactor shutdown is a regular daily process in the operation of the TRIGA reactor in Vienna. To make the calculations easier the negative reactivity caused by Xenon poisoning has been compensated solely by the shim rod in the period between Jan 28th and Feb 4th, 2011. Table 8.12 lists the relevant days together with both rod positions on each day.

Table 8.12: Recorded startup and shutdown positions of transient, regulating and shim rod

Date	startup or shutdown position	TR	RR	SR
2011-01-31	startup	499	331	298
2011-01-31	shutdown	499	331	334
2011-02-01	startup	499	350	275
2011-02-01	shutdown	499	350	310
2011-02-02	startup	499	350	267
2011-02-02	shutdown	499	350	305
2011-02-03	startup	499	350	263
2011-02-03	shutdown	499	350	311

Table 8.13: Reactivity compensation needed due to Xenon poisoning (experimental data)

Startup	Shutdown	SR from	SR to	dz	Reactivity [c]
2011-01-31 09:16	2011-01-31 15:45	298	334	36	0.3251
2011-02-01 09:04	2011-02-01 15:27	275	310	35	0.3161
2011-02-02 09:05	2011-02-02 15:45	267	305	38	0.3432
2011-02-03 09:08	2011-02-03 15:45	263	311	48	0.4336

Chapter 9

Conclusion

SCIENCE IS ALWAYS WRONG. IT NEVER SOLVES A PROBLEM WITHOUT CREATING TEN MORE. *George Bernard Shaw*

9.1 Numerical reactor kinetics

The modeling of the reactor behavior took much longer than designing and performing the actual experiment itself. The algorithm presented by [16] is a general approach designed to model the behavior of power reactors rather than experimental facilities like the TRIGA reactor in Vienna. The analysis of the impact of each input parameter on the final result and the stability of the result lead to a deep understanding of the involved physics: neutron physics, heat transfer and all the mathematics involved in the solution of systems of partial differential equations. As always in physics, the most important factor is equilibrium; so it is here.

The algorithm showed instabilities for small time differences most probably caused by catastrophic cancellation, truncation and/or accumulating rounding errors. Further investigation would be of interest to enable the simulation of reactor pulsing experiments.

In section 7.6 a correction function is presented. The reason for needing it is probably the temperature dependent thermal feedback coefficient function which is unique for each reactor and its configuration. The strongest argument is the obviously quadratic deviation rather than just a random one. Further studies would be of interest.

Time dependent neutron flux density would be of interest as a function of position in the reactor tank, for example at the center of the tank and two vertically and horizontally offset positions. As I had no access to prompt self powered neutron detectors this experiment could not be implemented. Eventually the use of Cobalt self-powered neutron detectors could help.

9.2 Xenon measurements and spectrometry in general

It has been shown that measuring the Xenon inventory in the reactor (respectively in a fuel rod of interest) after shutdown is possible and in good agreement with experiments. It is, of course, time-consuming and needs a lot of data post-processing. The algorithm developed in this thesis is a powerful tool for spectrum analysis and is worth to be developed further. One of its weaknesses is the fact that it is not at all user-friendly and needs a lot of programming experience to be adapted for other, possibly more general, needs.

Chapter 10

Acknowledgements

DAS LEBEN IST KEIN ZUCKERSCHLECKEN. UND KEIN KINDERGEBURTSTAG. UND AUCH KEIN PONYHOF! *Martin Weiler, 2010*

KRIEG IST DIE HÖLLE.¹ *Christoph Koenig, 2011*

I want to thank Helmuth Böck and Mario Villa for providing me an interesting topic for my thesis and for their instructive lectures and lab courses and Sam Karimzadeh (ATI/IAEA) and Michael Schrenk (IAEA) for helping me out with detectors for the in-core gamma ray spectrometry measurements.

Thanks to Andreas Kastner for support with numerical pitfalls, Martin Weiler and Oskar Schmidt for continuous entertainment (especially during field training), Norbert Fürstenhofer (Austrian NBC Defence School) for his omnipresent visions, Christoph König for company on the Great Wall, Jörg Riede for Josephine and Mike Norman Dressler for being a soulmate during the last sixteen years.

¹During lunch in business class of flight OS58 on our way to Tokyo after the Fukushima accident, March 2011

List of Tables

4.1	Delayed neutron parameters for the group ^{235}U [12]	12
4.2	Relevant parameters for Iodine and Xenon production and decay [16]	16
5.1	Input parameter list	25
5.2	List of temporary parameters	25
5.3	Output parameter list	26
6.1	Standard deviation data points	34
7.1	Color coding for the fuel elements	40
7.2	Deviatons from experimental results as shown in fig. 7.9	50
7.3	Effects of positive external reactivities at $T_F = 30^\circ\text{C}$	54
7.4	Effects of negative external reactivities at $T_F = 30^\circ\text{C}$	55
7.5	Effects of positive external reactivities at $T_F = 40^\circ\text{C}$	57
7.6	Effects of negative external reactivities at $T_F = 40^\circ\text{C}$	59
7.7	Effects of positive external reactivities at $T_F = 50^\circ\text{C}$	61
7.8	Effects of negative external reactivities at $T_F = 50^\circ\text{C}$	63
7.9	Effects of positive external reactivities at $T_F = 60^\circ\text{C}$	65
7.10	Effects of negative external reactivities at $T_F = 60^\circ\text{C}$	67
7.11	Effects of positive external reactivities at $T_F = 70^\circ\text{C}$	69
7.12	Effects of negative external reactivities at $T_F = 70^\circ\text{C}$	71
7.13	Effects of positive external reactivities at $T_F = 80^\circ\text{C}$	73
7.14	Effects of negative external reactivities at $T_F = 80^\circ\text{C}$	75
7.15	Effects of positive external reactivities at $T_F = 90^\circ\text{C}$	77

7.16	Effects of negative external reactivities at $T_F = 90^\circ\text{C}$	79
7.17	Effects of positive external reactivities at $T_F = 100^\circ\text{C}$	81
7.18	Effects of negative external reactivities at $T_F = 100^\circ\text{C}$	83
7.19	Effects of positive external reactivities at $T_F = 110^\circ\text{C}$	85
7.20	Effects of negative external reactivities at $T_F = 110^\circ\text{C}$	87
7.21	Effects of positive external reactivities at $T_F = 120^\circ\text{C}$	89
7.22	Effects of negative external reactivities at $T_F = 120^\circ\text{C}$	91
7.23	Effects of positive external reactivities at $T_F = 130^\circ\text{C}$	93
7.24	Effects of negative external reactivities at $T_F = 130^\circ\text{C}$	95
7.25	Effects of positive external reactivities at $T_F = 140^\circ\text{C}$	97
7.26	Effects of negative external reactivities at $T_F = 140^\circ\text{C}$	99
7.27	Effects of positive external reactivities at $T_F = 150^\circ\text{C}$	101
7.28	Effects of negative external reactivities at $T_F = 150^\circ\text{C}$	103
8.1	Experimental data	111
8.2	Temperature measurements (rod E13) for various reactor power levels	114
8.3	Comparison of experimental and MCNP results for temperature changes in rod E13 during the experiment	115
8.4	Experimentally determined values for power and temperature. The reactivity has been calculated from an interpolation of the values gained by a preceding experiment. The power and temperature values were taken before the reactivity has been inserted.	120
8.5	Power calibration data. A/V is the gain setting on the SR Amperemeter, the LV scale factor means the factor given by the LabView application, the resulting factor is given by $10 \times \text{LabView factor} / \text{SR factor}$	120
8.6	Dose rate measurements in the TRIGA reactor after shutdown. The position (z) is relative to the lower end of the beamline.	130
8.7	Overview about gamma spectrometry measurements	131
8.8	Datasets used for example analysis	134
8.9	Identified peaks in the 243 spectra measured between Jan. 28th - Jan. 30th, 2011 (excerpt)	136
8.10	Identified peaks in the 84 spectra measured on Tue Feb 01, 2011 (excerpt)	140

8.11 Reactor operation between Jan 28, 2011 and Feb 3, 2011	146
8.12 Recorded startup and shutdown positions of transient, regulating and shim rod .	149
8.13 Reactivity compensation needed due to Xenon poisoning (experimental data) . .	149

List of Figures

3.1	Top view of the TRIGA Mark II research reactor [18]	6
3.2	Side view of the TRIGA Mark II research reactor [18]	6
3.3	Current core configuration with shim rod (SR), transient rod (TR), control rod (CR) and the central irradiation facility (CIR).	7
4.1	Fission product decay chain of ^{235}U to ^{135}Xe	14
4.2	Cross sections for fission of ^{235}U and neutron capture for ^{135}Xe and ^{135}I	14
5.1	Comparison of analytical and numerical solution of the EH algorithm with $a = 5 * 10^{-5} s^{-1}$, $\tau = 20s$, $\lambda = 0.15s^{-1}$, $\beta_{eff} = 0.0065$, $\Lambda = 0$. The bend at $t = 20s$ is clearly visible.	20
6.1	The Gaussian function and its first and second derivatives. The second derivative is expected to be found in the derivated spectrum data if a peak is present.	28
6.2	Close-up: two peak candidates at $x \approx 615$ and $x \approx 672$, sixth order binomial smoothing filter	29
6.3	Histogram of the distribution of $D(x)$ around zero.	30
6.4	$N(x)$ and $N''(x)$ for unsmoothed versus smoothed input data	33
6.5	Close-up: comparison of the second derivatives of previously smoothed vs. unsmoothed input data, fourth order binomial smoothing filter	33
6.6	Original spectrum data and smoothed spectrum used for the standard deviation fits. After calibration the leftmost peak is at 511 keV (annihilation single escape), 1293.6 keV (^{41}Ar) and 1368.63 keV (^{24}Na)	34
6.7	Peak fits to obtain the standard deviation versus channel number	35
7.1	The MCNP model for the TRIGA Mark II reactor Vienna shown as xz plane view	38
7.2	The MCNP model for the TRIGA Mark II reactor Vienna shown as xy plane view	38

7.3	The MCNP model for the TRIGA Mark II reactor Vienna shown as xy plane view (zoomed to core)	39
7.4	Current (standard) core layout of the TRIGA reactor Vienna. Each fuel element is numbered according to its position in the core, reflected in the upper numbers; the lower number indicates both fuel type (see chapter 3) and a element-specific numbering, reflected in the lower numbers.	41
7.5	Core layout of the TRIGA reactor Vienna during the lab course in January 2011	42
7.6	Uncertainties in the simulation results	46
7.7	Computing time needed for different numbers of particles per cycle	47
7.8	Computing time needed for different numbers of particles per cycle versus the resulting uncertainties of the numerical results	48
7.9	Deviation from experimental results	50
7.10	The influence of a multiplication factor applied to α_{TF} once per calculation. . . .	51
7.11	Initial conditions for the heat transfer model	52
7.12	Times to reach a steady state versus initial fuel temperature as described above.	52
7.13	Applied positive reactivities and resulting power deviations	54
7.14	Applied positive reactivities and resulting power deviations	55
7.15	Applied negative reactivities and resulting power deviations	56
7.16	Applied negative reactivities and resulting power deviations	56
7.17	Applied positive reactivities and resulting power deviations	58
7.18	Applied positive reactivities and resulting power deviations	58
7.19	Applied negative reactivities and resulting power deviations	60
7.20	Applied negative reactivities and resulting power deviations	60
7.21	Applied positive reactivities and resulting power deviations	62
7.22	Applied positive reactivities and resulting power deviations	62
7.23	Applied negative reactivities and resulting power deviations	64
7.24	Applied negative reactivities and resulting power deviations	64
7.25	Applied positive reactivities and resulting power deviations	66
7.26	Applied positive reactivities and resulting power deviations	66
7.27	Applied negative reactivities and resulting power deviations	68
7.28	Applied negative reactivities and resulting power deviations	68

7.29 Applied positive reactivities and resulting power deviations	70
7.30 Applied positive reactivities and resulting power deviations	70
7.31 Applied negative reactivities and resulting power deviations	72
7.32 Applied negative reactivities and resulting power deviations	72
7.33 Applied positive reactivities and resulting power deviations	74
7.34 Applied positive reactivities and resulting power deviations	74
7.35 Applied negative reactivities and resulting power deviations	76
7.36 Applied negative reactivities and resulting power deviations	76
7.37 Applied positive reactivities and resulting power deviations	78
7.38 Applied positive reactivities and resulting power deviations	78
7.39 Applied negative reactivities and resulting power deviations	80
7.40 Applied negative reactivities and resulting power deviations	80
7.41 Applied positive reactivities and resulting power deviations	82
7.42 Applied positive reactivities and resulting power deviations	82
7.43 Applied negative reactivities and resulting power deviations	84
7.44 Applied negative reactivities and resulting power deviations	84
7.45 Applied positive reactivities and resulting power deviations	86
7.46 Applied positive reactivities and resulting power deviations	86
7.47 Applied negative reactivities and resulting power deviations	88
7.48 Applied negative reactivities and resulting power deviations	88
7.49 Applied positive reactivities and resulting power deviations	90
7.50 Applied positive reactivities and resulting power deviations	90
7.51 Applied negative reactivities and resulting power deviations	92
7.52 Applied negative reactivities and resulting power deviations	92
7.53 Applied positive reactivities and resulting power deviations	94
7.54 Applied positive reactivities and resulting power deviations	94
7.55 Applied negative reactivities and resulting power deviations	96
7.56 Applied negative reactivities and resulting power deviations	96
7.57 Applied positive reactivities and resulting power deviations	98
7.58 Applied positive reactivities and resulting power deviations	98

7.59	Applied negative reactivities and resulting power deviations	100
7.60	Applied negative reactivities and resulting power deviations	100
7.61	Applied positive reactivities and resulting power deviations	102
7.62	Applied positive reactivities and resulting power deviations	102
7.63	Applied negative reactivities and resulting power deviations	104
7.64	Applied negative reactivities and resulting power deviations	104
7.65	Energy deposition in MeV/g per initial fission neutron, $z = 0$	106
7.66	Energy deposition in MeV/g per initial fission neutron, $z = 15$	106
7.67	Energy deposition in MeV/g per initial fission neutron, close-up of shim rod . . .	107
7.68	Buildup and decay of ^{135}Xe and ^{135}I for a neutron flux of 10^{13}ns^{-1} . Values are given relative to the equilibrium values $^{135}\text{Xe}_{eq}$ and $^{135}\text{I}_{eq}$ (see text).	108
7.69	Xenon buildup: ration of $^{135}\text{Xe} / ^{135}\text{Xe}_{eq}$ versus time for different neutron fluxes.	108
8.1	Cumulative reactivities versus shim rod position.	112
8.2	MCNP model for shim rod at position 150 (shown in petrol blue)	112
8.3	Results of MCNP calculations of the shim rod reactivity per unit length versus experimental data	113
8.4	Fuel temperatures versus reactor power.	114
8.5	Comparison of experimental and MCNP data for temperature changes in rod E13 for various power levels	116
8.6	Energy deposition in rod E13, 5kW to 250kW	117
8.7	Amperemeter calibration	118
8.8	The complete data record for the reactivity feedback measurements as an overview. Note the clearly visible temperature feedback effects showing at about an hour after measurements started. The sharp peaks are artefacts caused by changes in the Amperemeter gain settings.	119
8.9	Final power calibration using the data from table 8.5. Note that the data shown in this table are values before correction with the calibration from the Amperemeter calibration data fit.	121
8.10	Deviation from steady state: Experimental versus numerical results for the first step	122
8.11	Deviation from steady state: Experimental versus numerical results for the second step	123

8.12 Deviation from steady state: Experimental versus numerical results for the third step	123
8.13 Deviation from steady state: Experimental versus numerical results for the fourth step	124
8.14 Deviation from steady state: Experimental versus numerical results for the fifth step	124
8.15 Deviation from steady state: Experimental versus numerical results for the sixth step	125
8.16 Deviation from steady state: Experimental versus numerical results for the seventh step	125
8.17 Fuel rod scanning device	127
8.18 Fuel rod scanning device placed onto the thermal column (final position for measurements)	128
8.19 HPGe detector over the constructed beamline	129
8.20 Experimental count rate measurements and the corresponding fit	130
8.21 Gamma ray spectra (selection) Wednesday pre midnight; x-axis: energy [keV], y-axis: total counts	132
8.22 Gamma ray spectra (selection) Wednesday post midnight; x-axis: energy [keV], y-axis: total counts	132
8.23 Gamma ray spectra (selection) Wednesday pre midnight; x-axis: energy [keV], y-axis: total counts	133
8.24 Gamma ray spectra (selection) Wednesday post midnight; x-axis: energy [keV], y-axis: total counts	133
8.25 Peak frequency in all 243 spectra of Jan. 28th - Jan. 30th, 2011 ($c = 0.08c_{gm}$) . .	135
8.26 Peak frequency in all 243 spectra of Jan. 28th - Jan. 30th, 2011 ($c = 0.02c_{gm}$) . .	135
8.27 Peak frequency in all 243 spectra of Jan. 28th - Jan. 30th, 2011 (combined) . . .	136
8.28 Values for the second derivatives of the first ^{135}I peak (1131 keV) over time . . .	137
8.29 Values for the second derivatives of the dominant ^{135}Xe peak (249.7 keV) over time	137
8.30 Peak areas $[\frac{1}{s}]$ of the dominant ^{135}Xe peak (249.7 keV) over time	138
8.31 Peak areas $[\frac{1}{s}]$ of the first ^{135}I peak (1131 keV) over time	138
8.32 Second derivatives of three spectra out of the 84 spectra measured on Feb 01, 2011	139
8.33 Peak frequency in all 84 spectra of Feb 01, 2011	140

8.34	Values for the second derivatives of the first ^{135}I peak (1131 keV) over time . . .	141
8.35	Values for the second derivatives of the dominant ^{135}Xe peak (249.7 keV) over time	142
8.36	Peak areas $[\frac{1}{s}]$ of the dominant ^{135}Xe peak (249.7 keV) over time	142
8.37	Peak areas $[\frac{1}{s}]$ of the first ^{135}I peak (1131 keV) over time	143
8.38	Peak areas $[\frac{1}{s}]$ and fits for ^{135}I and ^{135}Xe over time	143
8.39	Histogram of Xenon peak locations	144
8.40	Histogram of Iodine (1) peak locations	145
8.41	Histogram of Iodine (2) peak locations	145
8.42	Integrated count rate over the whole energy range versus time	147
8.43	Theoretical Iodine and Xenon development with reactor operation history between 2011-01-28 and 2011-02-04	148
8.44	Xenon development (numerical results) and experimental data	148

Bibliography

- [1] Judith F. Briesmeister (Editor): *MCNP – A General Monte Carlo N-Particle Transport Code*, Los Alamos National Laboratory report LA-12625-M, 1993
- [2] M. Villa, T. Stummer, R. Khan, H. Boeck: *Possibility of a Partial HEU-LEU TRIGA Fuel Shipment*, International conf. on Research Reactor Fuel Management RRFM 2007, session VII, 12-14 March 2007, Lyon, France.
- [3] R. Jera j, B. Glumac, M. Maucec: *MCNP Simulation of the TRIGA Mark II Benchmark Experiment*, Nuclear Society of Slovenia 1996
- [4] Computational analysis of Bangladesh 3 MW TRIGA research reactor using MCNP4C, JENDL-3.3 and ENDF/B-VI data libraries
- [5] Dodd, B.; Klein, A.C.; Lewis, B.R.; Merritt, P.A: *Results of the MCNP analysis of 20/20 LEU fuel for the Oregon State University TRIGA reactor*, 14. U.S. TRIGA users conference San Diego, CA (United States) 5-8 Apr 1994
- [6] Nacir, B.; Htet, A.; Erradi, L.; Chakir, E. : *Results of MCNP analysis for Moroccan TRIGA Mark-II Reactor*, 1. world TRIGA users conference Pavia (Italy) 16-20 Jun 2002
- [7] Abdel Munem, E.; Shukri, A.; Tajuddin, A.A.: *Neutron flux measurement in the thermal column of the Malaysian TRIGA mark II reactor with MCNP verification*, 12. international congress on neutron capture therapy Takamatsu, Kagawa (Japan) 9-13 Oct 2006
- [8] Snoj, L.; Ravnik, M.: *Calculation of power density with MCNP in TRIGA reactor*, International Conference Nuclear Energy for New Europe 2006 Portoroz (Slovenia) 18-21 Sep 2006
- [9] Yazid, P. I.: *Analysis Of Criticality Experiments Of Bandung Triga 2000 Reactor By Using MCNP-4B Code Analisis Percobaan Kekritisasi Teras Reaktor Triga 2000 Bandung Dengan Program MCNP-4B*, Conference on the Role of Nuclear Science and Technology on Empowering National Potential Bandung (Indonesia) 11-12 Jul 2000
- [10] Matsumoto, T.; Hayakawa, N.: *Benchmark analysis of TRIGA mark II reactivity experiment using a continuous energy Monte Carlo code MCNP*, Journal of Nuclear Science and Technology (Tokyo) , (Dec 2000) v. 37(12) p. 1082-1087

- [11] Matsumoto, T.; Hayakawa, N.: Benchmark analysis of reactivity experiment in the TRIGA Mark 2 reactor using a continuous energy Monte Carlo code MCNP, Musashi Kogyo Daigaku Genshiryoku Kenkyusho Kenkyusho-Ho, No. 26 (Jun 2000) p. 29-40
- [12] Stacey, Weston M.: *Nuclear Reactor Physics, Wiley-VCH, second edition 2007*
- [13] *Evaluated Nuclear Data File (ENDF) Database Version of May 31, 2010*
- [14] Boeck, Helmuth; Villa, Mario: *TRIGA REACTOR CHARACTERISTICS* AIAU 24309, June 2004
- [15] Rauch, H.: *Vorlesungsskriptum Reaktorphysik I*, AIAU 98402, 1998
- [16] Emmendoerfer, D.; Hoecker, K.: *Theorie der Kernreaktoren Part I & II*, B.I. Wissenschaftsverlag Mannheim 1982
- [17] Meschede, D.: *Gerthsen Physik*, Springer 2006
- [18] Boeck, H.; Villa, M.: *The TRIGA MArk II reactor at Vienna University of Technology*, ATI report, 2005
- [19] Mariscotti, M. A.: *A method for automatic identification of peaks in the presence of background and its applications to spectrum analysis*, Nuc. Inst. Meth. 50 (1967), 309-320
- [20] Marchand, P. and Marmet, L.: *Binomial smoothing filter: A way to avoid some pitfalls of least-squares polynomial smoothing*, Rev. Sci. Instrum. 54 (8), 1983.
- [21] Levenberg, K.: *A Method for the Solution of Certain Non-Linear Problems in Least Squares*, The Quarterly of Applied Mathematics 2: 164-168. (1944)
- [22] IAEA Nuclear Data Bank, www-nds.iaea.org
- [23] Wolfram Research, Inc., Mathematica, Version 6.0, Champaign, IL (2008)
- [24] General Atomics, *100kW TRIGA Pulsing Reactor Mechanical Operation and Maintenance Manual*, General Atomics, USA (1962)
- [25] Khan, R.: *Neutronics Analysis of the TRIGA Mark II Reactor Core and its Experimental Facilities*, Dissertation, TU Wien 2011

Mag. rer. nat. Julia Riede
Butjadinger Str. 57
26969 Butjadingen-Tossens
Deutschland

LEBENS LAUF

Persönliche Daten

Geburtsdatum: 22.10.1976
Geburtsort: Steyr, Oberösterreich
Familienstand: verheiratet, zwei Kinder

- Seit 12/2012 **Entwicklungsingenieurin bei AREVA, Bremerhaven**
Forschung & Entwicklung im Bereich Messtechnik (Fernfeld-
Windmessungen mit LIDAR)
- 04/2011 – 12/2012 **Prozessingenieurin bei AREVA, Erlangen**
Technische Teilprojektleiterin nukleare Instrumentierung im
Kernkraftwerk Olkiluoto 3, Finnland
- seit 10/2009 **Doktoratsstudium am Atominstitut der Technischen Universität
Wien**
Betreuer: Ao. Prof. Dr. Helmuth Böck
Thema: "*Numerische Simulation nichtstationärer Zustände des TRIGA-
Forschungsreaktors Wien*"
- 12/2006 - 04/2011 **Kernphysikerin im Bundesministerium für Landesverteidigung,
Korneuburg, Österreich**
- 04/2006 - 12/2006 Wehrdienst im österreichischen Bundesheer (ABC-Abwehr)
- 11/2005 - 04/2006 Trainingsvorbereitung für den Wehrdienst
- 10/2002 - 10/2005 **Diplomstudium Physik an der Universität Wien**
Diplomarbeitsthema: "*Simulation des Ansprechverhaltens von NaI(Tl)
Bohrlochdetektoren zur genauen Aktivitätsmessung von Gammastrahlung-
emittierenden Radionukliden*"
Abschluss nach nur sechs Semestern (Mindestzeit: zehn Semester) mit
Auszeichnung (Abschlussnote: 1.5)
- 2002 Mündliche Matura in Chemie und Physik
Studienberechtigungsprüfung an der Universität Wien
- 08/2001 - 10/2002 Programmierung und Systemadministration bei Young&Rubicam, 1010
Wien
- 08/2000 - 08/2001 Programmierung und Systemadministration bei Kabel New Media, 1150
Wien
- 08/1999 - 08/2000 Webgrafik und –programmierung bei Mang D’Arcy, 1030 Wien
- 08/1998 - 08/1999 Mutterschaftsurlaub
- 04/1997 - 08/1998 Webgrafik und –programmierung bei PPMedia, 1020 Wien
- 1995 - 1997 Fahrradkurier in Wien, Hamburg und Berlin
- 1992 - 1995 HTL Steyr, Fachrichtung Gold- und Silberschmiede
- 1991 - 1992 Hauptschule in Steyr-Promenade
- 1987 - 1991 Bundesgymnasium Steyr-Werndlpark
- 1983 - 1987 Volksschule in Steyr-Tabor